Amperometric Gas Sensing Using Room Temperature Ionic Liquids

A thesis submitted for the degree of Doctor of Philosophy in
Physical and Theoretical Chemistry

Peilin Li

Wolfson College

Trinity Term 2015

Abstract

The work presented in this thesis aims at overcoming the limitations of current amperometric gas sensors. The applicability of room temperature ionic liquids to be employed as potential electrolyte in gas sensors has been examined. This thesis demonstrates that RTILs have great potential to replace conventional electrolytes due to their wide electrochemical windows, negligible vapour pressure, inherent conductivity and sensitivity. A model to simulate the current response at porous electrodes has also been proposed to provide a theoretical support for the future application of porous electrodes in gas sensors. The results of these researches are summarised as follows:

Chapter 1 introduces the fundamentals of electrochemistry which are employed throughout this thesis. Chapter 2 presents a comprehensive review of the history and recent development of amperometric gas sensors with their specific applications and limitations presented. Room temperature ionic liquids, microelectrodes and porous electrodes are also introduced in this chapter to initially discuss their potential for gas sensors.

Chapter 4 studies the interaction between carbon dioxide and an imidazolium cation based RTIL. The solubility and diffusion coefficient are determined by the analysis of chronoamperometry using the Shoup and Szabo equation. A mechanism of the interaction between CO_2 and the RTIL is proposed and validated by theoretical modelling.

Chapter 5 focuses on O_2 uptake in a phosphonium cation based RTIL. A mechanism of O_2 reduction in this RTIL is proposed, reflecting a two electron reduction pathway. Proof-of-concept for this RTIL to be developed into a CO_2/O_2 dual sensor is confirmed with by experiments with CO_2/O_2 gas mixtures.

Oxygen uptake in a series of alkylammonium cation based RTILs has been carried out as described in Chapter 6. The diffusivity of O_2 in RTILs does not follow the Stoke-Einstein equation but broadly decreases as the viscosity increases.

Chapter 7 proposes a theoretical model for the electrochemical behaviour at porous electrodes. Studies with two types of porous electrodes are employed and validate the applicability for this model to simulate the current response at porous electrodes.

Acknowledgements

First and foremost, I would like to express my deepest gratitude to my supervisor Professor Richard G. Compton for his guidance, encouragement and patience during my D. Phil.. I would never have been able to finish my work and thesis without his support and understanding.

I would also like to thank all the group members, past and present, and in particular Dr. Linhongjia Xiong, who provided all kinds of help during my first and second year, even after she left Oxford, Dr. Edward Barnes and Dr. Martin Henstridge, who kindly provided theoretical knowledge and simulation programmes throughout this three years, Mr. Alex Neale, who came to Oxford twice all the way from Belfast for collaborations and extremely useful materials for my thesis. Special thanks to Mr. Xiaofei Zhou, Miss Patricia Lee, Miss Rita Nissim, Miss Her Shuang Toh, Miss Qianqi Lin, who joined the group at the same time as me, without your accompanying for three years, life would be very difficult. Also to Dr. Chris Batchelor-McAuley, Dr. Kristina Tschulik, Dr. Ying Wang, Dr. Wei Cheng, Dr. Lior Sepunaru, Dr. Enno Kätelhön, Mr. Shaltiel Eloul, Miss Eden Tanner for always being on hand to help. I thank everyone in the Compton group for encouragement and understanding.

I would like to acknowledge Professor Christopher Hardacre and Dr. Peter Goodrich for providing a huge amount of clean and neat RTILs for my project and collaboration.

I would also like to thank all my friends in Wolfson College and Oxford, life has never been lonely because of the Formals, BBQs, travelling and punting we had together.

I sincerely thank China Scholarship Council for the generous financial assistance. It is my great honour to be selected for the scholarship.

Finally, I would like to thank my parents who forever encourage and support me during my good times and hard times.

Glossary

Symbol	Definition	Unit
α	cathodic electron transfer coefficient	
β	anodic electron transfer coefficient	
η	dynamic viscosity	mPa·s
κ	specific conductivity	$S \cdot m^{-1}$
τ	dimensionless time	
ϕ	electrostatic potential	V
v	scan rate	$V \cdot s^{-1}$
γ	activity coefficient	
Λ	Matsuda and Ayabe parameter	
A	electrode area	cm^2
c/[]	concentration	$mol \cdot dm^{-3}$
$[]_0$	solution concentration at electrode surface	$mol \cdot dm^{-3}$
c^*	concentration of bulk solution	$mol \cdot dm^{-3}$
C_d	double layer capacitance	$F \cdot m^2$
D	diffusion coefficient	$cm^2 \cdot s^{-1}$
e^-	electron	
E	electrode potential	V
E^o	standard electrode potential	V
E_f^0	formal potential	V
F	Faraday constant	$96485\ C \cdot mol^{-1}$
i	current	A

i_{ss}	steady state limiting current	A
J	flux	$\mathrm{mol{\cdot}cm^{-2}{\cdot}s^{-1}}$
k^0	heterogeneous rate constant	$\mathrm{cm{\cdot}s^{-1}}$
k_f	forward rate constant	$\mathrm{cm{\cdot}s^{-1}}$
k_b	backward rate constant	$\mathrm{cm{\cdot}s^{-1}}$
n	number of electrons transferred	
p	pressure	kPa
R	Universal Gas Constant	$\mathrm{j{\cdot}K^{-1}{\cdot}mol^{-1}}$
r	electrode radius	M
t	time	s
T	Absolute temperature	K

Contents

Chapter 1

Fundamentals of Electrochemistry

This thesis is concerned with the development of electrochemical sensing and measurement techniques using room temperature ionic liquids (RTILs). The first chapter explains some of the key theoretical concepts of electrochemistry underpinning the work presented in this thesis. More detailed discussion can be found later in each chapter, where needed.

1.1 The Electrochemical Cell

An electrochemical cell is used to bring about electrochemical reactions. Consider a simple one-electron oxidation reaction in solution. At least two electrodes are required in order to apply a potential difference across a solution to induce the required electron transfer. The first electrode represents the interface of interest and under study. This is the 'working electrode' (WE), and the second electrode acts as the other half of the cell. The second electrode needs to have a known potential to calibrate the relative potential on the working electrode and to balance the charge flows from/to the working electrode. However, it is very difficult for an electrode to pass an appreciable current as well as maintain a constant potential.[1,2] Therefore, a 'reference electrode' (RE) and a 'counter electrode' (CE) are usually introduced in place of the second electrode to realise these functions. The reference electrode is designed to provide a constant value of potential assisted by passing negligible current through the electrode. The counter electrode balances the current observed at the working electrode by passing all the current through it. Thus the potential of the working electrode can be measured against the reference electrode. This is the so called ‘‘three-electrode system’’, which is used throughout the all the experiments reported in this thesis.

1.1.1 Chemical Equilibrium and Electrode Potential

Consider a simple electrochemical equilibrium between an electrode and electrolyte:

$$\mathrm{A} + n\mathrm{e}^{-} \rightleftharpoons \mathrm{B} \tag{1.1}$$

where A is reduced in the electrolyte, gaining n electrons to form species, B. Once the equilibrium established, the number of electrons gained by A is exactly equals the electrons lost by B. The Nernst equation is used to determine the potential of the equilibrium:

$$E = E^{o} + \frac{RT}{nF} ln \frac{a_A}{a_B} \tag{1.2}$$

where E is the potential at equilibrium, E^{o} is the standard electrode potential, R is the Universal Gas Constant, T is the absolute temperature, n is the number of electrons transferred, F is the Faraday constant and a_A/a_B are the activities of the electroactive species A/B involved in reaction (1.1). The activities of the electroactive are related to their concentrations, c_A and c_B, by unitless activity coefficients, γ_A or γ_B:

$$a_A = \gamma_A \cdot c_A \tag{1.3a}$$

$$a_B = \gamma_B \cdot c_B \tag{1.3b}$$

The standard electrode potential, E^o, is measured relative to a standard hydrogen electrode (1 atm H_2, 298 K and activity of H^+ equals 1). However, often due to the lack of knowledge in respect of the activity coefficients, the concept of the formal potential, E_f^0, is introduced to better express the electrode potential:

$$E = E_f^0 + \frac{RT}{nF} ln \frac{c_A}{c_B} \qquad (1.4)$$

Equation (1.4) is now related to the concentration of the electroactive species in the electrolyte. Through a combination of equations (1.3) and (1.4), the relationship between formal potential and standard electrode potential is given by:

$$E_f^0 = E^o + \frac{RT}{nF} ln \frac{\gamma_A}{\gamma_B} \qquad (1.5)$$

It worth mention that, considered the interaction energy of ions in the solution, two Chemists, Debye and Hückel proposed their limiting law to estimate the activity coefficient:[3]

$$ln\gamma_i = -Az_i^2\sqrt{I} \qquad (1.6)$$

where γ_i is the activity coefficient of species i, z_i is the charge number of species i, I is the ionic strength and A is a constant depends on temperature.

1.2 The Electrode/Solution Interface

A potential applied at an electrode-electrolyte interface can disturb equilibrium of the type described in the previous section and results in an electrical current flow through the interface; voltammetry is the study of that measured current as a function of potential. The mechanisms of this current flow process under the applied potential can be categorised into two types: Faradaic and non-faradaic processes.

1.2.1 Faradaic Processes

'Faradaic' processes involve the electron transfer between the electrode-electrolyte interface.[4] The electroactive species in the solution can either be oxidised or reduced depending on the direction of the flow of electrons. The amount of electroactive species involved in the electrochemical reaction is proportional to the amount of charge transferred, described by Faraday's law:

$$q = nNF \tag{1.7}$$

where q is the charge passed during the process, n is the number of electrons transferred per molecule, N is the number of moles of electroactive species involved in the electron transfer process and F is the Faraday constant. The magnitude of charge for one mole of electrons is 96485 C, and thus the Faraday constant equals 96485 $\mathrm{C \cdot mol^{-1}}$.

1.2.2 Non-Faradaic Processes

Under some circumstances, no charge transfer occurs over a range of potentials at a given electrode-electrolyte interface because such charge transfer reactions are kinetically or thermodynamically unfavourable. Adsorption and desorption processes can occur and the electrode-electrolyte interface structure can change with varying potential or solution composition, leading to a transient flow of charge. These processes are called non-Faradaic processes.

The flow of current results from non-Faradaic processes represents capacitative currents, i_c, and can be approximately described following a potential step as a function of time by:

$$i_c = \frac{AE}{R_s} e^{-t/R_s C_d} \tag{1.8}$$

where E is the magnitude of potential step, A is the area of electrode, R_s represents the resistance of the solution, t is the time and C_d is the double layer capacitance. For a linear potential sweep at a sweep rate v ($V \cdot s^{-1}$), i_c can be expressed by:

$$i_c = AvC_d(1 - e^{-\frac{t}{R_s C_d}}) \tag{1.9}$$

where at long times, a steady state value of AvC_d can be reached.

Modern experimental conditions are designed to minimise the non-Faradaic current so that the Faradaic current, which is the primary interest in electrochemistry, is the major signal measured. However, non-Faradaic current cannot be fully compensated, and a microelectrode with a small electrode radius is often required in experiments at high scan rate v.

1.2.3 The Electrical Double Layer

The current flow caused by the structure change of electrode/solution interface as a result of an applied potential arises from non-Faradaic processes, and the charging/discharging of the electrical double layer capacitance is the simplest case of a system in which only non-Faradaic processes occur.

A potential difference will develop across an electrode/solution interface due to the charge separation between the interfaces when an electrode is immersed in the electrolyte. This causes ion re-orientation in the immediate vicinity of the electrode surface so as to maintain local charge neutrality which leads to the formation of an electrical double layer. The electrical double comprises two distinct layers: a compact layer and a diffuse layer, shown in **Figure 1.1**. The compact layer refers to the ionic or uncharged species, both from the solvent or solute, adsorbed at the site of closest approach to the electrode surface. This layer, is located within the so-called Outer Helmholtz Plane (OHP).[5,6] The OHP passes through the centres of the ions at the distance of their immediate vicinity to the electrode. This plane is named after Helmholtz who first proposed a simple double layer model where two rigid layers of opposite polarity formed at the interface between the electrode and the solution. Gouy[7] and Chapman[8] later treated the ions as point charges and proposed the idea of a diffuse double layer, where potential dropped approximately exponentially. Stern[9] further improved the model by recognising that the ions are of finite dimensions and that the double layer indeed comprises *both* an Outer Helmholtz Plane and a diffuse layer. In this model, the potential between the electrode (Φ_M) and the Outer Helmholtz Plane (Φ_{OHP}) dropped linearly, followed by an exponentially decrease to the bulk solution (Φ_S). Grahame[10] later suggested that there is an Inner Helmholtz Plane (IHP) as some ions lose their solvation shell and specifically adsorbed to the electrode. The distance from electrode surface to the centre of these specifically adsorbed ions is referred to the IHP. Bockris *et al.*[11] also made further refinements to this model but the Gouy-Chapman-Stern model is generally adequate to qualitatively describe the interfacial region.

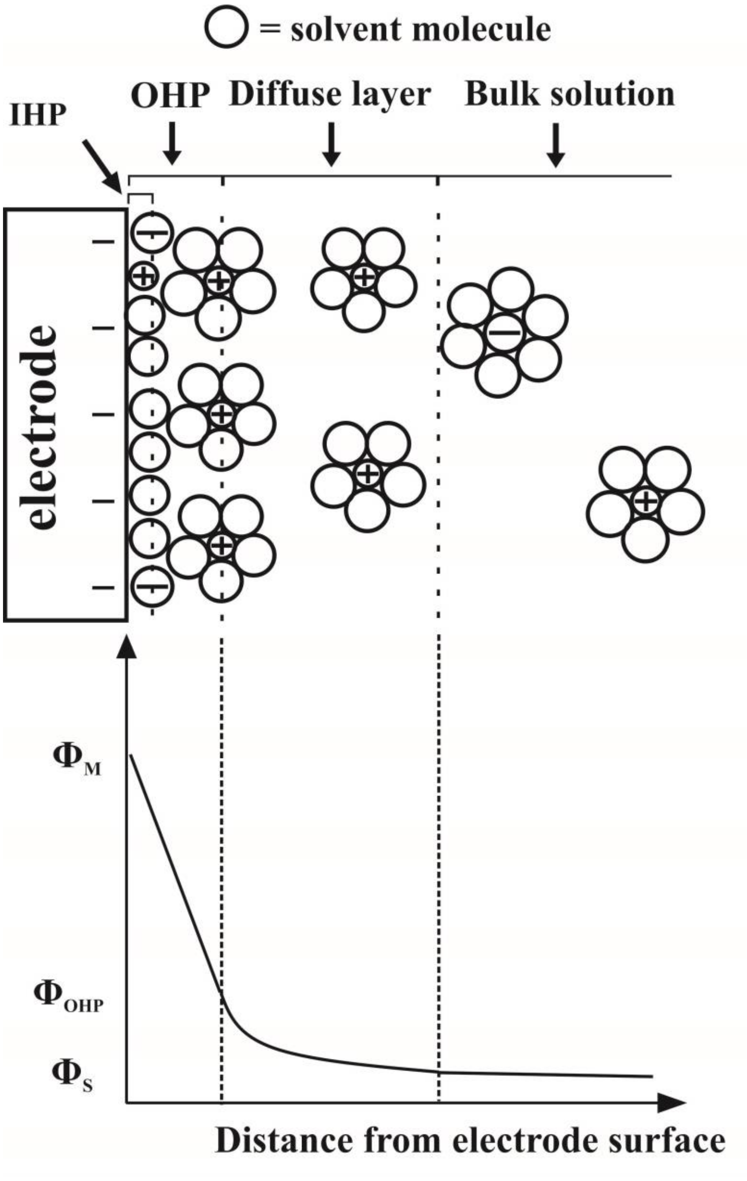

Figure 1.1: A schematic diagram of the electrical double layer.

1.3 Mass Transport

Electrode processes require that the electroactive species is transported from bulk solution to the electrode surface. Three types of mass transport can induce the motion of the molecules and ions: diffusion, migration and convection. These are introduced below.

1.3.1 Diffusion

Diffusion is the movement of species in solution in response to a concentration gradient. In an electrochemical reaction, the electroactive species near the electrode surface is consumed and hence its concentration is locally decreased. A depletion layer (‘diffusion layer’) is formed near the electrode surface and the resulting concentration gradient will drive the movement of fresh species to replenish the depleted region. The rate of diffusion is described by Fick’s first law:[12]

$$j_d = -D\frac{\partial c}{\partial x} \tag{1.10}$$

where j_d is the diffusive flux of a species, c is the concentration of electroactive species and x is the distance away from the electrode, thus $\frac{\partial c}{\partial x}$ is the concentration gradient in the direction from x to a plane surface, and D is the diffusion coefficient which describes the ease with which a species move through the solution. The latter is given by:

$$D = \frac{\delta x^2}{2\delta t} \tag{1.11}$$

where δt is defined as the time interval in which an electroactive particle moves a mean square distance of (δx^2).

Derived from Fick’s first law, Fick’s second law describes the rate of concentration variation at a point x:

$$\frac{\partial c}{\partial t} = D\frac{\partial^2 c}{\partial x^2} \tag{1.12}$$

which can be further modified to apply to a 3D system:

$$\frac{\partial c}{\partial t} = D\frac{\partial^2 c}{\partial x^2} + D\frac{\partial^2 c}{\partial y^2} + D\frac{\partial^2 c}{\partial z^2} \tag{1.13}$$

Equation (1.13) can be used to describe the rate of change of concentration around an electrode surface.

Diffusion to an electrode surface can be divided in to two types: linear and convergent. The electrode radius, *r*, and the size of the diffusion layer (the thickness of the depletion region near the electrode), *d*, are used to determine which of these two limiting diffusion cases to be applied:

$$d = 6\sqrt{Dt} \tag{1.14}$$

where *t* is the experimental time and *d* is a function of time. If $d << r$, linear diffusion dominates.[1] Examples include short time experiments or experiments using a macroelectrode (usually millimetres of radius). If $d >> r$, then convergent diffusion occurs. This will normally happen for long experiment times or if a microelectrode is employed (usually micrometres of radius). These two types of diffusion are shown in **Figure 1.2**.

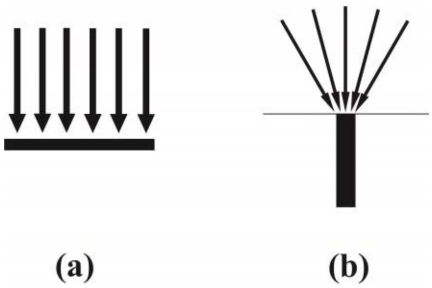

Figure 1.2: a) Linear and b) convergent diffusion to the electrode surface.

1.3.2 Convection

Convection is defined as the movement of the particles as a result of mechanical force(s) exerted in a solution, more specifically, natural convection, which is caused by density and thermal gradients, and forced convection, which occurs due to external forces such as stirring, vibration and gas bubbling through the solution. Natural convection is undesirable and unpredictable, although it not significant at short time scales on the order of 10 seconds.[13-15] Forced convection, comparatively, is several orders of magnitude greater and more predictable than natural convection and hence can be applied to overwhelm the influence of natural convection. The convection flux j_c is given by:

$$j_c = c \cdot v(x) \tag{1.15}$$

where $v(x)$ is the velocity of a solution at a point x.

1.3.3 Migration

Migration is defined as the motion of a charged species under an electric field.[16] When a potential is applied, a potential gradient will be established in the interfacial region between the electrolyte and working electrode. This potential gradient lead to a migration of charged particles attracted or repelled from the electrode electrostatically. The migration flux, j_m, down the direction of the potential gradient, $\frac{\partial \Phi}{\partial x}$, is described by:

$$j_m = -uc\frac{\partial \Phi}{\partial x} \tag{1.16}$$

where u is the mobility of the charged particles, c is the concentration. The mobility is the limiting velocity of the charged species, which is given by the Einstein-Smoluchowski equation:[16]

$$u = \frac{|z|FD}{RT} \tag{1.17}$$

where z is the charge of the migrating ions, F is the Faraday constant, D is the diffusion coefficient, R is the universal gas constant and T is the temperature. It is desirable to eliminate migration because it may severely complicate effects in electrochemistry.[2] To do this, an excess amount of inert and more concentrated, usually 50 – 100 times more concentrated than the analyte,[2] supporting electrolyte should be added to compress the electric field within the double layer, maintaining the mass transport to and from the electrode by diffusion only. Addition of supporting electrode provides other advantages such as increased conductivity, and, a minimised ohmic drop effect which is caused by the solution resistance arises from the physical distance between working and reference electrode. Supporting electrolyte also constrains the double layer to within a 10 – 20 Å region, facilitating the quantum tunnelling of electrons between the electrode and electroactive species. Furthermore, supporting electrolyte can keep the solution near a constant ionic strength so that can fix the formal potential of the redox couples.

1.4 Heterogeneous Electron Transfer

After the discussion of three principle types of mass transport, this section focuses on the Faradaic current resulting from electron transfer reaction in terms of electron transfer kinetics.

1.4.1 The Butler-Volmer Model

The Butler-Volmer model is the most widely accepted model of heterogeneous electron transfer kinetics originally developed independently by Butler[17] and by Volmer[18]. A simple one electron transfer reaction can be used to describe the Butler-Volmer model:

$$\mathrm{A} + \mathrm{e}^{-} \underset{k_b}{\overset{k_f}{\rightleftharpoons}} \mathrm{B} \tag{1.18}$$

in which A is reduced to B, k_f and k_b are the rate constants for the forward and backward heterogeneous electrochemical processes, respectively. Current flow is proportional to the forward and backward rate constant the concentration of species A, $[A]_0$, and B, $[B]_0$ at the surface of the electrode. Thus the overall current, i, is the summation of the currents for the forward and backward reactions:

$$i = FA(k_f[\mathrm{A}]_0 - k_b[\mathrm{B}]_0) \tag{1.19}$$

where F is the Faraday constant, A is the area of the electrode. The two rate constants can be expressed using transition state theory as:

$$k_f = k^0 \exp(-\frac{\alpha F\left(E - E_f^0\right)}{RT}) \tag{1.20}$$

$$k_b = k^0 \exp(\frac{\beta F\left(E - E_f^0\right)}{RT}) \tag{1.21}$$

where k^0 is the standard electrochemical rate constant, $\left(E - E_f^0\right)$ is the overpotential (the difference between the applied potential E and the formal potential E_f^0), and α, β are the transfer coefficients, which describes the symmetry of the energy barrier for the electron transfer process (Note that normally $\alpha + \beta = 1$ but in extremely irreversible reactions the sum of α and β may not be one due to the considerable asymmetry of the energy barrier).[19] Therefore, the current, i, in equation (1.18) can be expressed by:

$$i = FAk^0([\mathrm{A}]_0 \exp\left(\frac{-\alpha F\left(E - E_f^0\right)}{RT}\right) - [B]_0 \exp\left(\frac{(1-\alpha)F\left(E - E_f^0\right)}{RT}\right)) \quad (1.22)$$

The above equation is the Butler-Volmer equation. This equation can be combined with mass transport equations for theoretical modelling of the current response.

1.4.2 Electrochemical Reversibility

In an electrochemically reversible system, the electron transfer process is sufficiently fast that equilibrium is reached on the electrode surface in a short time and maintained regardless of the applied potential. Under this condition, the Butler-Volmer equation (1.22) can be simplified to the Nernst equation:[1]

$$E = E_f^0 + \frac{RT}{F} ln \frac{[A]}{[B]} \quad (1.23)$$

In contrast, a system is classified as 'irreversible' if the electron transfer is slower than the rate of mass transport. In such cases, equilibrium is not achieved at potentials around E_f^0 on the timescale of the experiment, and the reaction has to be driven under a significantly large overpotential. However, many electrochemical systems are found to display intermediate electrode kinetic are hence termed as 'quasi-reversible'.

In the voltammogram of an electrochemically irreversible process, there is a region of potential in which the current depends exponentially on potential between the limiting current plateau and the equilibrium potential, expressed by the following form of the Butler-Volmer equation:

$$i = i_0 \exp(-\frac{\alpha F\left(E - E_f^0\right)}{RT}) \tag{1.24}$$

where i_0 is the standard exchange current (the current extrapolated to zero overpotential). And can be further rearranged to:

$$\ln\left(\frac{i_0}{i}\right) = \frac{\alpha F\left(E - E_f^0\right)}{RT} \tag{1.25}$$

which is called the Tafel equation.[16,19] The exchange current and transfer coefficient can be determined using the above Tafel equation.

1.5 Homogeneous Processes

Electrochemical methods can be used to study kinetics and mechanisms for electrochemical processes with coupled homogeneous chemical steps where the effect on voltammetric behaviour can be significant. The most commonly used notation to describe such processes was developed by Testa and Reinmuth,[20] with a letter ‘E’ to represent heterogeneous electron transfer steps and a letter ‘C’ to describe a homogeneous step. Next, the most frequently encountered examples such as EC, ECE and DISP mechanisms are introduced briefly.

1.5.1 EC Mechanism

EC processes represent the cases where the product of a heterogeneous electron transfer reaction is unstable and undergoes a follow-up homogeneous reaction:

$$A + e^{-} \rightleftharpoons B \quad (1.26)$$

$$B \rightarrow C \quad (1.27)$$

in which the overall product, C, is electrochemically inert in the potential window where the precursor, A, is reduced. An EC_2 mechanism is denoted if the homogeneous step (1.27) involves a second order reaction of B. In addition, if the homogeneous step (1.27) involves the catalytic regeneration of the precursor, A, then EC' is used to represent the mechanism:

$$A + e^{-} \rightleftharpoons B \quad (1.28)$$

$$B + Z \rightarrow A + Y \quad (1.29)$$

It is seen that the net results of the process is the transformation of reactant Z to product Y, catalysed by A, which is regenerated.

1.5.2 ECE Mechanism

ECE mechanism will be used if the product of the homogeneous step is electrochemically active at the potentials where first heterogeneous electron transfer occurred and is itself reduced (or oxidised) immediately:

$$A + e^{-} \rightleftharpoons B \quad (1.30)$$

$$B \rightarrow C \quad (1.31)$$

$$C + e^{-} \rightleftharpoons D \quad (1.32)$$

1.5.3 DISP Mechanism

It worth mentioning that the second electron transfer of the homogeneous reaction product, C, as shown in equation (1.31) may occur either at the electrode surface via reaction (1.32) or in bulk solution via disproportionation,[1] as described by DISP mechanism below:

$$A + e^{-} \rightleftharpoons B \tag{1.33}$$

$$B \rightarrow C \tag{1.34}$$

$$B + C \rightleftharpoons A + D \tag{1.35}$$

Two further possibilities can be classified within the DISP mechanism, DISP 1 and DISP 2, depending on whether reaction (1.34) or (1.35) is the rate determining step. The mechanism is DISP 1 if reaction (1.34) is rate determining whereas DISP 2 will be the mechanism if reaction (1.35) is rate determining. DISP 2 is readily identified as the forward peak potential has dependences on both [A] and on the scan rate (20 mV/decade). However, ECE and DISP 1 mechanism have same rate determining step and give identical responses to [A] and forward peak potential scan rate dependence (30 mv/decade). These ambiguities can be distinguished by double potential step chronoamperometry.[21]

1.6 Voltammetric Techniques

Various voltammetric techniques exist to help study the current response when a voltage is applied to an electrode. This section outlines the techniques employed in this thesis notably ‘potential step chronoamperometry’ and ‘cyclic voltammetry’.

1.6.1 Potential Step Chronoamperometry

Potential step chronoamperometry is a commonly used technique to simultaneously study the concentration and diffusion coefficient of electroactive species.[2,22,23] In a potential step experiment, the potential is initially held at a value E_1, as shown in **Figure 1.3a**, where no Faradaic current is generated, and then the potential is stepped to a value, E_2, where the electrochemical reaction is fully driven in a diffusion controlled way.

For a macroelectrode, the current – time response is described by the planar diffusion governed Cottrell equation (1.36). The initial current is large due to a steep concentration gradient close to the electrode. The Faradaic current then decays rapidly due to the depletion of electroactive species in the close vicinity of the electrode surface,

$$i_d = nFAc\sqrt{\frac{D}{\pi t}} \tag{1.36}$$

where i_d is the diffusion limited current, n is the number of electrons transferred, A is the surface area of the electrode, c is the concentration of the electroactive species in the bulk solution, D is the diffusion coefficient of the electroactive species and t is time. It can be easily seen that according to equation (1.36) at sufficiently long time, i_d tends to zero; and either n, A, c or D can be obtained from the gradient of i vs. $1/\sqrt{t}$ plot provided the other three parameters are known for a system using a macroelectrode if the current response is solely controlled by diffusion.

For a microelectrode, the current – time response is dictated by equation (1.37):

$$i = 4nFcDrf(t) \tag{1.37}$$

where r is the electrode radius and $f(t)$ is given by:

$$f(t) = 0.7854 + 0.8862\sqrt{\frac{r^2}{4Dt}} + 0.2146\exp\left(-0.7823\sqrt{\frac{r^2}{4Dt}}\right) \tag{1.38}$$

According to equations (1.37) and (1.38), at short times, the response current i is a Cottrellian current which depends on $ncD^{1/2}t^{-1/2}$; at long times, a steady state current is recorded and can be described as $i_{ss} = 4nFrDc$. Thus at long times r can be derived with the known c, D, n values. However, by analysis of the entire transient both nc and D can be determined.

The resulting current against experimental time is shown in **Figure 1.3b**. The Shoup and Szabo equation is the most widely used numerical method to describe the chronoamperometric response at a microelectrode which is reported to simulate the current response over all time scale with an error ≤ 0.5%.[22] Chapter 4, section 4.2 and 4.3 gives a more detailed analysis of the application of the Shoup and Szabo equation.

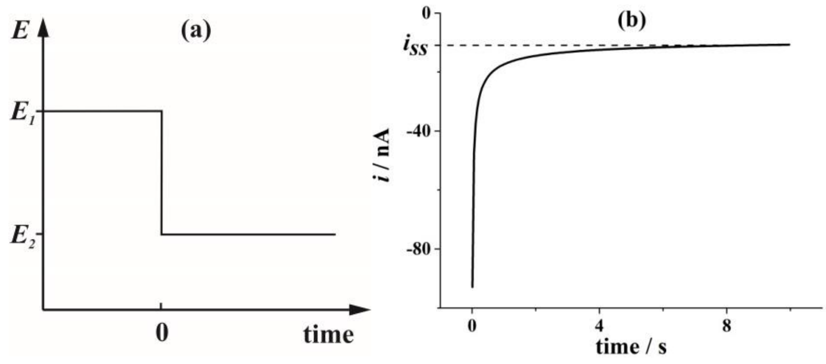

Figure 1.3: (a) Potential – time profile in a chronoamperometry experiment; (b) the resultant current – time response at a microelectrode.

1.6.2 Cyclic Voltammetry

Cyclic voltammetry is the measurement of current as the potential varied (usually linearly) from an initial value, E_1, where no reaction occurs to a final value, E_2, where the reaction is fully driven. The current is further recorded as the potential is then swept back to E_1. Both the forward and backward sweeps are made at a constant scan rate, v. **Figure 1.4** shows the potential waveform of cyclic voltammetry. Such experiments generate plots of i vs. E and are called 'cyclic voltammograms' (CVs).

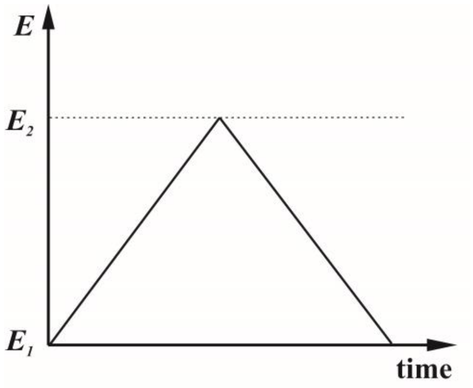

Figure 1.4: Potential waveform of cyclic voltammetry.

Various factors such as electrode kinetics, electrode area, and the mass transport type can influence the shape and position of a cyclic voltammogram, thus the voltamogram obtained using a macroelectrode can be very different from that with a microelectrode, and this will be discussed below.

1.6.2.1 Voltammetry at Macroelectrodes

At a macroelectrode, planar diffusion plays a dominate role, and typical voltammograms are shown in **Figure 1.5** for a simple one-electron oxidation reaction.

$$A \rightleftharpoons B + e^{-} \tag{1.39}$$

The three voltammograms shown in **Figure 1.5** correspond to reversible (black line), quasi-reversible (red line) and irreversible (blue line) electron transfer processes. The curved arrows in the figure illustrate the forward and backward sweeps for all voltammograms.

For the reversible process the initial potential is not positive enough to induce the oxidation of species A, hence no current is recorded. As the potential increases, the oxidation of A occurs and the current increases approximately exponentially along with the oxidation of the species A. When the current reaches the peak, the rate of electron transfer equals the diffusion rate of A at that particular potential. At even higher potentials, the current begins to decrease as the mass transport is slower compared to the rate of electron transfer, and the replenishment of species A from bulk solution is not sufficient in comparison to the consumption of species A at electrode surface.

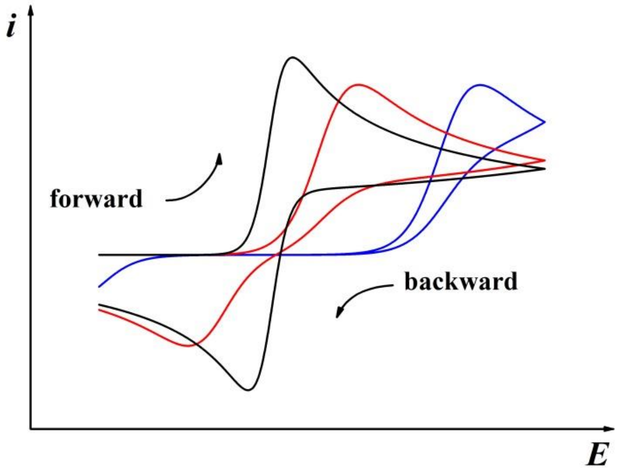

Figure 1.5: Planar diffusion controlled cyclic voltammetric response for reversible (▬), quasi-reversible (▬) and irreversible (▬) processes at a macroelectrode.

The peak current, i_p, for a reversible electron transfer process can be described by Randles-Sevčik equation:[24,25]

$$i_p = (2.69 \times 10^5)n^{\frac{3}{2}}AD^{\frac{1}{2}}v^{\frac{1}{2}}c \tag{1.40}$$

where n is the number of electrons transferred (n = 1 in this case), A is the surface area of the electrode, v is the scan rate, D is the diffusion coefficient and c is the concentration of electroactive species in bulk solution. An analogous process occurs in the reverse sweep where species B is reduced to A. For the fully reversible case (black line shown in **Figure 1.5**), the forward and backward peak potentials are separated for a value of $\Delta E_{pp} = \frac{2.303RT}{nF}$ (corresponding to $\frac{59}{n}$ mV at 298 K). Peak potentials are independent of scan rate employed, but at high scan rate, less depletion of species at the electrode surface occurs, leading to a thinner diffusion layer and a steeper concentration gradient. Consequently, more flux of electroactive species move towards the electrode and a larger peak current is generated. Therefore, the value of the peak current is linearly proportional to the square root of scan rate as shown in equation (1.40).

Before moving to quasi-reversible and irreversible processes, it is important to explain the definition of these terms. The key is the rate of mass transport to the electrode and the standard electrochemical rate constant, k^0. The rate of electron transfer kinetics is determined by k^0 whilst the rate of mass transport is measured by m_T, which is the mass transport coefficient:[1]

$$m_T = \frac{D}{d} \tag{1.41}$$

where d is the thickness of the diffusion layer, depending on time, t, approximately given by:

$$d \sim \sqrt{Dt} \tag{1.42}$$

The time, t, used to scan the voltammogram is related to the scan rate, v:

$$t \sim \frac{RT}{Fv} \tag{1.43}$$

where estimated to an order of magnitude is:

$$m_T \sim \sqrt{\frac{DFv}{RT}} \tag{1.44}$$

Therefore, in the cyclic voltammetric experiment, if $k^0 >> m_T$, the electrochemical process is a reversible process; if $k^0 << m_T$, the process will be irreversible. The transition between reversible and irreversible limit can be evaluated by a parameter, Λ, introduced in a classical paper by Matsuda and Ayabe:[26]

$$\Lambda = \frac{k^0}{(FDv/RT)^{1/2}} \tag{1.45}$$

Matsuda and Ayabe suggested the following ranges for the three types of reversibility at macroelectrodes:

Reversible: $$\Lambda \geq 15,\ k^0 \geq 0.3v^{\frac{1}{2}}\ cm \cdot s^{-1} \tag{1.46}$$

Quasi-reversible: $$\begin{gathered} 15 > \Lambda > 10^{-3} \\ 0.3v^{1/2} > k^0 > 2 \times 10^{-5} v^{1/2}\ cm \cdot s^{-1} \end{gathered} \tag{1.47}$$

Irreversible: $$\Lambda \leq 10^{-3},\ k^0 \leq 2 \times 10^{-5} v^{1/2} cm \cdot s^{-1} \tag{1.48}$$

These results involve an assumption that the transfer coefficient, α, equals 0.5 and apply to room temperature, 298 K.

As explained above, when the electrode kinetics is sufficiently slow in accordance with equation (1.48), the resulting voltammogram is classified as irreversible, as shown by the blue coloured scan in **Figure 1.5**. A smaller peak current and a much broader wave shape and can be seen compared to the reversible case. The peak current, i_p, at 298 K, can be calculated by:

$$i_p = (2.99 \times 10^5) n(\alpha{+}n')^{1/2} A D^{\frac{1}{2}} v^{\frac{1}{2}} c \tag{1.49}$$

where n is the number of electrons transferred, α is the transfer coefficient of the electron transfer in the rate determining step, n' is number of electrons transferred before the rate determining step. Although in the irreversible case, the peak current is proportional to the square root of scan rate, as in the reversible case, there are some differences compared to the reversible case. It can be seen from **Figure 1.5** that a large overpotential relative to the formal potential is required to drive the electron transfer which results in a peak potential more positive than that of the reversible case. A similar effect can also be found in the backward process where the reduction back peak occurs at a more negative potential. Furthermore, the peak to peak separation, ΔE_{pp} is given by:

$$\Delta E_{pp} = \frac{RT}{\alpha F} \ln(v) + constant \tag{1.50}$$

which shows that the peak to peak separation increases at higher scan rates.

In a quasi-reversible process, the wave shape of the voltammogram is intermediate between the reversible and irreversible cases, as shown by the red coloured line in **Figure 1.5**. The peak to peak separation is larger than that for reversible limit (~ 59 mV at 298 K) and also depends on the voltage scan rate. The peak current in a quasi-reversible process does not have a linear dependence on the square root of scan rate.

1.6.2.2 Voltammetry at Microelectrodes

When the radius of the electrode is sufficiently small, usually a few microns, convergent diffusion occurs at the electrode surface, and the resulting voltammogram is remarkably different to that seen for a macroelectrode. **Figure 1.6** shows the typical voltammogram obtained using a microelectrode. It is seen that a voltammetry with a steady state current is reached instead of a peak-shaped voltammogram. This occurs because of the continuously replenishment of the electroactive species due to the fast rate of mass transport to the surface of a microelectrode. The steady state current is expressed by equation (1.51), which has been described above:

$$i_{ss} = 4nFcDr \tag{1.51}$$

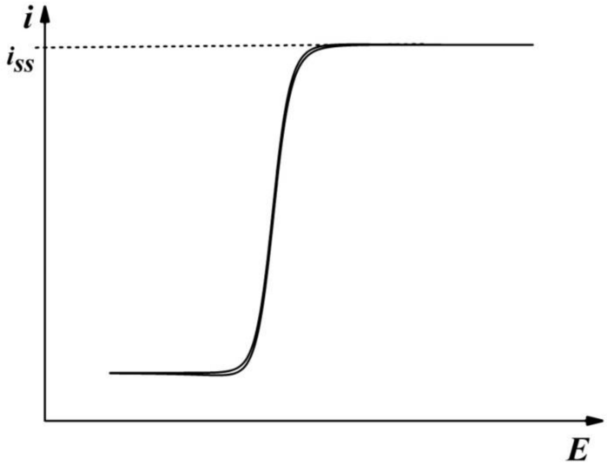

Figure 1.6: A typical steady state cyclic voltammogram at microelectrode.

However, it should be noted that planar diffusion, rather than abovementioned convergent diffusion can be still dominate even using a microelectrode when the scan rate is sufficiently high or if the electroactive species possess a very low diffusion coefficient, when a peak-shaped voltammogram occurs. The case of low diffusion coefficient is commonly encountered in the room temperature ionic liquid discussed in the thesis.

References

(1) Compton, R. G.; Banks, C. E. *Understanding Voltammetry*; 2nd ed.; Imperial College Press: London, 2011.

(2) Bard, A. J.; Faulkner, L. R. *Electrochemical Methods: Fundamentals and Applications*; 2nd ed.; Wiley, 2000.

(3) Debye, P.; Hückel, E. *Physik. Zeit.* **1923**, *24*, 185.

(4) Faraday, M. *Experimental Researches in Electricity*; Bernard Quaritch: London, Uk, 1839.

(5) Helmholtz, H. *Annalen der Physik* **1879**, *243*, 337.

(6) Helmholtz, H. *Annalen der Physik* **1853**, *165*, 211.

(7) Gouy, G. *Compt. Rend.* **1910**, *149*, 654.

(8) Chapman, D. L. *Phil. Mag.* **1913**, *25*, 475.

(9) Stern, O. *Z. Elektrochem. Angew. Phys. Chem.* **1924**, *30*, 508.

(10) Grahame, D. C. *Chem. Rev.* **1947**, *41*, 441.

(11) Bockris, J. O. M.; Devanathan, M. A. V.; Mueller, K. *Proc. Phys. Soc. Ser. A* **1963**, *274*, 55.

(12) Fick, A. *Annal. Phys. Chem.* **1855**, *94*, 59.

(13) Bamford, C. H.; Tipper, C. F. H.; Compton, R. G. *Electrode Kinetics: Principles and Methodology*; Elsevier, 1986.

(14) Amatore, C. A.; Deakin, M. R.; Wightman, M. *J. Electroanal. Chem.* **1986**, *206*, 23.

(15) Amatore, C.; Deakin, M. R.; Wightman, M. *J. Electroanal. Chem.* **1987**, *225*, 49.

(16) Rieger, P. H. *Electrochemistry*; 2nd ed.; Chapman and Hall, Inc.: New York, USA, 1994.

(17) Butler, J. A. V. *Transactions of the Faraday Society* **1924**, *19*, 729.

(18) Erdey-Gruz, T.; Volmer, M. *Z. physik. Chem.* **1930**, *150*, 203.

(19) Fisher, A. C. *Electrode Dynamics*; Oxford University Press: Oxford, UK, 1998.

(20) Testa, A. C.; Reinmuth, W. H. *Anal. Chem.* **1961**, *33*, 1320.

(21) Nadjo, L.; Savéant, J. M. *J. Electroanal. Chem.* **1971**, *30*, 41.

(22) Shoup, D.; Szabo, A. *J. Electroanal. Chem. Interfacial Electrochem.* **1982**, *140*, 237.

(23) Paddon, C. A.; Silvester, D. S.; Bhatti, F. L.; Donohoe, T. J.; Compton, R. G. *Electroanalysis* **2007**, *19*, 11.

(24) Randles, J. E. B. *Trans. Faraday Soc.* **1948**, *44*, 327.

(25) Sevčik, A. *Collect. Czech. Chem. Commun.* **1948**, *13*, 349.

(26) Matsuda, H.; Ayabe, Y. *Z. Elektrochem.* **1955**, *59*, 494.

Chapter 2

Introduction to Amperometric Gas Sensors

In this chapter, an introduction to the history of, and recent developments in, amperometric gas sensing will be provided. The application of room temperature ionic liquids (RTILs), microelectrodes and porous electrodes in gas sensors are included, and are of direct relevance to the work reported later in this thesis.

2.1 Introduction

Gas sensors play ever-increasing roles in many areas including environmental monitoring, health and safety, and the automotive and aerospace industries, with a well-known example being the fire alarms for carbon monoxide detection.[1-5] A variety of chemical and physical principles are utilised to quantitatively measure the concentration of gases. Currently commercialised gas sensors are based on electrochemistry,[1,6-9] spectrometry[10-14] and luminescence.[15-18] **Table 2.1** illustrates different types of gas sensors and the various theoretical principles employed. Among different possible gas sensing techniques, the electrochemical technique offers superiorities in respect of high sensitivity, high portability, low cost, and low energy consumption.[1,19] However, their limited selectivity is, to some extent, a major drawback of the electrochemical sensors except in niche applications.

Table 2.1: Comparison of different types of gas sensors and principles

Type	Principle	Examples
Photoionisation detector	Detection of electrically charged gas excited by high energy photons from UV range	OV(organic vapours),[20-23] NO_2[24]
IR sensor	Detection of the radiation given off by gas	CO_2,[25] CO,[26] CH_4[27]
Fluorescence sensor	Comparison the difference of the excitation and emission wavelength	CO,[28] H_2S,[29] HCN[30]
Metal oxide semiconductor	Conductivity change of the metal oxide during adsorption and desorption of gas	H_2,[31,32] NH_3,[33,34] NO_2,[35] CO[36]
Catalytic gas sensor	Detection of the resistance difference before and after the oxidation of gas.	OV,[37] SO_2,[38] CH_4[39,40]
Electrochemical gas sensor	Measurement of current generated by reaction of gases at electrode	O_2,[41-43] NO_2,[44] H_2S,[45,46] OV[47]

Electrochemical gas sensors are classified into three main categories according to their different operating principles: potentiometric, conductometric and amperometric gas sensors.

Potentiometric gas sensors measure the potential between two electrodes (working and reference electrodes) when no external voltage is present; the measured potential is typically dependent on the logarithm of the concentration of dissolved gas in the analyte,[48] according to the Nernst equation introduced in Chapter 1. Potentiometric gas sensors are used to detect CO_2,[49-53] SO_2[54,55] and NH_3[56-58]. The sensing principle is thermodynamic which means all reactions related to the sensing process are at equilibrium.

Conductometric gas sensors measure the conductivity variation of a sensitive layer when they are in contact with gases.[59] During the process taking place on the sensitive layer, the resistance of the layer changes, and this is correlated to the concentration of the gases. Metal oxide semiconductors are mainly used as materials for the sensitive layers as they exhibit conductivity changes when exposed to gases.[60] Conductometric sensors are low cost and have a long life and can be used to detect NH_3, NO_2 and H_2.[61] Unfortunately, they are energy consuming as high temperatures are required for measurable gas responses, and the selectivity of the sensors is limited.

Amperometric gas sensors are most widely used to monitor the gas concentration in a variety of applications including medical care (eg. nitric oxide sensor), and human health (eg. carbon monoxide sensor) as they provide relatively high analytical performance at modest cost.[1] This type of gas sensor is based on the measurement of the current generated by the reaction of a gas at an electrode. Often the current is simply proportional to the concentration of the target gas when operated under appropriate diffusion-limited conditions. The signal can be measured at varied or fixed potential, although the fixed potential mode is mostly applied. The earliest successful amperometric gas sensor was designed by Clark *et al* at 1953 to measure the oxygen content in blood samples.[62]

In the following sections, the history and modern development of Clark type sensors are introduced along with their applications and limitations. Subsequently the recent advancement of amperometric gas sensors will be discussed in respect of the application of room temperature ionic liquids as solvents, and microelectrodes and porous electrodes as detectors. Detailed evaluation of potentiometric and conductometric gas sensor is not covered because the amperometric sensing technique is solely employed in this thesis.

2.2 Clark Type Sensor

2.2.1 The Clark Sensor

The original design of the oxygen sensor by Clark *et al* in 1953[62] included a power supply, a shiny platinum (Pt) button covered with cellophane as the cathode, and a potassium chloride-calomel electrode as the anode. A variable shunt was applied to compensate the current variation in the cathode. The anode tip was wrapped with saline-saturated cotton to improve the electrical contact. The cellophane covered Pt working electrode was an important innovation. The working electrode showed enhanced oxygen selectivity as the cellophane membrane allowed the penetration of oxygen but prevented interferences from other gases and red blood cells. After contact between oxygen and the Pt cathode, the measurement arose from the following two reduction steps:

$$O_2 + 2H_2O + 2e^- \rightarrow H_2O_2 + 2OH^- \tag{2.1}$$

$$H_2O_2 + 2e^- \rightarrow 2OH^- \tag{2.2}$$

A fixed potential (0.6 V) was applied between the working electrode (cathode) and the reference electrode (anode). The current was recorded by a galvanometer and was found to be proportional to the concentration of dissolved oxygen. The Clark sensor provided reproducibility, stability, sensitivity and high portability. It subsequently allowed the detection of blood oxygen both *in vitro* and *in vivo*. The development of the Clark sensor inspired numerous scientists to develop new generations of gas sensors based on the Clark type sensor. These will be introduced in the following section.

2.2.2 Modern Clark Type Gas Sensors

Modern amperometric gas sensors are typically designed on the principle of the original Clark type sensor, but which consists of a three-electrode system, a gas selective membrane and some electrolyte, as shown in **Figure 2.1**. The electrodes are connected to an external potentiostat. The target gas passes through the membrane into an electrolyte and then diffuses to the working electrode. The membrane is used to control the gas flow, prevent electrolyte leakage and ideally only allow the target gas to pass through. The target gas can then be either oxidised or reduced to produce a current flow depending on the nature of the gas. For instance, carbon monoxide (CO) can be oxidised to carbon dioxide (CO_2), resulting in the electrons flowing from the working electrode to the counter electrode through the external circuit. On the contrary, dissolved O_2 can be reduced to water, leading to electrons flowing from the counter electrode to the working electrode.

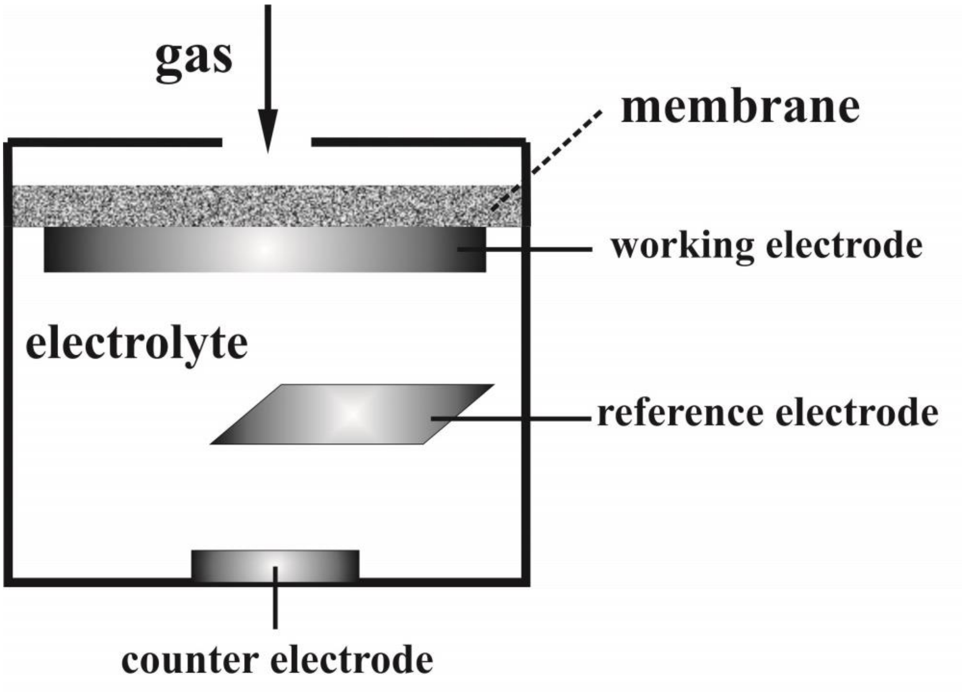

Figure 2.1: Schematic Clark type gas sensor. Note that the membrane and working electrode do not necessarily contact each other.

2.2.3 Practical Applications

The detection of CO in air for health and safety purposes since 1970s is one of the primary applications of amperometric gas sensors.[63] From 1970s onwards, additional applications of amperometric gas sensors were found in many fields. The amperometric gas sensors may possess advantages such as high sensitivity (~ ppm level), low cost, energy efficiency, durability, and high selectivity. Portability also makes amperometric gas sensors attractive because the measurement can be conducted ‘on the spot’ rather than requiring sampling and transporting back to a lab for analysis. After more than five decades of development with the advancement of nanotechnology, microfabrication and computational power, modern amperometric gas sensors employ various types of working electrodes, electrolytes and have reached maturity in various applications.[64]

2.2.3.1 Industry

Gases are monitored in many industries because the composition of the vapour phase is an important indicator in industrial activities. Amperometric gas sensors provide fast, low cost and 'on spot' measurement and thus are quite widely applied.[65-70] In the food processing industry, foodstuffs can produce volatiles with concentrations ranging from 1 to 1000 ppm which can be monitored by amperometric gas sensors. For example, the quality of olive oil can be easily measured with a gas sensor because old olive oil releases aldehydes.[67] Also in petrochemical refining, amperometric gas sensors are used to detect SO_2 and volatile organic aromatic compounds levels in exhaust gases.[71,72] In consumer goods manufacturing, (eg. detergents) gas sensors are used to detect the presence of contaminants or the consistency of the chemical product.[1]

2.2.3.2 Environment

Reflecting an increasing awareness of the hazards of environmental pollution, gas sensors suitable for environmental monitoring on emission and safety have become very important. Conventional analytical equipment for the analysis of air quality is often costly and bulky.[1] Thus it is important to develop a new generation of gas sensors which are cheap, highly selective, and small in size. Gas concentration detection limits from a few ppb to hundreds of ppm are also crucial for air quality analysis. Currently, working microelectrode sensors are being developed for these highly demanding tasks. [64] For instance, platinum or gold electrodes are employed in amperometric gas sensors to detect combustible gases (eg. CO, H_2, hydrocarbons),[73] nitrogen oxide gases (NO_x),[74] lean combustion gas control (to ensure burning fuel with an excess of air by measuring the air-fuel raio)[75] and selective measurement of olefins (eg. propene) with zinc oxide/platinum electrodes.[76] Multi-electrode amperometric gas sensors are now developed to simultaneously detect gas mixtures such as O_2 and NO or O_2 and combustible gases.[73] The key for multi-electrode development is that only one electrode reaction takes place at one electrode with the control of different applied potentials.

Indoor air quality measurement is receiving growing interest as exposure to environmental pollutants, even at trace levels, is extremely hazardous to health in the long term. To both accurately and conveniently monitor the trace level of pollutants, new sensors are required. Amperometric gas sensors are ideal as they cover all the requirement of low cost, small size, energy efficiency, etc. For example, the amperometric measurement of gaseous formaldehyde using gold electrode and sulphuric acid electrolyte has a detection limit of 13 ppb.[77] However, issues such as sensitivity, response time and durability still need to overcome for domestic applications.

2.2.3.3 Defence and Security

Amperometric gas sensors are used for defence and security purposes due to their energy efficiency and portability. Some examples include the detection of toluene or other toxins accumulating in garments in which the sensors can be embedded.[78] Furthermore, amperometric gas sensors with wireless function are applied in airports, battlefields and military bases for the detection of explosives/toxic gases and for early warning systems, specifically, the detection of mustard gas (which is highly skin corrosive), hydrogen cyanide (an extremely poisonous liquid that boils slightly above 25.6 ^{o}C), hydrogen peroxide (explosive) and TNT (explosive). [69,70,79-82] The challenges for amperometric gas sensors in these applications are longevity, reproducibility and low maintenance cost.

2.2.3.4 Medical

Accurate and quick diagnostic results can be provided with the aid of amperometric sensors. For example, the analysis of patient's exhaled air, excreted urine, and some body fluids may give useful information on some diseases, or metabolic conditions if some specific chemicals are detected. And the real-time monitoring by an amperometric sensor helps physicians better determine the recovery of patients. Some suggested applications are listed in **Table 2.2**:

Table 2.2: Some applications of amperometric gas sensors in medical field

Target gases	Symptoms
4-heptanone, benzaldehyde, *p*-cresol, phenol	phenylketonuria[83]
methylbutyric acids, 2-keto-3-methylvaleric acid, *p*-cresol	maple syrup urine disease[83]
3-methyl butyrolactone, isovaleric acid	isovaleric acidemia[83]
trimethylamine	trimethylaminuria[83]
nitric oxide	inflammatory disease[84]

2.2.4 Limitations of Clark Type Sensors

Despite the wide popularity of Clark type sensors, some limitations such as response time, lifespan, and sensitivity still constrain their application.

The response time is significantly influenced by the time taken for gases to diffuse through the membrane. **Table 2.3** compares the diffusion coefficients of O_2, D_{O_2}, in air, in water and in Nafion or polythene based polymer membranes.

Table 2.3: A comparison of O_2 diffusion coefficients, D_{O_2}, in three different media.

Media	$\boldsymbol{D_{O_2}}$ **/ cm^2·s^{-1}**
Air[85]	0.179
Water[85]	2.10×10^{-5}
Polymer membrane[86,87]	10^{-6}

It is seen from **Table 2.3** that in a polymer membrane, O_2 diffuses about an order of magnitude slower than in water. Herein, permeability is introduced to describe the penetration of permeate molecules through a membrane or interface. Permeability is expressed according to:

$$\frac{\delta p}{\delta t} = P\frac{\delta^2 p}{\delta z^2} \tag{2.3}$$

where P (= αD, where α is the gas solubility and D is the gas diffusion coefficient) is the permeability of the permeate molecule, p is the partial pressure in the medium, t is time and z is the distance to electrode surface. Typically, oxygen's permeability is 2.7×10^{-9} m^2·s^{-1}·atm^{-1} in water and 8×10^{-11} m^2·s^{-1}·atm^{-1} in polymer membrane.[88] It is worth stressing that the thickness of the membrane plays an important role on the diffusion time of gases as it takes longer time for a gas to diffuse through a thicker membrane before contacting the working electrode. The time taken for a gas to reach 90% steady state response, t_{90}, is typically used as an indicator for the speed of a sensor's response. **Table 2.4** shows t_{90} value for some gases. Note in **Table 2.4**, the electrolyte used is concentrated sulphuric acid, and for non-toxic gas O_2, potassium acetate aqueous solution is employed as the electrolyte. The membrane used is the most commonly employed Nafion based gas permeable solid polymer membrane.

Table 2.4: t_{90} values for some gases[89], electrolyte used for toxic gases NH_3, H_2S, SO_2 and NO_2 is concentrated sulphuric acid, and for non-toxic gas O_2, potassium acetate aqueous solution is employed. The membrane used is a gas permeable solid polymer membrane.

Gas	O_2	NH_3	H_2S	SO_2	NO_2
t_{90} / s	< 11	< 90	< 15	< 25	< 25

For a t_{90} longer than 10 seconds, some amperometric gas sensors become impractical as for some applications such as respiratory or combustion monitoring the response time needs to be as quick as within seconds or even less.[90] The sensitivity also depends on the membrane in some cases. Do *et al* reported an enhanced sensitivity[91,92] by employing a conductive polymer membrane (polyaniline /Au/Nafion) as both a selective membrane and a working electrode. In their report, no separate working electrode was needed but the sensitivity to NO was increased from 0.33 μA·ppm^{-1} to 2.28 μA·ppm^{-1}.

Another drawback of Clark type sensors is the electrolyte used in the electrochemical cell. Evaporative losses importantly lead to sensor failure. Conventional electrolytes may also boil or freeze at high or low temperatures, which again cause failure of the gas sensor. An amperometric gas sensor commonly has a 24 month lifespan when employed at 298 K, 60% relative humidity and within ± 20% of ambient pressure.[93] But it is expected to have a shorter lifespan when used in extreme conditions such as in an oil field where the temperature can vary from – 60 to + 60 ^{o}C.[94,95]

Commercial gas sensors typically use H_2SO_4/H_2O as electrolyte as this solution has a vapour pressure similar to average ambient conditions.[96] However, this solution should normally be used in the temperature range of -45 to 50 ^{o}C, thus applications in some real-world conditions, as described above, will shorten the lifetime. Furthermore, this electrolyte is designed to be used under 60% relative humidity, whereas the electrolyte may absorb water or evaporate when the external gas has a higher or lower relative humidity. AlphaSense reported that the solution has a 50 wt% loss under 0 to 20% relative humidity in two days and 100 wt% gain under 100% relative humidity in two days.[97] Therefore, frequent calibration is required when gas sensors are used in such environments. Additionally, H_2SO_4/H_2O electrolyte has an electrochemical window of around only 2 V which is relatively narrow for some gases to be observed, especially for volatile organic compounds and CO_2, SO_2 and H_2S which have fairly high oxidation and/or reduction potentials.[98-100]

Non-target gases may also influence the result of the target gas. RAE System Inc reported that,[101] in their O_2 sensor, 20 vol% CO_2 can lead to an increase of 6% in the reading, and more than 25 vol% CO_2 dramatically increases the reading for O_2 concentration due to the adsorption of CO_2 into potassium acetate electrolyte.

In the following section, recent developments which may overcome these drawbacks will be discussed.

2.3 Recent Advances

This section discusses the recent development of amperometric gas sensors which may overcome the above mentioned limitations in respect of solvents and electrodes.

2.3.1 The Application of Room Temperature Ionic Liquids as Electrolytes

Most organic compounds are electrically neutral molecules; by contrast, room temperature ionic liquids (RTILs) are ionic salts. By careful selection of bulky, asymmetric organic cations and inorganic or organic anions, they can be designed to melt at or below room temperature.[96] **Figure 2.2** shows some commonly used cations and anions of RTILs with their abbreviations. Sigma-Aldrich (www.sigmaaldrich.com), Merck (www.merckmillipore.co.uk /chemicals/ionic-liquids) and BASF (www.intermediates.basf.com/chemicals/ionic-liquids) are commercial supplier for high purity RTILs. The purity of RTILs can normally be assessed by electrochemistry,[102] high performance liquid chromatography (HPLC),[103-105] or X-ray photo-electron spectroscopy techniques.[106-108] RTILs have many special properties which make them potentially alternative electrolytes for amperometric gas sensors, and these will be discussed next.

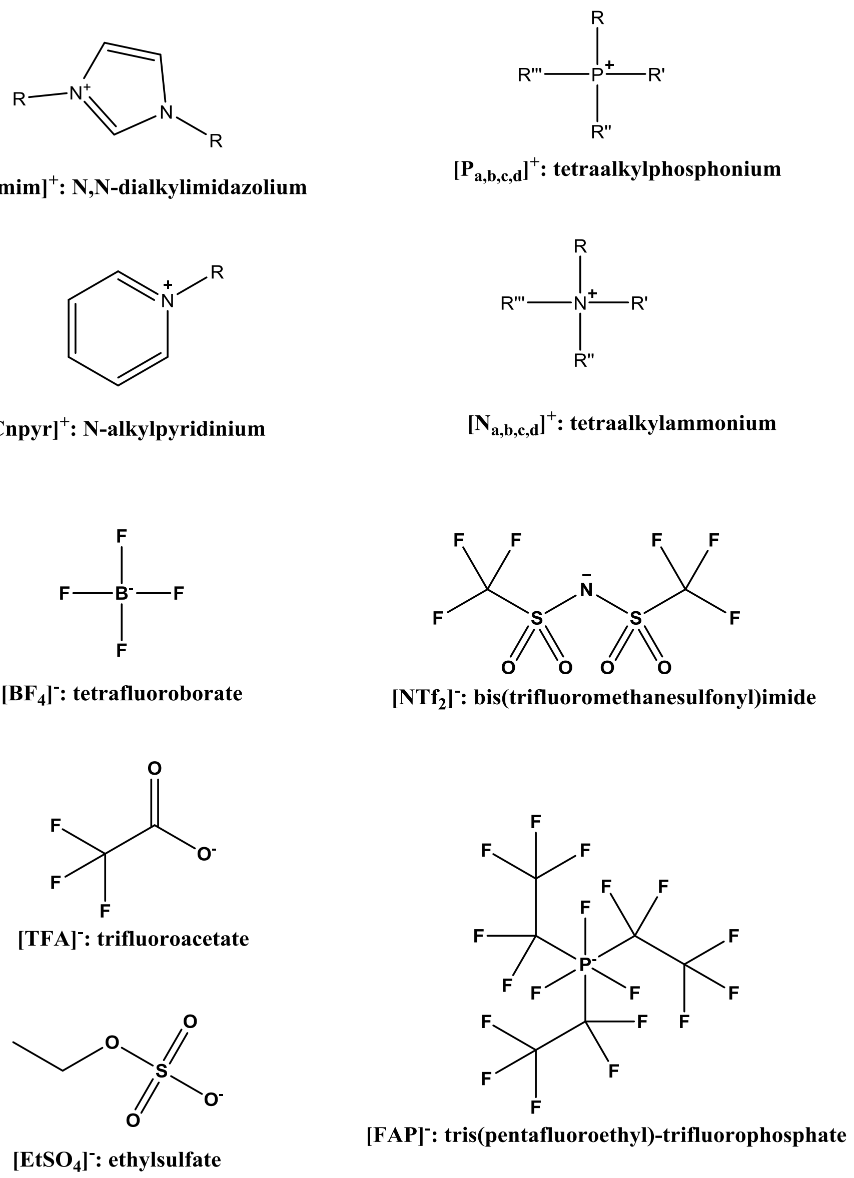

$[C_n mim]^+$: N,N-dialkylimidazolium

$[P_{a,b,c,d}]^+$: tetraalkylphosphonium

$[Cnpyr]^+$: N-alkylpyridinium

$[N_{a,b,c,d}]^+$: tetraalkylammonium

$[BF_4]^-$: tetrafluoroborate

$[NTf_2]^-$: bis(trifluoromethanesulfonyl)imide

$[TFA]^-$: trifluoroacetate

$[EtSO_4]^-$: ethylsulfate

$[FAP]^-$: tris(pentafluoroethyl)-trifluorophosphate

Figure 2.2: Structures, names and abbreviations of some commonly used cations and anions for room temperature ionic liquids

2.3.1.1 Electrochemical Window

The electrochemical window of a solvent is a measurement of the voltage difference between the anodic and cathodic breakdown potentials of the species (ions or molecules) which make up of the solvent.[109] The electrochemical windows for aqueous solutions are relatively narrow (~ 1.5 to 2 V) at most electrodes because of the reduction or oxidation of water itself.[110] This voltage ranges for aprotic solvents, on the other hand, are much wider: 5.0 V for acetonitrile, 3.5 V for dichloromethane and 4.4V for dimethylsulfoxide.[110] However RTILs typically have even wider electrochemical windows compared to aprotic solvents, with voltage ranges normally from 4.0 to 6.0 V,[111] due to the electrochemical stability of the constituent cation and anion that make up RTILs. Accordingly, the identities of the cation and anion of a RTIL are the key factors which decides the electrochemical window. It has been suggested that cations are often more influential on the window range.[112] Generally, the electrochemical window decreases with the order of $[P_{a,b,c,d}]^+$ > $[C_n\text{mPyrr}]^+$ > $[N_{a,b,c,d}]^+$ > $[C_n\text{mim}]^+$.[113] Although smaller, the anion composition also influences the potential window of the RTILs and the resulting window size generally follows the order of $[\text{FAP}]^-$ > $[\text{NTf}_2]^-$ > $[\text{PF}_6]^-$ ≈ $[\text{BF}_4]^-$ > halides (Br^-, I^-).

In addition to the composition, the electrochemical windows of RTILs are also affected by other factors. O'Mahony *et al*[114] reported that temperature and water content have an impact on the potential range of RTILs in the following order: vacuum-dried > atmospheric > wet; and 298 K > 318 K > 338 K. The explanations are as follows. First, water plays a negative effect on the electrochemical window and second, the rate constant of electron transfer increases at higher temperature and hence so does the ion breakdown. Although the electrochemical windows vary with different RTIL compositions, they are generally still larger than for molecular solvents, allowing the electrochemical study of species which normally reside outside of an accessible potential range in conventional solvents.

2.3.1.2 Inherent Conductivity

It is easily appreciated that RTILs exhibit good intrinsic conductivity (κ) since they are solely composed of ions. RTILs mostly have a comparable conductivity to organic solvents with supporting electrolyte, but a lower value compared to aqueous solutions with supporting electrolyte. **Table 2.5** lists the conductivities of some RTILs, and of water and organic solvent with supporting electrolyte.

Table 2.5: Conductivity, κ, of some RTILs, water and organic solvent, at 298 K.

Solvents	κ^{115} / mΩ^{-1}·cm^{-1}
[C_2mim][NTf_2]	9.2[116]
[C_4mim][NTf_2]	4.0[117]
[C_6mim][NTf_2]	0.22[118]
[C_6mim][FAP]	0.17[119]
[C_4mpyrr][NTf_2]	2.1[115]
[C_4mim][OTf_2]	2.9[120]
[C_4mim][BF_4]	0.36[118]
[$N_{6,2,2,2}$][NTf_2]	0.67[121]
[$P_{14,6,6,6}$][FAP]	1.1 (Merck)
Water	[a]13[122]
Acetonitrile	[b]7.6[122]
Dimethylsulfoxide	[b]2.7[122]
N,*N*-Dimethylformamide	[b]4.0[122]

[a]containing 0.1 M KCl as supporting electrolyte
[b]containing 0.1 M tetrabutylammonium perchlorate as supporting electrolyte

As shown in **Table 2.4**, conductivities show a large variation for different ionic liquids even they are all composed of ions. This is a reflection of structural differences. Bulky ions tend to move more slowly than smaller ions, as demonstrated by the conductivity of $[C_2mim][NTf_2]$ (9.2 $m\Omega^{-1}\cdot cm^{-1}$) and $[C_6mim][NTf_2]$ (0.22 $m\Omega^{-1}\cdot cm^{-1}$), since the alkyl substituent in the imidazolium group changes from ethyl to hexyl. Similarly, an aqueous solution with supporting electrolyte exhibits higher conductivity than most RTILs due to the small size of the charge carriers in aqueous solution. Hydrogen bonding may also lead to low mobility and conductivity.[123] By comparing the conductivities of butylimidazolium ($[C_4mim]^+$) RTILs, $[C_4mim][BF_4]$ has a conductivity of 0.36 $m\Omega^{-1}\cdot cm^{-1}$, which is an order of magnitude smaller than the others, a difference which can be attributed to the hydrogen bond formation around $[BF_4]^-$.

External conditions such as temperature and additives also influence the conductivity of RTILs. The dependence of RTIL's conductivity with temperature can be empirically described by Vogel-Tammann-Fulcher equation:

$$\kappa = AT^{-\frac{1}{2}}\exp(-B(T - T_0)) \tag{2.4}$$

where T_0 is the ideal gas temperature at which the conductivity drops to zero, A and B are empirically derived constants for each particular RTIL. Meanwhile, Chaban *et al*[124] reported that the addition of 15% acetonitrile into RTILs increased the conductivity more than 50 times. Similar observations were found with the addition of water, [125] methanol,[126] and dimethyl sulfoxide.[126] This can be explained by the decreased viscosity of RTILs which led to enhanced conductivity.

2.3.1.3 Volatility

The vapour pressure of a solvent reflects its volatility, and is measured when the liquid phase and gas phase are in equilibrium. A high vapour pressure indicates the probability of solvent evaporation so this property is very important for a solvent, especially when employed in extreme conditions such as high temperature and low pressure. RTILs only have a few mPa vapour pressure at 298 K. This is considerably small compared to conventional solvents, such water[127] (3.2 kPa), methanol (17 kPa)[128], ethanol (7.9 kPa)[128] and acetonitrile (13 kPa).[129] in general, much stronger inter-molecular forces give RTILs a much lower vapour pressure.

2.3.1.4 Thermal Stability

The thermal stability or the upper liquid limit of conventional solvents is generally defined by their boiling points.[130] For RTILs, the upper limit is usually defined as their decomposition temperature as this is normally lower than their boiling point due to their negligible vapour pressure. RTILs are reported to have decomposition temperatures from 573 – 674 K, with some RTILs stable even up to 725 K.[131] In comparison with water, which can only be used up to 373 K, RTILs have a clear advantage as a solvent to use in extreme conditions.

The decomposition of RTILs is ascribed to different mechanisms such as nucleophilic substitution,[132] thermal rearrangement[133] and dealkylation.[134] RTILs are found to have higher thermal stability for bigger anion sizes in an order of $[PF_6]^-$ > $[NTf_2]^-$ > $[BF_4]^-$ > halide[135,136] and with longer alkyl chain length (eg. from ethyl to octyl).[136] Clearly, RTILs have a temperature range large enough for general gas sensing applications.

2.3.1.5 Tunability

RTILs are frequently referred to as ‘designer solvents’ because RTILs can be tailored for different applications by modifying their constituent cation and anion. Mixing two RTILs is the simplest way to tune the composition and this method was reported to enhance the solubility of CO_2[137] and SO_2[138-140] due to the changed inter-molecular interaction activity between the ions. Thus Fox *et al* reported that a mixture of $[py_{1,5}][NTf_2]$ (*N*,*N*-methylpentylpyrrolidinium bis(trifluoromethylsulfonyl)imide) and $[pi_{1,5}][NTf_2]$ (*N*,*N*-methylpentylperidinium bis(trifluoromethylsulfonyl)imide) have same conductivity but lower viscosity when compared to individual components.[141]

2.3.1.6 RTILs Mediated Gas Sensor

Since RTILs have great potential to replace the conventional electrolytes used in amperometric gas sensors, as described above, various studies have been conducted in order to test the suitability of RTILs in gas sensing. Rogers *et al*[142] reviewed a variety of electrochemical reaction mechanisms for gas detection in RTILs. Some of mechanisms are shown in **Table 2.6**.

Table 2.6: Some electrochemical reactions of gases taking place in RTILs.[142]

Gas	Reaction mechanism
H_2S	$H_2S + e^- \rightarrow HS^- + H^\cdot$
NO_2	$NO_2 \leftrightharpoons NO_2^+ + e^-$
NH_3	$4NH_3 \rightarrow 3NH_4^+ + 1/2N_2(g) + 3e^-$
O_2	$O_2 + e^- \leftrightharpoons O_2^{\cdot-}$
SO_2	$SO_2 + e^- \leftrightharpoons SO_2^{\cdot-}$

The benefit of RTILs applied as electrolytes in gas sensors are summarised as follows.

a) Wide electrochemical windows allow various gases which normally lie outside of the potential window of conventional electrolyte to be detected in RTILs;

b) Low volatility and high thermal stability make RTILs ideal electrolytes to be used at high temperatures, as well as possibly eliminating the membrane in an amperometric gas sensor due to their considerably low volatility which prevent the solvent evaporation. In this way a membrane free sensor would be made with the RTIL simultaneously acting as membrane and electrolyte;

c) The intrinsic conductivity of RTILs eliminates the need for the addition of supporting electrolyte as in conventional solutions;

d) The RTILs' physical and chemical properties can be tuned by carefully selection of cation and anion for different purposes (see Chapter 6).

As described above, RTILs have ohmic resistances similar to that of organic solvents when applied in electrochemistry. However, using a microelectrode can minimise this effect. This is described in the next section.

2.3.2 The Application of Microelectrodes for Gas Sensing

Microelectrodes are defined as possessing at least one dimension within the micro-scale, which means 10 to 100 μm. Microelectrodes exhibit higher rates of mass transport, better signal to noise ratios and lower uncompensated resistances compared to macroelectrodes. Thus they are widely used in RTIL systems to compensate the RTILs' undesirably high viscosity and lower conductivity as compared to aqueous solvents with supporting electrolyte.

According to equation (1.13), the diffusion regime at a microelectrode is dominated by convergent diffusion. This requires that the experimental timescale the electrode radius, r, is much less than the thickness of the diffusion layer, d ($r \ll d$). Therefore, the electroactive species are driven both onto the surface and edge of the electrode.[143] In the case of a macroelectrode, however, the less effective linear diffusion is dominant and $r \gg d$.

In an electrochemical measurement, the noise is proportional to the active area of the electrode whereas the signal is dependent on the size of the diffusional field.[144] Thus it is easily appreciated that microelectrodes improve the signal to noise ratio since they have small electrode areas and strong diffusional fields relative to the size of the electrode surface. This improvement enables microelectrodes to have a lower detection limit than macroelectrode.[145] Furthermore, a smaller electrode area generates smaller currents and accordingly, less solution resistance is encountered. This is another advantage over a macroelectrode and a simple two electrode system can then be employed when using a microelectrode.[110]

In terms of electrochemical measurements carried out with microelectrode in a gas sensor, chronoamperometry is highlighted as this measurement can simultaneously determine the concentration and diffusion coefficient of the solute gas, as described in Chapter 1. In chronoamperometric measurements, the potential is stepped from a voltage where no electron transfer takes place to a potential where the reaction is fully driven in a diffusional controlled way. At short times, the current response is dominated by Cottrellian behaviour on a planar disc-electrode, as described by equation (1.35). At long times, the current decays to zero for a macroelectrode whilst a steady state current is recorded for a microelectrode, as described by equation (1.50). A detailed discussion about chronoamperometric experiments appeared in Chapter 1. Among the several models proposed[146-149] to simulate the current – time transients, the Shoup and Szabo equation is the most frequently used equation to describe the chronoamperometric response over all timescales with a reported error of less than 0.5%.[148] Chapters 4, 5, and 6 employ this equation to simultaneously determine concentrations and diffusion coefficients of some electroactive species in different RTILs.

2.3.3 The Application of Porous Electrodes for Gas Sensing

As the concerns over environmental pollution increase, new sensing techniques need to be introduced to replace the presently employed methods especially for toxic gases such as NO_x, H_2S and CO. These toxic gases survive in the air for relatively long times and the threshold levels of these gases are rather low in many countries (from ppb to ppm levels).[150,151] Due to the low detection limit needed, a variety of sensing techniques require a long preliminary adsorption or an absorption step which makes continuous or 'on the spot' measurements unsuitable.[151] Porous electrodes have a great potential to overcome these problems due to their extremely large active surface areas which lead to enhanced current responses. Porous electrodes have been studied for the detection of CO,[152] hydrocarbons,[152] NO_x[150] and H_2S,[151] and the reported detection limit can be as low as 0.07 ppb (ca. 0.1 $n\text{g}\cdot\text{L}^{-1}$).[151]

On the other hand, gas sensors with low detection limits for non-toxic gases, such as O_2 and CO_2, also require further development. For measurements in oceanography, biology and medicine, O_2 or CO_2 concentration can be lower than a couple of μmol·L^{-1},[84,153] where even current amperometric sensors cannot reliably applied in such situations.

Porous electrodes have a great variety of structures. They can be made by electroplating in templating layers of spheres before the latter are moved (see Chapter 7),[154] or from materials with pre-existing internal pores. Examples of the latter include vitreous carbon foam and graphite felt (see Chapter 3). They can also be made by metal oxide nanoparticles supported on conducting materials.[152,155]

The internal pore size of porous electrode can be varied from nanometres to millimetres. Thus from an electrochemical perspective, it is important to understand the mass transport take place in the pores. Chapter 7 specifically discusses this property for porous electrodes, and most notably the transition between simple Fickian diffusion to thin-layer behaviour. A theoretical model is proposed to simulate the current response generated from internal pores under diffusion conditions and a comparison between experiments and theoretical modelling can also be found in Chapter 7.

Apart from the application in chemical sensors,[156-162] porous electrodes are also receiving growing interests in fuel cells,[157] batteries,[157] catalysis,[155,163] and optical devices[164] due to their extremely high surface area and porous structure which allows fast transport of gases and liquids. Herein, we focus on their application in gas sensors as this is the primary interest of this thesis.

2.4 Aims of this Thesis

The work reported in this thesis aims to investigate the applicability of RTILs to be employed as electrolytes in amperometric gas sensors. It is anticipated that RTILs can minimise issues generated by the presently used electrolyte in amperometric gas sensors such as solvent loss, and the limitation of narrow electrochemical windows. Further, since porous electrodes may offer the advantage of extremely low detection limit, a theoretical model regarding the mass transport behaviour at porous electrodes is proposed and two different types of porous materials are also tested to examine the validity of the theory.

References

(1) Stetter, J. R.; Li, J. *Chem. Rev.* **2008**, *108*, 352.

(2) Xiong, L.; Compton, R. G. *Int. J. Electrochem. Sci.* **2014**, *9*, 7152.

(3) Gutmacher, D.; Foelmli, C.; Vollenweider, W.; Hoefer, U.; Woellenstein, J. *Procedia Eng.* **2011**, *25*, 1121.

(4) Srivastava, S. C.; Jaiswal, R. J.; Sinha, S.; Singh, R. V. K.; Das, R. N. *J. Mines, Met. Fuels* **1987**, *35*, 384.

(5) Sinha, A. K.; Rajwar, D. P.; Ghosh, A. K. *J. Mines, Met. Fuels* **1987**, *35*, 365.

(6) Rees, N. V.; Compton, R. G. *Energy & Environmental Science* **2011**, *4*.

(7) Korotcenkov, G.; Han, S. D.; Stetter, J. R. *Chem. Rev.* **2009**, *109*, 1402.

(8) Rahman, M. A.; Kumar, P.; Park, D.-S.; Shim, Y.-B. *Sensors* **2008**, *8*, 118.

(9) Knake, R.; Jacquinot, P.; Hodgson, A. W. E.; Hauser, P. C. *Analytica Chimica Acta* **2005**, *549*, 1.

(10) Arasaradnam, R. P.; Covington, J. A.; Harmston, C.; Nwokolo, C. U. *Aliment. Pharmacol. Ther.* **2014**, *39*, 780.

(11) Buszewski, B.; Grzywinski, D.; Ligor, T.; Stacewicz, T.; Bielecki, Z.; Wojtas, J. *Bioanalysis* **2013**, *5*, 2287.

(12) Biniecka, M.; Caroli, S. *TRAC-Trend Anal. Chem.* **2011**, *30*, 1756.

(13) Angerosa, F. *Eur. J. Lipid. Sci. Tech.* **2002**, *104*, 639.

(14) Dorresteijn, R. C.; De Gooijer, C. D.; Tramper, J.; Beuvery, E. C. *BIotichnol. Bioeng.* **1994**, *43*, 149.

(15) Wolfbeis, O. *Anal. Chem.* **2002**, *74*, 2663.

(16) Lu, X.; Winnik, M. *Chem. Mater.* **2001**, *13*, 3449.

(17) Demas, J. N.; DeGraff, B. A.; Coleman, P. B. *Anal. Chem.* **1999**, *74*, 793A.

(18) Chu, C.-S.; Lo, Y.-L.; Sung, T.-W. *Photonic Sensors* **2011**, *1*, 234.

(19) Yamazoe, N. *Sensors and Actuators B: Chemical* **2005**, *108*, 2.

(20) Barnes, S.; Old, L. T. *Chem. Eng. Prog.* **2009**, *105*, 51.

(21) Suresh, M.; Vasa, N. J.; Agarwal, V.; Chandapillai, J. *Sens. Actuators, B* **2014**, *195*, 44.

(22) Hori, H.; Ishimatsu, S.; Fueta, Y.; Hinoue, M.; Ishidao, T. *J. UOEH* **2013**, *34*, 363.

(23) Yin, C.; Liu, S.; Li, Y.; Chen, X. *Appl. Mech. Mater.* **2013**, *336-338*, 244.

(24) Chiorino, A.; Ghiotti, G.; Prinetto, F.; Carotta, M. C.; Gnani, D.; Martinelli, G. *Sens. Actuators, B* **1999**, *58*, 338.

(25) Golinelli, E.; Musazzi, S.; Perini, U.; Barberis, F. *Lect. Notes Elec. Eng* **2014**, *268*, 19.

(26) Dong, L.; Ma, W.; Zhang, L.; Yin, W.; Jia, S. *Guangxue Xuebao* **2014**, *34*, 0130002.

(27) Qiao, J.-P.; Qin, J.-M.; Yan, X.-Y.; Zhang, Z.-X. *J. Optoelectron. Laser* **2014**, *25*, 217.

(28) Kitiyanan, B.; Alvarez, W. E.; Harwell, J. H.; Resasco, D. E. *Chem. Phys. Lett.* **2000**, *317*, 497.

(29) Zhu, Q.; Aller, R. C. *Mar. Chem.* **2013**, *157*, 49.

(30) Jackson, R.; Oda, R. P.; Bhandari, R. K.; Mahon, S. B.; Brenner, M.; Rockwood, G. A.; Logue, B. A. *Anal. Chem.* **2014**, *86*, 1845.

(31) Zakrzewska, K. *Thin Solid Films* **2001**, *391*, 229.

(32) Vijayalakshmi, K.; Renitta, A.; Karthick, K. *Ceram. Int.* **2014**, *40*, 6171.

(33) Patil, J. Y.; Nadargi, D. Y.; Gurav, J. L.; Mulla, I. S.; Suryavanshi, S. S. *Mater. Lett.* **2014**, *124*, 144.

(34) Qi, Q.; Wang, P.-P.; Zhao, J.; Feng, L.-L.; Zhou, L.-J.; Xuan, R.-F.; Liu, Y.-P.; Li, G.-D. *Sens. Actuators, B* **2014**, *194*, 440.

(35) Kaci, S.; Keffous, A.; Hakoum, S.; Trari, M.; Mansri, O.; Menari, H. *Appl. Surf. Sci.* **2014**, *305*, 740.

(36) Carotta, M. C.; Fioravanti, A.; Gherardi, S.; Malagu, C.; Sacerdoti, M.; Ghiotti, G.; Morandi, S. *Sens. Actuators, B* **2014**, *194*, 195.

(37) Gu, J.; Zhang, Y.; Jiang, J.; Li, S. *Chin. J. Sci. Inst.* **2014**, *35*, 350.

(38) Darmastuti, Z.; Bur, C.; Moller, P.; Rahlin, R.; Lindqvist, N.; Andersson, M.; Schutze, A.; Spetz, A. L. *Sens. Actuators, B* **2014**, *194*, 511.

(39) Somov, A.; Baranov, A.; Spirjakin, D. *Sens. Actuators, A* **2014**, *210*, 157.

(40) Karpova, E.; Mironov, S.; Suchkov, A.; Karelin, A.; Karpov, E. E. *Sens. Actuators, B* **2014**, *197*, 358.

(41) Xiong, L.; Batchelor-McAuley, C.; Goncalves, L. M.; Rodrigues, J. A.; Compton, R. G. *Biosens. Bioelectron.* **2011**, *26*, 4198.

(42) Husson-Borg, P.; Majer, V.; Costa Gomes, M. F. *J. Chem. Eng. Data* **2003**, *48*, 480.

(43) Evans, R. G.; Klymenko, O. V.; Saddoughi, S. A.; Hardacre, C.; Compton, R. G. *J. Phys. Chem. B* **2004**, *108*, 7878.

(44) Chen, W.-C.; Hsu, Y.-L.; Venkatesan, S.; Zen, J.-M. *Electroanalysis* **2014**, *26*, 565.

(45) Lawrence, N. S.; Davis, J.; Marken, F.; Jiang, L.; Jones, T. G. J.; Davies, S. N.; Compton, R. G. *Sens. Actuators, B* **2000**, *69*, 189.

(46) Lawrence, N. S.; Jiang, L.; Jones, T. G. J.; Compton, R. G. *Anal. Chem.* **2003**, *75*, 2499.

(47) Sekhar, P. K.; Subramaniyam, K. *ECS Electrochem. Lett.* **2014**, *3*, B1.

(48) Bakker, E.; Telting-Diaz, M. *Anal. Chem.* **2002**, *74*, 2781.

(49) Maj-Zurawska, M.; Hulanicki, A. *Chem. Anal.* **2009**, *54*, 1149.

(50) Xie, X.; Bakker, E. *Anal. Chem.* **2013**, *85*, 1332.

(51) Severinghaus, J. W.; Bradley, A. F. *J. Appl. Physiol.* **1958**, *13*, 515.

(52) Caflisch, C. R.; Carter, N. W. *Anal. Biochem.* **1974**, *60*, 252.

(53) Beyenal, H.; Davis, C. C.; Lewandowski, Z. *Sens. Actuators, B* **2004**, *97*, 202.

(54) Mowery, M. D.; Hutchins, R. S.; Molina, P.; Alajarin, M.; Vidal, A.; Bachas, L. G. *Anal. Chem.* **1999**, *71*, 201.

(55) Ben Youssef, I.; Alem, H.; Sarry, F.; Elmazria, O.; Jimenez Rioboo, R.; Arnal-Herault, C.; Jonquieres, A. *Sens. Actuators, B* **2013**, *185*, 309.

(56) Fraticelli, Y. M.; Meyerhoff, M. E. *Anal. Chem.* **1981**, *53*, 992.

(57) Meyerhoff, M. E.; Fraticelli, Y. M.; Greenberg, J. A.; Rosen, J.; Parks, S. J.; Opdycke, W. N. *Clin. Chem.* **1982**, *28*, 1973.

(58) Arnold, M. A. *Anal. Chim. Acta* **1983**, *154*, 33.

(59) Wohltjen H.; Barger W.R.; Snow A.W.; N.L., J. *IEEE Trans. Electron. Dev.* **1985**, *ED-32*, 1170.

(60) Korotcenkov, G. *Mater. Sci. Eng. B* **2007**, *139*, 1.

(61) Korotcenkov, G. *Chemical Sensors: Fundamentals of Sensing Materials* Momentum Press, 2010; Vol. Volume 1: General Approaches.

(62) Clark, L. C., Jr.; Wold, R.; Granger, D.; Taylor, Z. *J. Appl. Physiol. (1948-1976)* **1953**, *6*, 189.

(63) Stetter, J. R. *Ann. Am. Conf. GoV. Ind. Hyg.* **1984**, *11*, 225.

(64) Bryzek, J. S.; Roundy, S.; Bircumshaw, B.; Chung, C.; Castellano, K.; Vestel, M.; Stetter, J. R. *IEEE Circuits Devices* **2006**, *22*, 8.

(65) Cao, Z.; Butner, W. J.; Stetter, J. R. *Electroanalysis* **1992**, *4*, 253.

(66) Chang, S. C.; Stetter, J. R.; Cha, C. S. *Talanta* **1993**, *40*, 461.

(67) Stetter, J. R.; Penrose, W. R. *Understanding Chemical Sensors and Chemical Sensor Arrays (Electronic Noses): Past, Present, and Future*; Wiley-VCH: Weinheim, Germany, 2002; Vol. 10.

(68) Stetter, J. R. In *NIST Workshop on Gas Sensors: Strategies for Future Technologies* Gaithersburg, MD, 1993.

(69) Findlay, M. W.; Penrose, W. R.; Stetter, J. R. *Anal. Chim. Acta* **1993**, *284*, 1.

(70) Stetter, J. R. *Ann. Am. Conf. GoV. Ind. Hyg.* **1984**, *11*, 225.

(71) Chiou, C.-Y.; Chou, T.-C. *Sens. Actuators, B* **2002**, *87*, 1.

(72) Kaisheva, A.; Iliev, I.; Christov, S.; Kazareva, R. *Sens. Actuators, B* **1997**, *44*, 571.

(73) Reinhardt, G.; Mayer, R.; Rosch, M. *Solid State Ionics* **2002**, *150*, 79.

(74) Nakamura, T.; Sakamoto, Y.; Saji, K.; Sakata, J. *Sens. Actuators, B* **2003**, *93*, 214.

(75) Ivers-Tiffee, E.; Hardtl, K. H.; Menesklou, W.; Riegel, J. *Electrochim. Acta* **2001**, *47*, 807.

(76) Ueda, T.; Plashnitsa, V. V.; Nakatou, M.; Miura, N. *Electrochem. Commun.* **2007**, *9*, 197.

(77) Knake, R.; Jacquinot, P.; Hauser, P. C. *Electroanalysis* **2001**, *13*, 631.

(78) Ernst, S.; Herber, R.; Slavcheva, E.; Vogel, I.; Baltruschat, H. *Electroanalysis* **2001**, *13*, 1191.

(79) Wang, J. *Counterterrorist etection Techniques of Explosivs*; Elsevier: Amsterdam, The Netherlands, 2007.

(80) Wang, J. *Electroanalysis* **2007**, *4*, 415.

(81) Wang, J.; Pumera, M.; Collins, G. E.; Mulchandani, A. *Anal. Chem.* **2002**, *74*, 6121.

(82) Wang, J.; Pumera, M.; Chatrathi, M. P.; Escarpa, A.; Musameh, M.; Collins, G.; Mulchandani, A.; Lin, Y.; Olsen, K. *Anal. Chem.* **2002**, *74*, 1187.

(83) Burke, D. G.; Halpern, B.; Malegan, D.; McCairns, E.; Danks, D.; Schlesinger, P.; Wilken, B. *Clin. Chem.* **1983**, *29*, 1834.

(84) Wang, Y.; Xu, H.; Zhang, J.; Li, G. *Sensors* **2008**, *8*, 2043.

(85) Cussler, E. L. *Diffusion: Mass Transfer in Fluid Systems*; Cambridge University Press: Cambridge, United Kingdom, 1997.

(86) Evans, N. T. S.; Quinton, T. H. *Respir. Physiol.* **1978**, *35*, 89.

(87) Haug, A. T.; White, R. E. *J. Electrochem. Soc.* **2000**, *147*, 980.

(88) Hahn, C. E. W. *Analyst* **1998**, *123*, 57R.

(89) Xiong, L., PhD Thesis: Amperomectric Gas Sensing, University of Oxford, 2014.

(90) Tierney, M. J.; Kim, H. O. L. *Anal. Chem.* **1993**, *65*, 3435.

(91) Do, J.-S.; Shieh, R.-Y. *Sens. Actuators, B* **1996**, *37*, 19.

(92) Do, J. S.; Chang, W. B. *Sens. Actuators, B* **2001**, *72*, 101.

(93) Moseley, P.; Norris, J.; Williams, D. *Techniques and mechanisms in gas sensing*; Adam Hilger, 1991.

(94) O'Mahony, A. M.; Compton, R. G. *Electroanalysis* **2010**, *22*, 2313.

(95) Koschel, D.; Coxam, J.-Y.; Majer, V. *Ind. Eng. Chem. Res.* **2007**, *46*, 1421.

(96) Silvester, D. S.; Compton, R. G. *Z. Phys. Chem.* **2006**, *220*, 1247.

(97) AlphaSense *AlphaSense Application Note ANN 106*; http://www.alphasense.com/.

(98) Najdeker, E.; Bishop, E. *J. Electroanal. Chem. Interfacial Electrochem.* **1973**, *41*, 79.

(99) Ramasubramanian, N. *J. Electroanal. Chem. Interfacial Electrochem.* **1975**, *64*, 21.

(100) Venkatasetty, H. V.; H.V. Setty Enterprises, Inc., USA . 1998, p 22 pp.

(101) *RAE Systems Inc Technical Note TN-152*; http://www.raesystems.eu/downloads/tech-notes.

(102) Schroder, U.; Wadhawan, J. D.; Compton, R. G.; Marken, F.; Suarez, P. A. Z.; Consorti, C. S.; de Souza, R. F.; Dupont, J. *New J. Chem.* **2000**, *24*, 1009.

(103) Stepnowski, P.; Muller, A.; Behrend, P.; Ranke, J.; Hoffmann, J.; Jastorff, B. *J. Chromatogr., A* **2003**, *993*, 173.

(104) Stepnowski, P.; Nichthauser, J.; Mrozik, W.; Buszewski, B. *Anal. Bioanal. Chem.* **2006**, *385*, 1483.

(105) Le Rouzo, G.; Lamouroux, C.; Bresson, C.; Guichard, A.; Moisy, P.; Moutiers, G. *J. Chromatogr. A* **2007**, *1164*, 139.

(106) Kim, K.-S.; Choi, S.; Demberelnyamba, D.; Lee, H.; Oh, J.; Lee, B.-B.; Mun, S.-J. *Chem. Commun.* **2004**, *10*, 828.

(107) Forsyth, S.; Golding, J.; MacFarlane, D. R.; Forsyth, M. *Electrochim. Acta* **2001**, *46*, 1753.

(108) Matsumoto, H.; Kageyama, H.; Miyazaki, Y. *Chem. Lett.* **2001**, 182.

(109) Wilkes, J. S.; Levisky, J. A.; Wilson, R. A.; Hussey, C. L. *Inorg. Chem.* **1982**, *21*, 1263.

(110) Bard, A. J.; Faulkner, L. R. *Electrochemical Methods: Fundamentals and Applications*; 2nd ed.; Wiley, 2000.

(111) Buzzeo, M. C.; Evans, R. G.; Compton, R. G. *ChemPhysChem* **2004**, *5*, 1106.

(112) Barrosse-Antle, L. E.; Bond, A. M.; Compton, R. G.; O'Mahony, A. M.; Rogers, E. I.; Silvester, D. S. *Chem. - Asian J.* **2010**, *5*, 202.

(113) Tian, Y.-H.; Goff, G. S.; Runde, W. H.; Batista, E. R. *J. Phys. Chem. B* **2012**, *116*, 11943.

(114) O'Mahony, A. M.; Silvester, D. S.; Aldous, L.; Hardacre, C.; Compton, R. G. *J. Chem. Eng. Data* **2008**, *53*, 2884.

(115) Buzzeo, M. C.; Hardacre, C.; Compton, R. G. *Anal. Chem.* **2004**, *76*, 4583.

(116) Ning, H.; Hou, M. Q.; Mei, Q. Q.; Liu, Y. H.; Yang, D. Z.; Han, B. X. *Sci. China: Chem.* **2012**, *55*, 1509.

(117) Vranes, M.; Dozic, S.; Djeric, V.; Gadzuric, S. *J. Chem. Eng. Data* **2012**, *57*, 1072.

(118) Hunger, J.; Stoppa, A.; Schroedle, S.; Hefter, G.; Buchner, R. *ChemPhysChem* **2009**, *10*, 723.

(119) Li, J.-G.; Hu, Y.-F.; Ling, S.; Zhang, J.-Z. *J. Chem. Eng. Data* **2011**, *56*, 3068.

(120) Zech, O.; Stoppa, A.; Buchner, R.; Kunz, W. *J. Chem. Eng. Data* **2010**, *55*, 1774.

(121) Sun, J.; Forsyth, M.; MacFarlane, D. R. *J. Phys. Chem. B* **1998**, *102*, 8858.

(122) Lide, D. *CRC Handbook of Chemistry and Physics*; 85 ed.; Taylor & Francis, 2004.

(123) Miran, M. S.; Kinoshita, H.; Yasuda, T.; Susan, M. A. B. H.; Watanabe, M. *Chem. Commun.* **2011**, *47*, 12676.

(124) Chaban, V. V.; Voroshylova, I. V.; Kalugin, O. N.; Prezhdo, O. V. *J. Phys. Chem. B* **2012**, *116*, 7719.

(125) Fitchett, B. D.; Knepp, T. N.; Conboy, J. C. *J. Electrochem. Soc.* **2004**, *151*, E219.

(126) Bester-Rogac, M.; Hunger, J.; Stoppa, A.; Buchner, R. *J. Chem. Eng. Data* **2010**, *55*, 1799.

(127) Tunnell, G. *World distribution of atmospheric water vapour pressure*; H.M. Stationery Office: United Kingdom, 1958.

(128) Ambrose, D.; Sprake, C. H. S. *The Journal of Chemical Thermodynamics* **1970**, *2*, 631.

(129) Ewing, M. B.; Ochoa, J. C. S. *J. Chem. Eng. Data* **2004**, *49*, 486.

(130) Wilkes, J. S. *J. Mol. Catal. A* **2004**, *214*, 11.

(131) Huddleston, J. G.; Visser, A. E.; Reichert, W. M.; Willauer, H. D.; Broker, G. A.; Rogers, R. D. *Green Chem.* **2001**, *3*, 156.

(132) Chan, B. K. M.; Chang, N.; Grimmett, M. R. *Australian J. Chem.* **1977**, *9*, 2005.

(133) Dessiaterik, Y.; Baer, T.; Miller, R. E. *J. Phys. Chem. A* **2006**, *110*, 1500.

(134) Chowdhury, A.; Thynell, S. T. *Thermochim. Acta* **2006**, *443*, 159.

(135) Fredlake, C. P.; Crosthwaite, J. M.; Hert, D. G.; Aki, S. N. V. K.; Brennecke, J. F. *J. Chem. Eng. Data* **2004**, *49*, 954.

(136) Ngo, H. L.; LeCompte, K.; Hargens, L.; McEwen, A. B. *Thermochim. Acta* **2000**, *357-358*, 97.

(137) Wang, C.; Guo, Y.; Zhu, X.; Cui, G.; Li, H.; Dai, S. *Chem. Commun.* **2012**, *48*, 6526.

(138) Cui, G.; Lin, W.; Ding, F.; Luo, X.; He, X.; Li, H.; Wang, C. *Green Chem.* **2014**, *16*, 1211.

(139) Cui, G.; Zheng, J.; Luo, X.; Lin, W.; Ding, F.; Li, H.; Wang, C. *Angew. Chem., Int. Ed.* **2013**, *52*, 10620.

(140) Wang, C.-M.; Cui, G.-K.; Luo, X.-Y.; Xu, Y.-J.; Li, H.-R.; Dai, S. *J. Am. Chem. Soc.* **2011**, *133*, 11916.

(141) Fox, E. T.; Paillard, E.; Borodin, O.; Henderson, W. A. *J. Phys. Chem. C* **2013**, *117*, 78.

(142) Rogers, E. I.; O'Mahony, A. M.; Aldous, L.; Compton, R. G. *ECS Trans.* **2010**, *33*, 473.

(143) Cope, D. K.; Tallman, D. E. *J. Electroanal. Chem. Interfacial Electrochem.* **1985**, *188*, 21.

(144) Weber, S. G. *Anal. Chem.* **1989**, *61*, 295.

(145) Wang, J. *Analytical Electrochemistry*; 3rd ed.; Wiley, 2006.

(146) Fleischmann, M.; Pons, S. *J. Electroanal. Chem. Interfacial Electrochem.* **1988**, *250*, 257.

(147) Klymenko, O. V.; Evans, R. G.; Hardacre, C.; Svir, I. B.; Compton, R. G. *J. Electroanal. Chem.* **2004**, *571*, 211.

(148) Shoup, D.; Szabo, A. *J. Electroanal. Chem. Interfacial Electrochem.* **1982**, *140*, 237.

(149) Heinze, J. *J. Electroanal. Chem. Interfacial Electrochem.* **1981**, *124*, 73.

(150) Zeng, J.; Hu, M.; Wang, W.; Chen, H.; Qin, Y. *Sens. Actuators, B* **2012**, *161*, 447.

(151) Schiavon, G.; Zotti, G. *Anal. Chem.* **1995**, *67*, 318.

(152) Wu, N.; Zhao, M.; Zheng, J.-G.; Jiang, C.; Myers, B.; Li, S.; Chyu, M.; Mao, S. X. *Nanotechnology* **2005**, *16*, 2878.

(153) Revsbech, N. P.; Larsen, L. H.; Gundersen, J.; Dalsgaard, T.; Ulloa, O.; Thamdrup, B. *Limnology and Oceanography: Methods* **2009**, *7*, 371.

(154) Barnes, E. O.; Chen, X.; Li, P.; Compton, R. G. *J. Electroanal. Chem.* **2014**, *720-721*, 92.

(155) Sun, F.; Cai, W.; Li, Y.; Jia, L.; Lu, F. *Adv. Mater.* **2005**, *17*, 2872.

(156) Wang, R.; Okajima, T.; Kitamura, F.; Ohsaka, T. *Electroanalysis* **2004**, *16*, 66.

(157) Shin, H.-C.; Dong, J.; Liu, M. *Adv. Mater.* **2003**, *15*, 1610.

(158) Shimizu, Y.; Hyodo, T.; Egashira, M. *Catal. Surv. Asia* **2004**, *8*, 127.

(159) Lee, Y. J.; Braun, P. V. *Adv. Mater.* **2003**, *15*, 563.

(160) Nakayama, D.; Takeoka, Y.; Watanabe, M.; Kataoka, K. *Angew.Chem. Int. Ed.* **2003**, *42*, 4197.

(161) R. W. J. Scott; S. M. Yang; N. Coombs; G. A. Ozin; D. E. Williams *Adv. Funct. Mater.* **2003**, *13*.

(162) Song, Y. Y.; Zhang, D.; Gao, W.; Xia, X. H. *Chem. Eur. J.* **2005**, *11*, 2177.

(163) Matsushita, S. I.; Miwa, T.; Tryk, D. A.; Fujishima, A. *Langmuir* **1998**, *14*, 6441.

(164) Jiang, P.; Mcfarland, M. J. *J. Am. Chem. Soc.* **2005**, *127*, 3710.

Chapter 3

Experimental methods

This chapter describes all the chemical reagents and room temperature ionic liquids (RTILs) used throughout this thesis, as well as the general experimental methodology, electrochemical T-cell set ups and other apparatus. Details of experimental procedures and apparatus specific to individual investigations will be given in the relevant chapters.

3.1 Chemicals

The names and abbreviations of chemicals used in the experiments in the following chapters are listed in **Table 3.1**.

Table 3.1: List of chemicals used in this thesis

Chemical name	**Formula/Abbreviation**	**Purity**	**Supplier**
1-butyl-3-methylimidazolium acetate	$[C_4mim][Ac]$	-	QUILL, Belfast
1-butyl-3-methylimidazolium tetrafluoroborate	$[C_4mim][BF_4]$	-	QUILL, Belfast
1-butyl-3-methylimidazolium tris(pentafluoroethyl)-trifluorophosphate	$[C_4mim][FAP]$	-	QUILL, Belfast
1-butyl-3-methylimidazolium bis(trifluoromethanesulfonyl)	$[C_4mim][NTf_2]$	-	QUILL, Belfast

imide			
1-ethyl-3-methylimidazolium acetate	[C$_2$mim][Ac]	-	QUILL, Belfast
trihexyl(tetradecyl)phosphonium trifluorotris(pentafluoro-ethyl)phosphate	[P$_{6,6,6,14}$][FAP]	-	QUILL, Belfast
N-butyl-*N*-methylpyrrolidinium bis(trifluoromethanesulfonyl) imide	[Pyrr$_{14}$][NTf$_2$]	-	QUILL, Belfast
N-butyl-*N*-methylpiperidinium bis(trifluoromethanesulfonyl) imide	[Pip$_{14}$][NTf$_2$]	-	QUILL, Belfast
N-butyl-*N*-methylazepinium bis(trifluoromethanesulfonyl) imide	[Aze$_{14}$][NTf$_2$]	-	QUILL, Belfast
N-methyl-*N*-(2-methoxyethyl)pyrrolidinium bis(trifluoromethanesulfonyl) imide	[Pyrr$_{1(2o1)}$][NTf$_2$]	-	QUILL, Belfast
N-methyl-*N*-(2-methoxyethyl)piperidinium bis(trifluoromethanesulfonyl) imide	[Pip$_{1(2o1)}$][NTf$_2$]	-	QUILL, Belfast
ferrocene	Fe(C$_5$H$_5$)$_2$/Fc	98%	Sigma-Aldrich
decamethylferrocene	Fe(C$_{10}$H$_{15}$)$_2$/DmFc	95%	Fluka
tetrabutylammonium perchlorate	TBAP	≥ 99%	Fluka
hexaammineruthenium(III) chloride	Ru(NH$_3$)$_6$Cl$_3$	98%	Sigma-Aldrich
potassium chloride	KCl	≥ 99%	Sigma-Aldrich

acetonitrile	MeCN	≥ 99.9%	Sigma-Aldrich
deionised water	H_2O	18.2 MΩ·cm	Millipore
ethanol	EtOH	≥ 99.8%	Sigma-Aldrich
nitrogen, compressed	N_2	industrial	BOC
oxygen, compressed	O_2	industrial	BOC
carbon dioxide, compressed	CO_2	industrial	BOC

All the RTILs used in the following investigation were synthesised by Dr. Peter Goodrich and kindly donated by Prof. Christopher Hardacre at The Queen's University Ionic Liquids Laboratory ('QUILL'), Belfast. All hydrophobic non-functionalised [NTf$_2$] anion-based ILs were prepared via alkylation[1] of the *N*-methylpyrrolidine, *N*-(2-methoxyethyl)pyrrolidine, *N*-methylpiperidine or *N*-butylazepane with the corresponding alkylhalide. This formed a cyclic alkylammonium halide which underwent an aqueous metathesis reaction with Li[NTf$_2$] to form the corresponding cyclic alkylammonium [NTf$_2$] anion-based RTILs. The hydrophillic [BF$_4$] and [Ac] anion-based RTILs were synthesised via the alkylation of *N*-methylimidazole with bromobutane[2] to yield 1-methy-3-butylimidazolium bromide [C$_4$mim]Br. This salt was dissolved in water and passed through a Br^-/OH^- anion exchange resin, Amberlite 400. The [C$_4$mim][OH] was then neutralised with an equimolar amount of tetrafluoroboric acid or acetic acid to form the desired RTILs. All the RTILs were used as received without further purification.

All the aqueous solutions used in the thesis were prepared using deionised water which has a resistivity equal to or greater than 18.2 MΩ·cm at 298 K from a

Millipore water system. RTIL solutions containing decamethylferrocene were prepared by adding 30 μL of approximately 2 mM decamethylferrocene in acetonitrile to 30 μL of the RTILs, followed by the removal of the acetonitrile under vacuum overnight. All the gases introduced to the RTIL solutions, unless specified in Chapter 7, were passed through a column of $CaCl_2$/4 Å molecular sieves (Acros Organics) before any contact with sample solutions in order to remove any residual water.

3.2 Instrumental

All electrochemical measurements were performed in a thermostatted box functioned as a Faraday cage[3] using a computer-controlled PGSTAT30-Autolab potentiostat (Eco-Chemie, Netherlands). All the experiments, except as reported in Chapter 7, were conducted using a three-electrode arrangement with a platinium (Pt) micro-disc working electrode (Model G0225, Princeton Applied Research, the United States) and two silver wires (99.99%, annealed, 0.5 mm diameter, Goodfellow, Cambridge) as the reference and counter electrode, respectively. The Pt micro-disc electrode was polished was polished with alumina powder (Buehler, IL) of 1.0, 0.3, and 0.05 μm sizes on three soft lapping polishing pads (Kemet Ltd., UK). The potential step chronoamperometry technique (detailed in Chapter 1) on the one-electron oxidation of 2.0 mM ferrocene in acetonitrile containing 0.1 M TBAP was employed to calibrate the radius of the Pt working electrode. The known diffusion coefficient[4] of 2.30×10^{-9} $m^2 \cdot s^{-1}$,at 298 K, was used to calculate the radius r_e using the equation:[5]

$$I_{ss} = 4nFr_eDC \tag{3.1}$$

where n is the number of electrons transferred, F is the Faraday constant. A steady state current I_{ss} is recorded. Thus r_e can be derived with the known C, D, n values.

All the electrochemical measurement involving RTILs were carried out in a specially designed T-cell which enables voltammetry to be conducted using tiny volumes of IL while also permitting both the drying of the solvent and the introduction of gases into the cell (see **Figure 3.1**).[3,6-8] The working electrode was sleeved with part of a disposable pipette tip to provide a conical cavity for the RTIL sample.[7] Prior to exposure to any gas, the T-cell system, containing 30 μL of RTIL, was put under vacuum overnight to remove any impurities (notably possible water and organic solvents).

For experiments using porous electrode in Chapter 7, the graphite felt was provided by the SGL group, Germany (www.sglgroup.com). Product specification is provided by the manufacturer: the nominal thickness was 2.2 mm and the porosity was 95%; the carbon fibre which made up of the graphite felt had a diameter of 8 μm with a density around 1.8 g·cm^{-3}.[9]

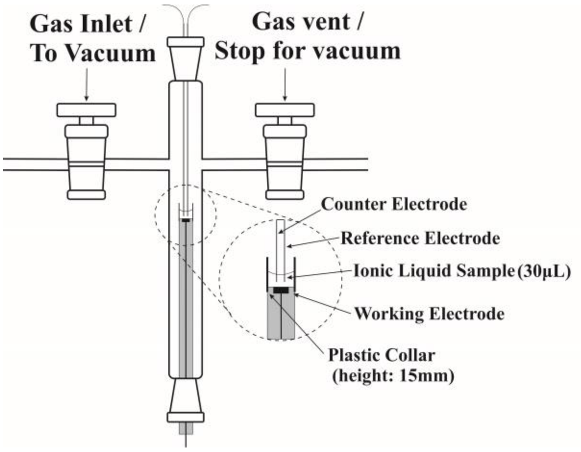

Figure 3.1: Schematic illustration of the T-cell used in the small scale study of RTILs.[7,8] The approximate dimension of the RTIL layer covering the electrode is 0.5 cm in diameter and 0.2 cm in height, and was measured by a calliper.

The graphite felt was then cut into 5.1 mm diameter discs using a punch. This disc electrode was held on a jig and cut into 1.1 mm thickness. A small thickness was desirable in order to reduce the permeation time for the solution of interest. The punch and jig were made by the Departmental workshop. A platinum wire (99.99%, annealed, 0.5 mm diameter, Goodfellow, Cambridge Ltd., UK) was passed through the felt like a 'fish hook' to secure the electrode and provide a good electrical connection between the electrode and the potentiostat (**Figure 3.2**). **Figure 3.3** is a photo taken from the graphite felt material used in this experiment. The graphite felt electrode was then immersed in the solution for electrochemical measurements. Note that the background current generated by the immersed Pt wire is tiny compared to the signal from the porous electrode, and thus provide a negligible influence on the experiment.

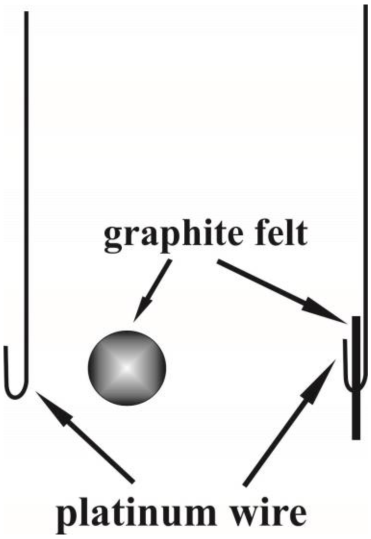

Figure 3.2: Schematic illustration of the graphite felt electrode and the platinum 'fish hook'.

Figure 3.3: The graphite felt material used in this thesis.

The vitreous carbon foam electrode used in Chapter 7 was purchased from Goodfellow, Cambridge Ltd., UK. The bulk foam is 3.2 mm in thickness. Pores occupy 96.5% of the volume with a 0.208 mm radius according to the product specification provided by Goodfellow.

The electrode is simply made by cutting a small piece from the bulk foam. A Pt wire contact was employed and had the same function as described above for the graphite felt electrode. The vitreous carbon foam electrode was then immersed in the solution of interest for electrochemical measurements. Note that the background current generated by Pt wire is also negligible in this case. **Figure 3.4** shows a photo taken from the foam material used in this thesis.

Figure 3.4: Vitreous carbon foam material used in the experiment.

References

(1) Bonhote, P.; Dias, A.-P.; Papageorgiou, N.; Kalyanasundaram, K.; Graetzel, M. *Inorg. Chem.* **1996**, *35*, 1168.

(2) Ferguson, J. L.; Holbrey, J. D.; Ng, S.; Plechkova, N. V.; Seddon, K. R.; Tomaszowska, A. A.; Wassell, D. F. *Pure Appl. Chem.* **2012**, *84*, 723.

(3) Evans, R. G.; Klymenko, O. V.; Saddoughi, S. A.; Hardacre, C.; Compton, R. G. *J. Phys. Chem. B* **2004**, *108*, 7878.

(4) Wang, Y.; Rogers, E. I.; Compton, R. G. *J. Electroanal. Chem.* **2010**, *648*, 15.

(5) Compton, R. G.; Banks, C. E. *Understanding Voltammetry*; 2nd Edition ed.; Imperial College Press, 2010.

(6) Huang, X.-J.; Rogers, E. I.; Hardacre, C.; Compton, R. G. *J. Phys. Chem. B* **2009**, *113*, 8953.

(7) Li, P.; Henstridge, M. C.; Xiong, L.; Compton, R. G. *Electroanalysis* **2013**, *25*, 2268.

(8) Barrosse-Antle, L. E.; Bond, A. M.; Compton, R. G.; O'Mahony, A. M.; Rogers, E. I.; Silvester, D. S. *Chem. - Asian J.* **2010**, *5*, 202.

(9) Delanghe, B.; Tellier, S.; Astruc, M. *Electrochim. Acta* **1990**, *35*, 1369.

Chapter 4

Rate and Extent of Carbon Dioxide Uptake in Room Temperature Ionic Liquids: a New Approach using Microdisc Electrode Voltammetry

This chapter introduces a simple method which enables the simultaneous determination of both the maximum CO_2 concentration and kinetics of CO_2 uptake and release by a room temperature ionic liquid. This method is based upon the analysis of chronoamperometry recorded in bulk ionic liquid at intervals during exposure to CO_2 and subsequent exposure to vacuum to remove the dissolved CO_2. Comparing experimental data with a numerical model reveals the rate-limiting factors for both uptake and release of CO_2. The work in this Chapter includes collaboration with Dr. Martin Henstridge (theoretical model) and Dr. Linhongjia Xiong (method validation in [C_4mim][BF_4]) and has been published in *Electroanalysis*.[1]

4.1 Introduction

The uptake, capture and storage of the greenhouse gas carbon dioxide are currently the subject of considerable urgent investigation prompted not least by concerns over climate change.[2-5] Whilst diverse approaches have been proposed, one of those with possible practical application concerns the absorption of carbon dioxide by room temperature ionic liquids (RTILs) where large solubilities can be realised. The merits of RTILs include their extremely low volatility which aids the processing of the dissolved carbon dioxide[6-9] and also their wide electrochemical windows which open up the possibility of electrochemical sequestration of carbon dioxide, and transformation into chemical feedstocks for fine chemical synthesis.[10-18]

In particular the use of imidazolium based RTILs has valuable potential because of the unusually high solubility of carbon dioxide in those media which likely arises from complexation between the solute gas and the constituent ion(s) of the RTILs as reported for 3-methylimidazolium acetate[19-21] (see **Figure 4.1** for the chemical structure):

$$CO_2 + A \rightleftharpoons CO_2{\cdot}A \qquad (4.1)$$

where A is a component of the ionic liquid. The complexation is most likely arisen from the nucleophilic reaction between the carbon atom on CO_2 and nitrogen atom on the imidazolium ring.[22-24] Thus the solubility of carbon dioxide in these solvents can be around the Molar (M) level with the number of solute molecules approaching that of the RTIL solvent itself!

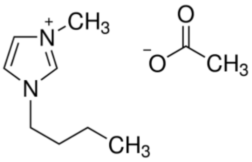

Figure 4.1: Chemical structure of 1-butyl-3-methylimidazolium acetate.

The unusually high values of carbon dioxide solubility in some RTILs pose a challenge in measurement. In particular the need for rapid but accurate monitoring of a large number of candidate RTILs for carbon dioxide capture challenges the classical gas solubility approaches – the gravimetric methods, especially isochoric saturation technique (IST) and microbalance (MB). IST measures the pressure above the solution when thermodynamic equilibrium is attained, and directly relates the pressure to the solubility of the gas in the liquid.[25] On the other hand, MB uses a electrobalance to measure the weight of the solution at thermodynamic equilibrium.[26] The solubilities measured using these methods are fully summarised in **Table 4.1** (the abbreviations for the RTILs in the table are explained in **Figures 4.2** and **4.3**). Although gravimetric methods have some advantages, for instance the measurement can be made at various pressures and temperatures, the process needs long equilibration time and a considerable amount of RTIL samples, as well as the high cost of the machine. In the present Chapter we show that a simple electrochemical method can provide the necessary data and allows not only the *uptake* of carbon dioxide to be found as a function of temperature but also the *dynamics* of gas uptake and release to be quantified.

Table 4.1: CO_2 solubility, S (mole fraction), at 1 bar and different temperatures.

IL	Temp / K	S / %	Method
$[C_4mim][BF_4]$[27]	313	1.4	IST[25,28]
$[C_4mim][Bu_2PO_4]$[27]	313	2.05	IST
$[C_4mim][FAP]$[25]	303	4	IST
$[C_4mim][OcSO_4]$[29]	313	1.55	IST
$[C_4mim][NTf_2]$[27]	313	2.3	IST
$[C_{10}mim][NTf_2]$[30]	303	3.23	IST
$[C_8H_4F_{13}mim][NTf_2]$[30]	298	3.9	IST
$[C_{10}mim][Me_2PO_4]$[27]	313	1	IST
$[C_2mim][BETI]$[31]	298	2.9	MB[32,33]
$[C_2mim][FAP]$[25]	303	3.35	IST
$[C_2mim][Et_2PO_4]$[27]	313	1.5	IST
$[C_2mim][EtSO_4]$[29]	283	1.6	IST
$[C_2mim][NTF_2]$[31]	298	3.1	MB
$[C_2mim][TFA]$[31]	298	2.25	MB
$[C_2mim][TFO]$[31]	298	1.96	MB
$[C_6mim][BF_4]$[31]	298	1.77	MB
$[C_6mim][FAP]$[25]	303	3.67	IST
$[C_6mim][NTF_2]$[31]	298	3.4	MB

[C$_8$mim][BF$_4$]^{31}	298	2.25	MB
[C$_8$mim][NTf$_2$]^{30}	298	3.3	IST

S* is the mole fraction of CO$_2$ in the solution: $S=\frac{n(CO2)}{n(CO2)+n(IL)}\times 100\%$

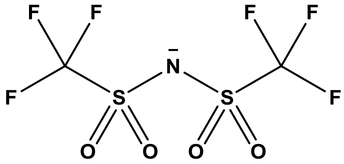

[NTf$_2$]$^-$: bis(trifluoromethanesulfonyl)imide

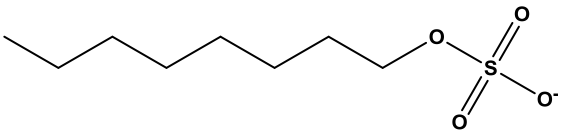

[OcSO$_4$]$^-$: octylsulfate

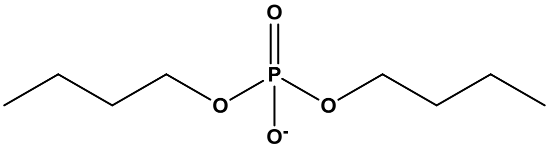

[Bu$_2$PO$_4$]$^-$: dibutyl-phosphate

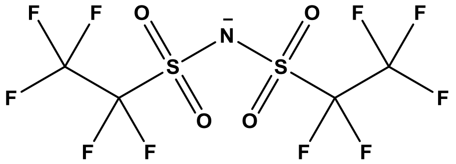

[BETI]$^-$: bis(pentafluoro-ethylsufonyl)imide

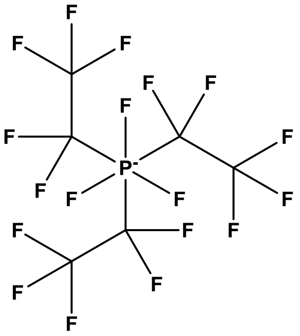

[FAP]$^-$: tris(pentafluoroethyl)-trifluorophosphate

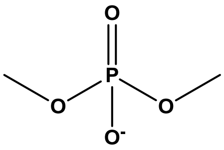

[Me$_2$PO$_4$]$^-$: dimethylphosphate

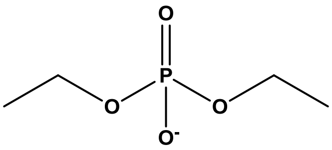

[Et$_2$PO$_4$]$^-$: diethylphosphate

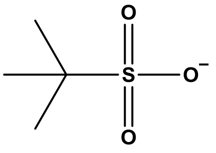

[TFO]$^-$: trifluoromethylsolfonate

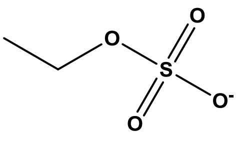

[EtSO$_4$]$^-$: ethylsulfate

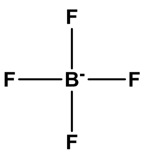

[BF$_4$]$^-$: tetrafluoroborate

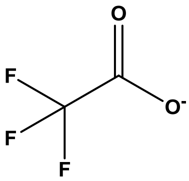

[TFA]$^-$: trifluoroacetate

Figure 4.2: RTIL anions names and abbreviations in **Table 4.1.**

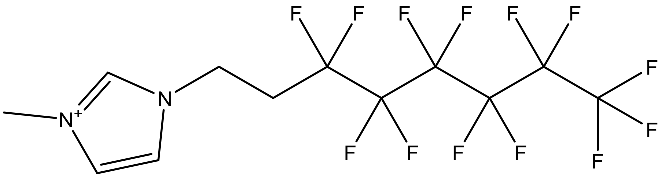

$[C_8H_4F_{13}mim]^+$: 1-(3,3,4,4,5,5,6,6,7,7,8,8,8-tridecafluorooctyl)-3-methylimidazolium

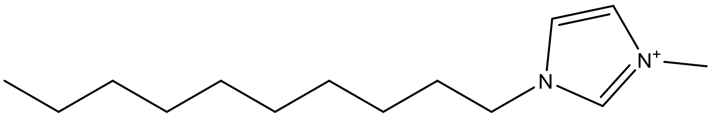

$[C_{10}mim]^+$: 1-decyl-3-methylimidazolium

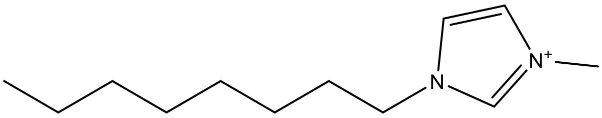

$[C_8mim]^+$: 1-octyl-3-methylimidazolium

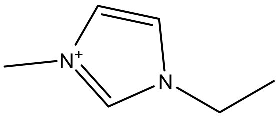

$[C_2mim]^+$: 1-ethyl-3-methylimidazolium

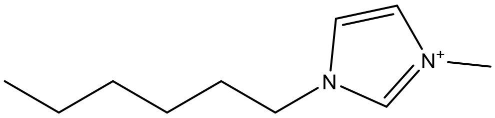

$[C_6mim]^+$: 1-hexyl-3-methylimidazolium

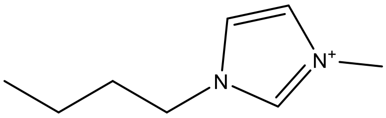

$[C_4mim]^+$: 1-butyl-3-methylimidazolium

Figure 4.3: RTIL cations names and abbreviations in **Table 4.1**.

4.2 Experimental

4.2.1 Set Up of The Electrochemical Cell

The experimental approach proposed is based on the T-cell shown in Chapter 3. The microelectrode is immersed in a tiny volume of the RTIL solution of interest: 30 μL of RTIL was mixed with 30 μL acetonitrile (MeCN) containing 2.0 mM decamethylferrocene (DmFc). The reason for choosing decamethylferrocene instead of ferrocene as internal reference is that ferrocenium can react with RTILs so interference of the voltammogram can potentially take place whereas decamethylferrocene is rather stable in RTILs.[34] Prior to exposure to CO_2, the whole system was vacuumed overnight to remove the acetonitrile. No precipitate can be found in the RTIL which means decamethylferrocene was dissolved completely in the RTIL. Note that as silver wire was employed as pseudo-reference electrode, the potential related to electrochemical reaction may shift during different experiments. Therefore, the oxidation of decamethylferrocene was used as an internal redox reference, by which help us better locate the electrochemical reaction under investigation.

4.2.2 Carbon Dioxide Measurements

During the CO_2 uptake experiments, compressed CO_2 are passed through a $CaCl_2$/4 Å molecular sieve Dreschel bottle before entering the T-cell in order to fully dry the gas. Two measurements are then made.

First a voltammogram is recorded when the RTIL has been allowed to uptake an appreciable amount of carbon dioxide (saturation of CO_2 is the confirmed when the reduction peak reaches maximum) and the peak potential for the electrochemical reduction of carbon dioxide observed; the latter is typically a one electron process leading first to the radical anion of carbon dioxide and subsequently to other products such as oxalate:[21,35]

$$\mathbf{CO_2 + e^- \rightarrow CO_2^{\cdot -} \rightarrow C_2O_4^{2-}, ...} \qquad (4.2)$$

Note that owing to the tiny size (~μm) of the microelectrodes used the concentration depletion local to the electrode is a tiny fraction of dissolved carbon dioxide so that the measurement is essentially non-perturbing to the concentration profile of the dissolved gas within the entire RTIL volume. The RTIL layer covering the electrode has a diameter and height around 0.5 and 0.2 cm, measured by a calliper, respectively, as illustrated in Chapter 3, **Figure 3.1**.

Second a fresh sample of RTIL, initially under vacuum, is exposed to carbon dioxide and potential step transients recorded periodically until the solvent becomes saturated with carbon dioxide. Once the solvent is saturated the carbon dioxide flow is stopped and the system is once more placed under vacuum. Periodic potential step transients continue to be recorded as the carbon dioxide is removed from the solvent.

The potential steps are measured from a potential at which zero current flows to one negative of the carbon dioxide reduction such that the electrolysis of the latter is transport controlled but not sufficiently negative that solvent reduction is induced.

The current time transient from the potential step is measured over a period of several seconds and analysed so as to give a measure of both the diffusion coefficient and dissolved carbon dioxide levels. Note first that the latter is measured local to the microelectrode surface and second that since the duration of the potential step transients is tiny in comparison to the overall time required for the RTIL to become saturated (several hours, *vide infra*) with gas that these are *effectively* instantaneous, non-perturbing, measurements of the local concentrations close to the electrode surface.

The analysis of these potential step transients is based upon the approximate analytical expression due to Shoup and Szabo,[36-38] which gives the current response *I* as a function of concentration C, diffusion coefficient D and electrode radius r for all times:

$$I = 4nFrDCf(t) \tag{4.3}$$

where n is the number of electrons transferred, F is the Faraday constant and $f(t)$ is given by:

$$f(t) = 0.7854 + 0.8862\sqrt{\frac{r^2}{4Dt}} + 0.2146\exp\left(-0.7823\sqrt{\frac{r^2}{4Dt}}\right) \tag{4.4}$$

According to equation (4.3) and (4.4), at short times, the response current I is a Cottrellian current which depends on $nCD^{1/2}t^{-1/2}$; at long times, a steady state current is recorded, and can be described as $I_{ss} = 4nFrDC$. By combining data from short and long times, C and D can be resolved. The experimental transient is compared with the Shoup-Szabo expression for a range of different values for both C and D and the combination which best fits the experiment is retained. The "best" fit was determined as that which minimised the mean scaled absolute deviation (MSAD), defined by:

$$MSAD = \frac{1}{N}\sum_{N}\frac{I_{\mathrm{fit}} - I_{\mathrm{exp}}}{I_{\mathrm{exp}}} \tag{4.5}$$

where N is the number of experimental data points and I_{exp} and I_{fit} denote the current from the experimental and Shoup-Szabo transients respectively.

The method was validated by Dr. Linhongjia Xiong[39] who applied it to the dissolution of O_2 in [C_4mim][BF_4], for which no complexation occurs and the limiting gas concentration is much lower than that observed for CO_2 in [C_4mim][Ac] and for which values for k_H (Henry's law constant) have been measured previously.[28,40] **Figure 4.4a** shows the chronoamperometric responses for 100%, 80%, 50% and 30% oxygen in [C_4mim][BF_4] recorded at 293 K at a 5.0 μm radius platinum micro-disc electrode. The limiting concentrations of dissolved oxygen were obtained via Shoup-Szabo analysis and the mole fraction of dissolved O_2 was then calculated for each transient and plotted against the partial pressure of O_2 gas. The resulting plot (shown in **Figure 4.4b**) was found to be linear and yielded a Henry's law constant of 1120 ± 70 bar. This value is consistent with other values reported in the literature using the microbalance technique,[28,40] thus validating the current method as a tool for studying gas solubility in RTILs.

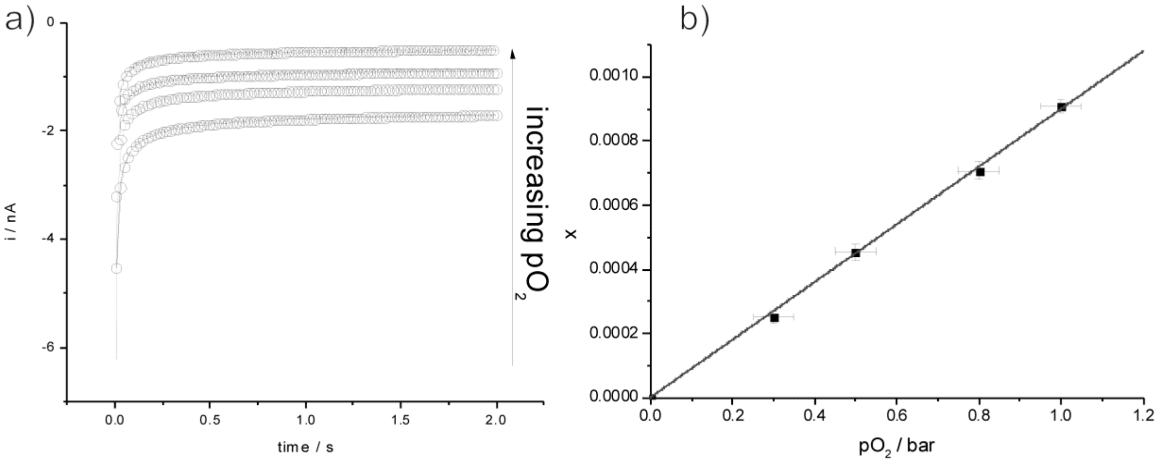

Figure 4.4: a) Chronoamperometry for 1, 0.8, 0.5 and 0.3 bar oxygen in [C_4mim][BF_4] at 293 K recorded at a 5.0 μm radius platinum micro-disc electrode. b) Plot of the measured mole fraction, x, against the imposed partial pressure, p for O_2.

4.3 Results and Discussion

Experiments using CO_2 were conducted using [C_4mim][Ac], [C_4mim][BF_4], [C_4mim][NTf_2], [C_4mim][FAP] and [C_2mim][Ac]. [C_4mim][Ac], as discussed in the text below, was chosen to perform chronoamperometric, uptake and release, temperature dependence and variable partial pressure study. Theoretical modelling was used to determine the mechanism and kinetics of the CO_2 – RTIL uptake process.

4.3.1 Theoretical Model

The theoretical model and programming were developed by Dr. Martin Henstirdge who completed his DPhil and Post-doctoral research in the group. The model was developed to analyse the concentration–time data for the uptake of CO_2 by [C_4mim][Ac] on the basis of a kinetic model in which CO_2 dissolves at the surface of the RTIL layer above the electrode and then is transported to the latter via Fickian diffusion with a diffusion coefficient, $D_{\mathrm{CO_2}}$. Further, since high carbon dioxide solubility is often closely linked to complex formation with the ionic liquid component, A, our model additionally includes a complexation reaction running in parallel with diffusive transport:

$$\mathrm{CO_2 + A \rightleftharpoons CO_2 \cdot A} \qquad (4.6)$$

where CO_2•A is the complex which has its own diffusion coefficient, $D_{\mathrm{CO_2 \cdot A}}$.

The Shoup-Szabo analysis revealed that the electroactive species has a small diffusion coefficient (~10^{-12} $m^2 \cdot s^{-1}$). This suggests that the electroactive species is the CO_2•A complex rather than CO_2 itself which, due to its small size, would be expected to diffuse relatively quickly, as compared to O_2 typically has a much bigger diffusion coefficient of around 10^{-10} $m^2 \cdot s^{-1}$ in RTIL.[41]

This RTIL layer is modelled as a linear space, within which the rate of change of the concentration of each species is affected by the rates of both diffusion and complex formation:

$$\frac{\partial C_i}{\partial t} = D_i \frac{\partial^2 C_i}{\partial x^2} \pm \left[k_\mathrm{f} C_{\mathrm{CO_2}} C_\mathrm{A} - k_\mathrm{b} C_{\mathrm{CO_2 \cdot A}}\right] \tag{4.7}$$

where t is time, x is perpendicular distance from the electrode surface and k_f and k_b are the rate constants for complex formation and dissociation respectively.

Note the $\pm$ symbol present in equation (4.7): for species CO_2 and A the kinetic term should be subtracted from the diffusional term, for the complex CO_2•A the kinetic term should be added to the diffusional term.

Initially only ionic liquid is present, *i.e.* neither dissolved CO_2 nor CO_2•A are present, and both the RTIL and the complex are subject to zero-flux boundary conditions at both the electrode surface and RTIL surface.

Under flow of CO_2 we assume that CO_2 dissolves rapidly at the RTIL surface and that an equilibrium concentration is rapidly attained. Thus locally equilibrium at the gas/liquid interface is assumed to be rapidly attained; in contrast, the diffusion of the complex to the liquid/electrode interface is slow. Thus for $t > 0$ we assume that the CO_2 concentration maintains a constant value at the boundary. Similarly, when under vacuum we assume that CO_2 is rapidly removed from the RTIL surface and so the concentration is assumed to be zero at the boundary. In both cases CO_2 is also subject to a zero-flux boundary condition at the electrode surface.

Equation (4.5) is solved subject to the above boundary conditions using the backwards implicit finite difference method.[42] The grid of points employed was not regular: the grid spacing expanded outwards from both the electrode surface and IL surface. The non-linear kinetic term in equation (4.7) was linearised using the method described in Britz.[42] Upon discretisation the system of simultaneous equations may be arranged as a matrix equation which may be solved using the Thomas algorithm.[42] The fitting will be shown later in this chapter.

4.3.2 Cyclic Voltammetry Study of RTILs and CO_2 System

Carbon dioxide was purged into a range of RTILs including [C_4mim][Ac], [C_4mim][BF_4], [C_4mim][NTf_2], [C_4mim][FAP] and [C_2mim][Ac] to study the cyclic voltammetry of CO_2 in these media. **Figure 4.5** shows the resultant voltammograms.

It is seen from **Figure 4.5** that compared to other RTIL systems which either have less recognisable voltammetric peaks, or unusual signal due to the contaminant (**Figure 4.5c**), the voltammogram of [C_4mim][Ac] system shows the best resolved voltammetric peak after exposure to CO_2, which is distinct and well-defined compared to the voltammogram in the absence of CO_2. This is likely associated with complex formation in which the latter is more activated to reduction. The system contains both the IL and internal reference decamethylferrocene before exposure to CO_2 as the Ag pseudo reference electrode may cause peak shift in different study, but the peak potential relative to internal reference remained the same. The reduction of CO_2 is associated with the peak at potentials around -1.8 V vs. Ag, whilst - 2.1 V, relative to internal reference decamethylferrocene. **Figure 4.6** shows the voltammetric peak for the reduction of the complex relative to the internal decamethylferrocene reference.

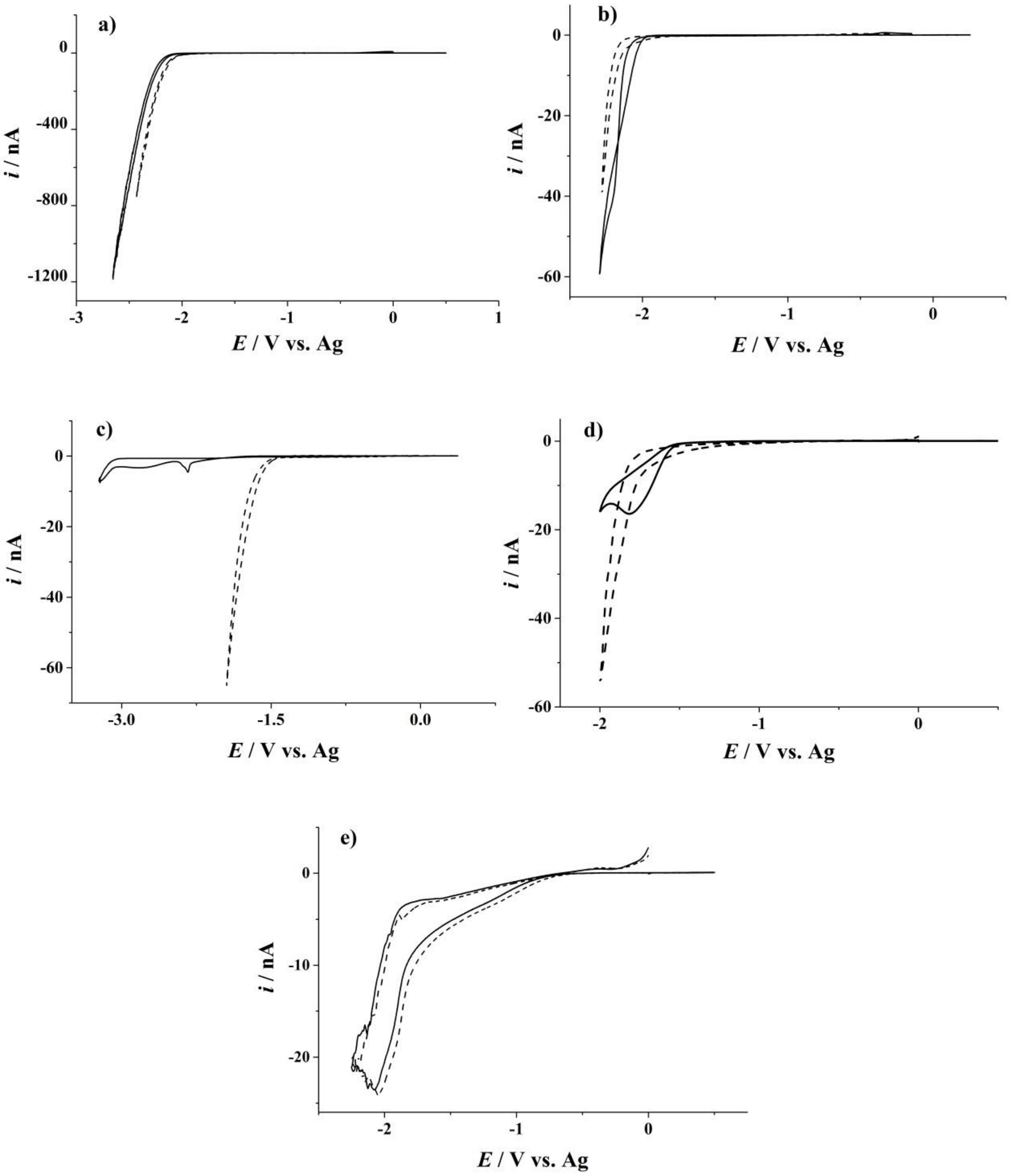

Figure 4.5: Voltammetry recorded in RTILs a) [C_4mim][NTf_2], b) [C_4mim][BF_4], c) [C_4mim][FAP], d) [C_4mim][Ac] and e) [C_2mim][Ac] after exposure to CO_2 (▬) and in the absence of CO_2 (---). All recorded with a 5.5 µm radius Pt microelectrode at a scan rate of 100 mV·s^{-1}.

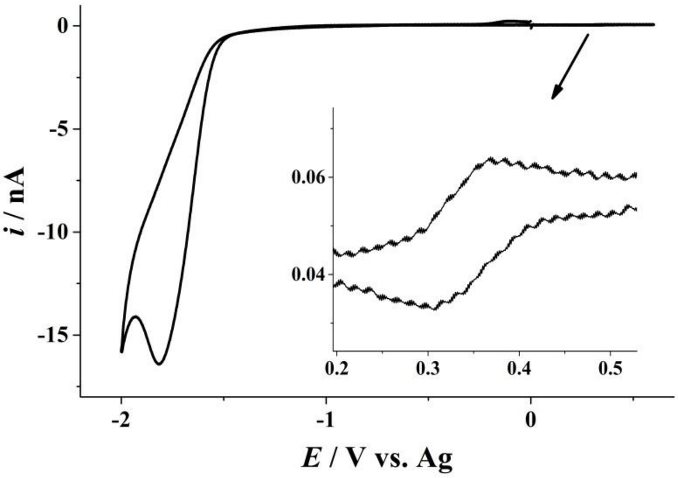

Figure 4.6: Voltammetry recorded in RTILs [C_4mim][Ac] after exposure to CO_2. The inset shows the voltammetric peak for the internal reference DmFc in the RTIL.

Note that in **Figure 4.5d** the background solvent decomposition signal is shifted to more negative potentials in the presence of CO_2 probably due to changed chemistry.[43] Also the size of the peak at - 1.8 V vs. Ag reflects both the concentration of the dissolved CO_2 as a complex and also the very low diffusion coefficient of the diffusing species as discussed below. The voltammetric peak is assumed to be diffusion controlled[43] on the basis of the chronoamperometry discussed below.

Separate experiments performed using mixtures of [C_4mim][Ac] and [C_4mim][NTf_2] with varying composition confirmed that no voltammetric peak is observed in the absence of [C_4mim][Ac] (see **Figure 4.5a** for pure [C_4mim][NTf_2] voltammogram) and that the voltammetric peak potential is dependent of the concentration of [C_4mim][Ac]. **Figure 4.7a** shows the voltammograms recorded after CO_2 saturation in pure [C_4mim][Ac] and three mixtures of [C_4mim][Ac] and [C_4mim][NTf_2] in different ratios. It is seen that as the ratio of [C_4mim][Ac] decreased, the reduction peak became difficult to recognise, which finally lead to no recognisable peak. The concentration of the electroactive species in each RTIL mixture was measured using chronoamperometry, as shown in **Figure 4.7b,** and the resulting transients were then analysed using Shoup & Szabo equation explained in section **4.2.2** to calculate the concentration. **Figure 4.7c** shows the linear dependence between the concentrations of electroactive species and the mole percent of [C_4mim][Ac]. The reduction peak current has a larger value with lower proportion of [C_4mim][Ac] whereas the corresponding concentration of electroactive species in **Figure 4.7c** has a lower value. This can be explained by the change of diffusion property of the electroactive species in the mixtures with different composition of two RTILs. Meanwhile, the reason for **Figure 4.7c** does not go through origin may be attributed to the sudden change of dissolution of CO_2 in pure [C_4mim][NTf_2] where clearly no reduction peak can be found, as shown in **Figure 4.5a**.

These results strongly suggest that CO_2 is not itself the electroactive species being detected, but rather that the dissolved gas forms an electroactive complex with the [C_4mim][Ac] solvent.

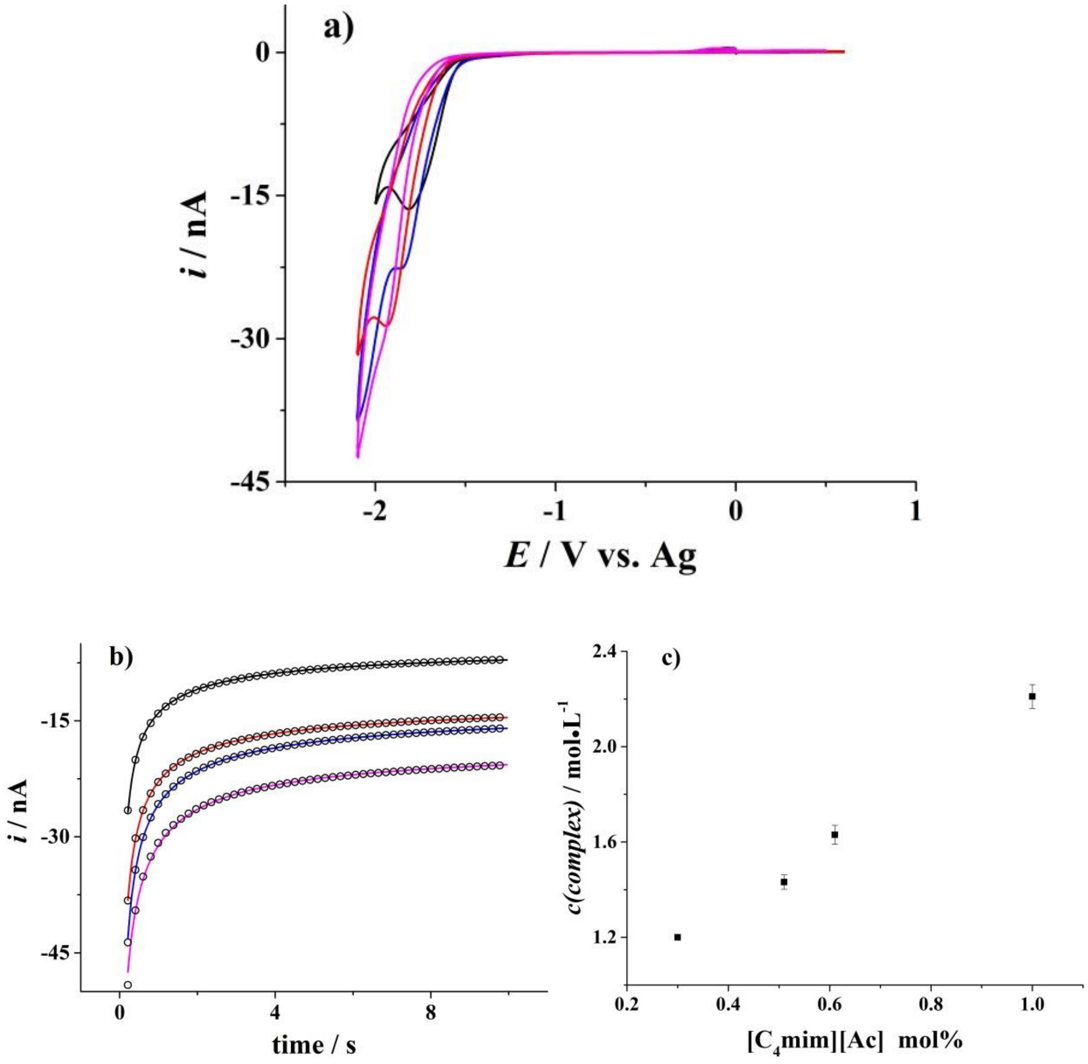

Figure 4.7: a) Voltammetry after CO_2 saturation recorded in pure [C_4mim][Ac] (▬), 61 mol% [C_4mim][Ac] (▬), 51 mol% [C_4mim][Ac] (▬), and 30 mol% [C_4mim][Ac] (▬), with the rest made up of [C_4mim][NTf_2]; b) Chronoamperometric transient (same aforementioned line colour designation) along with Shoup-Szabo fitting (○) c) Linear dependence between the concentration of electroactive species c(complex) and aforementioned mole percent of [C_4mim][Ac].

4.3.3 Measuring the Uptake and Release of CO_2

A series of experiments were next performed to investigate the uptake and release of CO_2 in [C_4mim][Ac]. Cyclic voltammetry and chronoamperometry was recorded at intervals while first CO_2 was flowed over the RTIL and then while the dissolved CO_2

was removed under vacuum. Voltammograms recorded at different time after exposure to CO_2 are shown in **Figure 4.8** below. It is seen from **Figure 4.8a** that the reduction peak current at around - 1.8 V vs. Ag became relative stable after around 400 minutes exposure to CO_2. A similar trend can be found in **Figure 4.8b** of the chronoamperometric measurements where the transient after 500 minutes overlaid perfectly. Thus suggests that the CO_2 – [C_4mim][Ac] interaction has reached equilibrium.

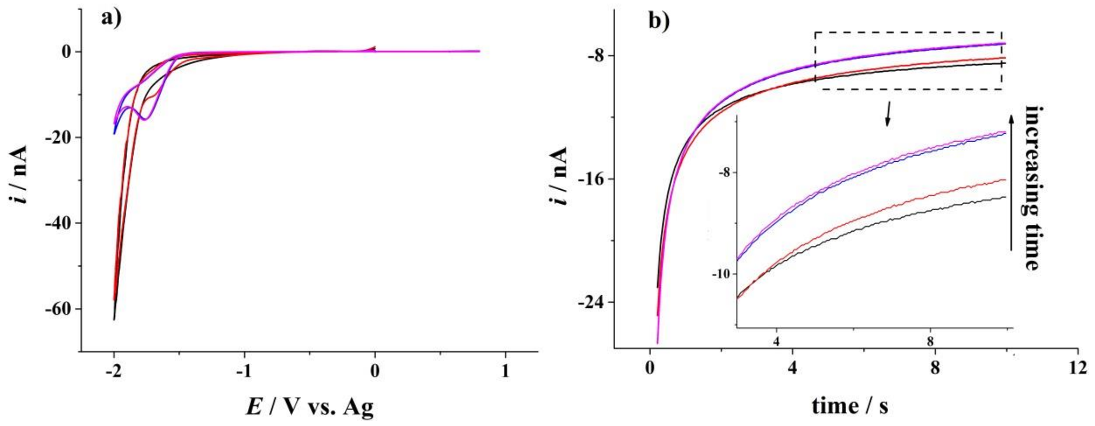

Figure 4.8: a) Cyclic voltammograms recorded after exposure to CO_2 at 5 (▬), 20 (▬), 390 (▬) and 450 (▬) minutes; b) Chronoamperometry recorded at 35 (▬), 180 (▬), 500 (▬) and 1100 (▬) minutes, at - 1.8 V vs. Ag.

The analysis of an experimental transient recorded after exposure 1100 minute of CO_2 is then shown separately in a black curve in **Figure 4.9**. The software package Origin 8.1 (Microsoft software Inc.) was used to fit the experimental data, as shown in black circles. The Shoup and Szabo equation (4.3) was imported into the nonlinear curve fitting programme in Origin. The value for the electrode radius of 5.5 μm (measured as detailed in Chapter 3) was fixed, and values for concentration *c* and diffusion coefficient *D* were obtained by fitting of the experimental data.

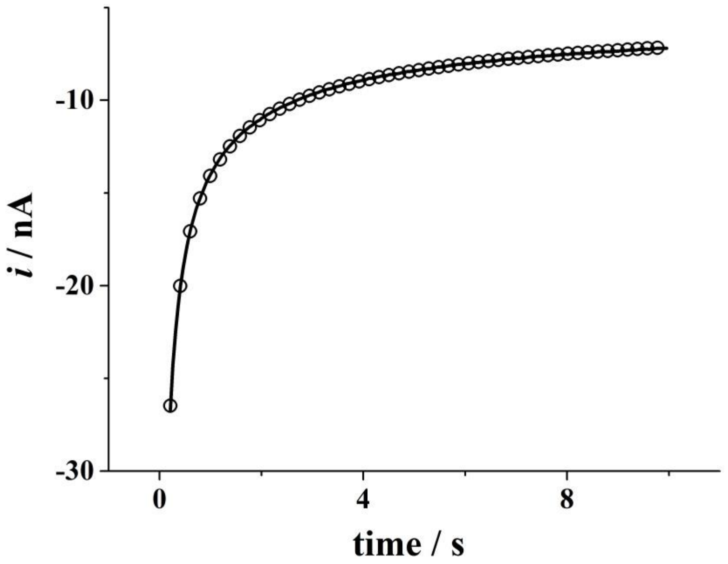

Figure 4.9: Typical chronoamperometric transient (▬) along with Shoup and Szabo fitting (○). The electrode potential was stepped from ca. 0.0 V to -1.8 V vs. Ag.

In order to obtain accurate value of *c* and *D*, the experimental chronoamperometric data was compared with the simulated transient using Shoup and Szabo equation systematically for a range of *c* and *D* values. Then the current in each data point from experimental transient was compared with current generated from Shoup and Szabo equation, thus the errors can be quantified by MSAD as explained in equation (4.5). After repeated for a range of *c* and *D* values, the 'best' values of *c* and *D* were obtained from the combination of c and D which yielded the lowest MSAD. **Figure 4.10** below shows the 2D contour plot of MSAD from the chronoamperometric response of the reduction of electroactive species where the concentration and diffusion coefficient corresponding to the x and y axis, respectively. The values of MSAD in the contour plot were indicated by the list of colour on the right of the plot. The minimum MSAD appeared where $c = 2.21$ mol·L^{-1} and $D = 9.20 \times 10^{-13}$ m^2·s^{-1}, which is shown in the black region in the plot. As can be seen that the black region radiates out into brown, thus there is a range of c (2.21 ± 0.12 mol·L^{-1}) and D (9.20 ± 0.51 × 10^{-13} m^2·s^{-1}) values which satisfies the fitting criteria of a MSAD value less than 0.005.

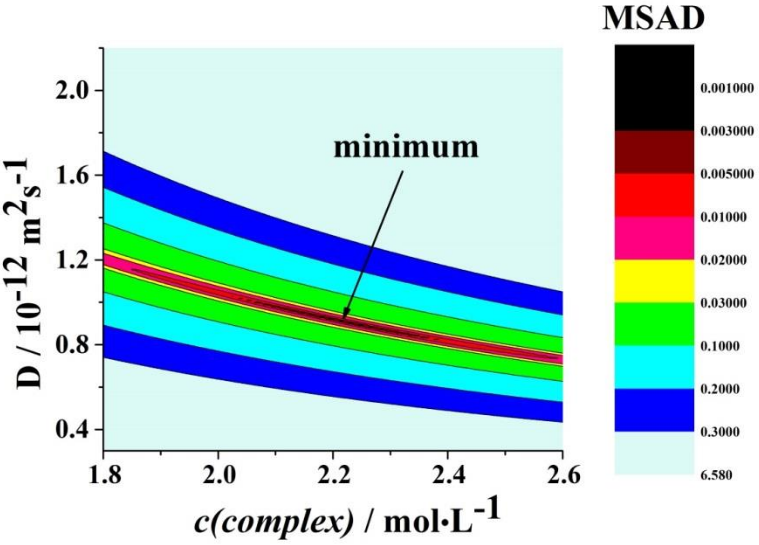

Figure 4.10: 2D contour plot of MSAD where the colour corresponding to the MSAD is listed to the right. The result was obtained from the reduction of electroactive species in [C$_4$mim][Ac] after exposure to CO$_2$ for 1100 minutes.

The analysis of each transient using the above method yielded the concentration of electroactive species in the immediate vicinity of the electrode surface as a function of time (shown in **Figure 4.11a**). The theoretical model introduced in **4.3.1** is used here to simulate the concentration – time data for the uptake of CO$_2$ by [C$_4$mim][Ac], as explained in equation (4.7). The proposed mechanism has three possible rate-determining steps: (i) uptake/release of CO$_2$ at the gas-liquid interface, (ii) formation/dissociation of the complex or (iii) diffusion of the complex.

Fitting of the experimental data was attempted assuming various possible rate-determining steps. **Figure 4.11** shows the experimental and simulated change of *c(complex)* divided by its saturated concentration C_{sat}, which equals 2.21 mol·dm^{-3}, with respect to time. Under flow of CO_2 (as the data from 0 to 400 minutes shown in **Figure 4.11a**), it was found that neither rate limiting CO_2 dissolution nor rate limiting complex formation were able to reproduce the extremely rapid accumulation at the electrode surface – each gave a much less steep curve than was observed experimentally. It was only possible to reproduce the rapid accumulation at the electrode if both CO_2 dissolution and complex formation were both fast. Thus diffusion of the complex through the solution was found to be the rate-limiting factor for CO_2 uptake.

When considering the removal of CO_2 under vacuum (as the data from 1500 to 9000 minutes shown in **Figure 4.11a**), rate-limiting diffusion, however, is not consistent with the much slower removal of CO_2 under vacuum. Were diffusion to be rate limiting then the removal of CO_2 would be expected to take place on the same timescale as the uptake. The experimental data, however, shows that the removal of CO_2 is a much slower process than the uptake. Of the two remaining possible rate limiting processes, it was found that assuming rate limiting complex dissociation gave a much better fit to the experimental data. Comparison with the experimental data suggested that dissociation of the complex, rather than CO_2 release, was rate-limiting.

Therefore, the best fit parameters (shown in the legend of **Figure 4.11**) of diffusion coefficient D and rate constant k for forward (k_f), backward (k_b) process were determined. The rate constants are derived in equation (4.7). The system reached saturation after around 400 minutes with a maximum limiting concentration of 2.21 mol·dm^{-3}. The removal of dissolved CO_2 was observed to be much slower than the initial uptake because of the powerful complexation between CO_2 and [C_4mim][Ac] and the slow diffusion of the complex. A plot of ln(*c(complex)*) against time for the removal was found to be *approximately* linear with a slope of 3.3×10^{-4} min^{-1}, as shown in **Figure 4.11b**.

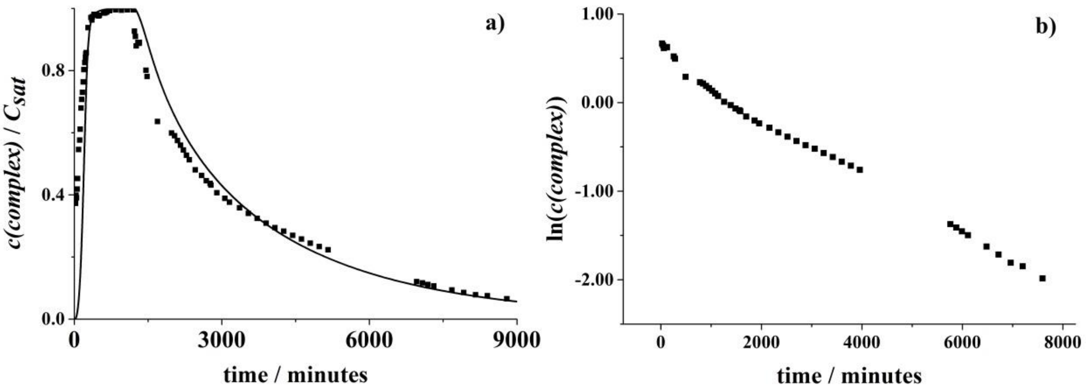

Figure 4.11: a) Experimental (■) and simulated (▬) concentration of electroactive species (as a fraction of the saturated concentration, C_{sat}) as a function of time. Best fit parameters: $D_{CO2} = 2 \times 10^{-6}$ cm^2·s^{-1}, $D_{RTIL} = 1 \times 10^{-8}$ cm^2·s^{-1}, $D_{complex} = 1 \times 10^{-8}$ cm^2·s^{-1}; $k_f = 1$ cm^3·mol^{-1}·s^{-1}, $k_b = 9.1 \times 10^{-5}$ s^{-1}; the height of the RTIL above the electrode is 0.2 cm. b) Natural logarithm of the concentration of electroactive species c(complex) against time shows a linear dependence with a slope of 3.3×10^{-4} min^{-1}.

4.3.4 Temperature Dependence of the Rate of CO_2 Uptake

Next, this same electrochemical methodology was used to measure the temperature dependence of the limiting complex concentration, *c(complex)*, and diffusion coefficient, *D*, respectively. Potential step transients were recorded for saturated [C_4mim][Ac] solutions at six different temperatures, namely 276, 287, 298, 303, 308 and 313 K. Analysis of these transients yielded both a limiting concentration and a diffusion coefficient for the electroactive species as a function of temperature (**Figure 4.12**). It is seen from **Figure 4.12a** that the CO_2 uptake, as indicated voltammetrically by the reduction peak around - 1.8 V vs. Ag, increased slightly with temperature. A plot of ln(D) against 1/T in **Figure 4.12b** was found to be linear, which is consistent with an Arrhenius-type temperature dependence[44], which has an apparent activation energy of + 35 kJ·mol^{-1}.

$$\ln(D) = -\frac{E_a}{R}\frac{1}{T} + \ln(A) \tag{4.8}$$

where E_a is the activation energy, R is the universal gas constant and A is the prefactor. Values for the activation energy of diffusion of CO_2 in a range of RTILs have previously been recorded in the region of + 16 kJ·mol^{-1}.[45] This suggests that the electroactive species in our system is somewhat larger than CO_2, which is consistent with the electroactive species being a complex rather than CO_2 itself.

A plot of ln(*c(complex)*) against 1/T in **Figure 4.12c** was found to be linear, which is consistent with an Van't Hoff type temperature dependence,[46] which has an enthalpy change of + 6.9 kJ·mol^{-1}.

$$\ln(c(complex)) = -\frac{\Delta H}{R}\frac{1}{T} + \ln(B) \tag{4.9}$$

where ΔH is the enthalpy change of the CO_2 solvation process and B is the prefactor. This value apparently suggests that the formation of electroactive species in this system is in favour of higher temperature, which is controversial in respect of previously reported values around -35 kJ·mol^{-1}.[47,48] However, note that in solubility measurement of the type reported in this chapter, the $\varDelta H$ values for the electroactive species solubility are differential enthalpies of solubility pertaining to gas saturation, which is the rate of the change of enthalpy ΔH with the increase of $n_{complex}$, equation (4.10).

$$\varDelta H_{sol} = (\frac{\partial \varDelta H}{\partial n_{complex}})_{T,p,n_A} \tag{4.10}$$

where $\varDelta H_{sol}$ is the differential enthalpy of solution, at a given temperature T and pressure p, n_A is the number of moles of solvent, which is the ionic liquid in this case. For the measurement reported the data related to the CO_2 saturated solution.

These, in principle, can be quite different (even to the extent of differing in sign) from the corresponding molar integral values, which are the integral enthalpy changes divided by the amount of solute transferred, seen in equation (4.11).

$$\varDelta H_m = \frac{\varDelta H}{n_{complex}} \tag{4.11}$$

where $\varDelta H_m$ is molar integral enthalpy of solution. The two quantities are related in the sense that if a graph of $\varDelta H$, the integral enthalpy of solution is plotted as a function of molality, then the value of the slope at a given molality gives the differential enthalpy $\varDelta H_{sol}$ of solution at that concentration.[49,50]

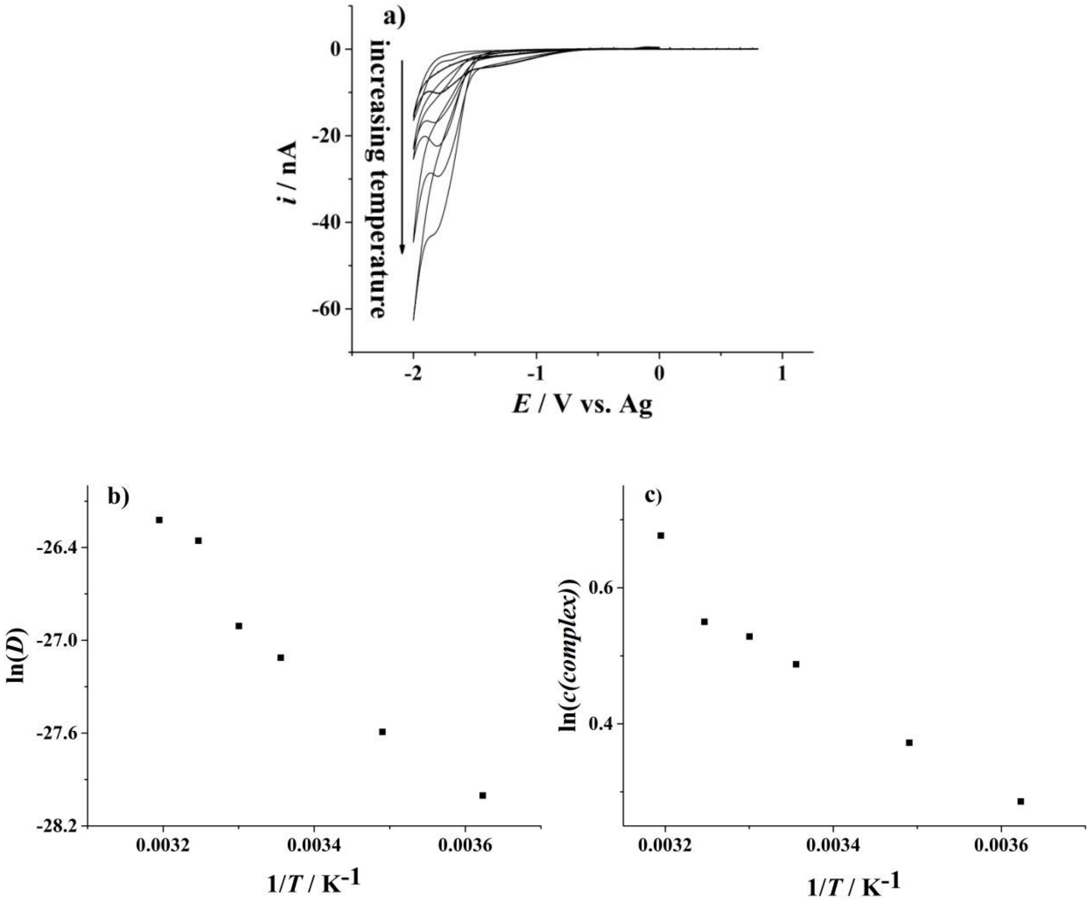

Figure 4.12: a) Cyclic voltammograms recorded after exposure to CO_2 at 276, 287, 298, 303, 308 and 313 K, the reduction peak current around -1.8 V vs. Ag increases with increasing temperatures. b): The natural logarithm of Diffusion coefficient against 1/*T* plot reflects a linear dependence with an activation energy of 35 kJ·mol^{-1}. c) The natural logarithm of the concentration of electroactive species against 1/*T* plot reflects a linear dependence with an enthalpy change of + 6.9 kJ·mol^{-1}.

Note that for the present system the diffusion coefficient is a function of concentration as well as temperature, as discussed in the following section. Since limiting concentration is itself slightly temperature dependent, the diffusion coefficient values (measured for a saturated solution) used in the Arrhenius analysis correspond to both varying temperatures and varying concentrations. Thus the exact value of the activation energy estimated is approximate. Nevertheless its large value remains indicative of an electroactive complex, rather than electroactive CO_2.

4.3.5 Variable Partial Pressure Experiments

The uptake of gases into RTIL systems as a function of pressure sometimes follows Henry's law type behaviour.[51]

$$p = k_H c \tag{4.12}$$

where p is the partial pressure of the gas, k_H is the Henry's constant and c is the concentration of the dissolved gas. This is usually the case for gases with low solubility and where no complexation occurs with the solvent. In the present situation, however, the amount of gas absorbed by the RTIL is extremely large. Moreover the uptake may be accompanied by significant volume changes in addition to the inferred complex formation. Thus Henry's law type behaviour is not expected for the system under study. Rather if the complex formation is strong then the uptake of gas will be very similar regardless of the CO_2 gas pressure (above some minimum threshold) reflecting the stoichiometric uptake of gas.

The non-applicability of Henry's law to the current system was examined by experiments in which three mixtures of CO_2 and N_2 of varying composition were flowed over [C_4mim][Ac] and the uptake/release of CO_2 studied at 298 K. In each case the total pressure was fixed at 1 atmosphere. Flow meters were employed to control the CO_2 and N_2 concentrations in the mixture. The concentration of eletroactive species was measured and analysed as described in **4.3.3**. **Figure 4.13a** shows cyclic voltammograms and **Figure 4.13b** shows the transient measuremnts in the gas mixture system. It was observed that the mixtures containing 75% CO_2 and 50% CO_2 have very similar cyclic voltammograms and reached almost the same limiting concentration of electroactive species (1.32 ± 0.01 M and 1.36 ± 0.02 M respectively), while the mixture containing 25% CO_2 reached a slightly smaller value (0.82 ± 0.01 M).

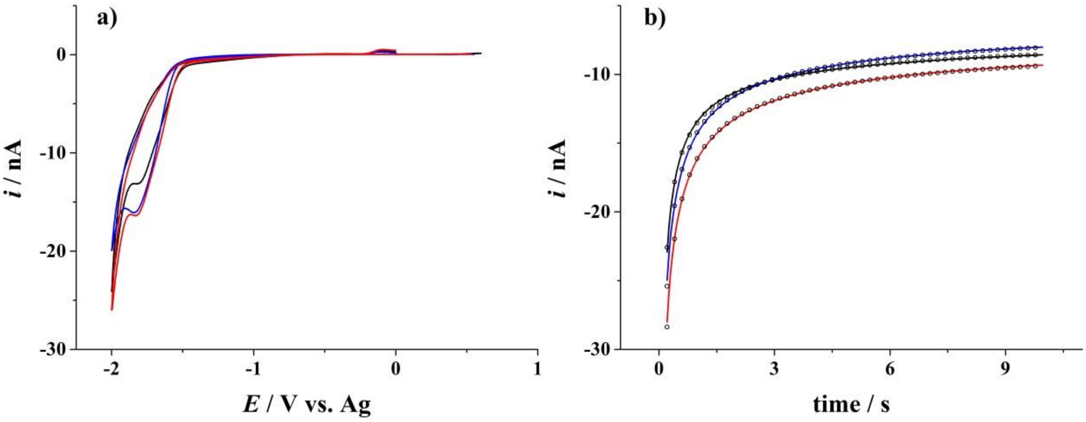

Figure 4.13: a) Cyclic voltammograms recorded with 25 (▬), 50 (▬) and 75 (▬) vol% CO_2 in the gas mixture, with the rest made up of N_2; b) Chronoamperometry recorded at aforementioned CO_2 vol% in gas mixtures, with fitted transient (○). All measurements were carried out at 298 K.

The limiting (i.e. equilibrium) concentration of electroactive species should vary linearly with the partial pressure of CO_2 according to Henry’s law. The above data clearly do not follow this trend, confirming the current system is far from an ideal solution and Henry’s law is not applicable.

Analysis of the chronoamperometric transients recorded during CO_2 uptake and release for these mixtures reveals that the diffusion coefficient of the electroactive species is dependent upon its concentration. The effect of dissolved gases on the diffusion coefficients of solutes has been shown above and has been attributed to the concentration being so high as to alter the transport properties of the solvent**.** Importantly, all three mixtures show a similar variation of *D* with *c* (shown in **Figure 4.14**) for both the uptake and release of CO_2, demonstrating the reliability and reproducibility of results derived using this method. Furthermore, the relatively small diffusion coefficient (10^{-12} $m^2 \cdot s^{-1}$) support the idea of complexation between CO_2 and RTIL since it is unlikely for a gas to diffuse so slowly in a pure inert RTIL.

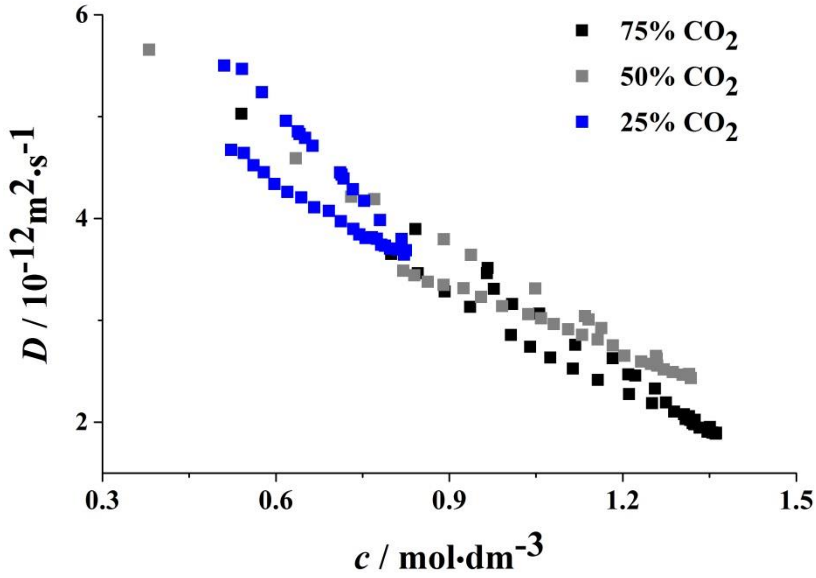

Figure 4.14: Variation of diffusion coefficient with concentration for electroctive species in $[C_4mim][Ac]$ for three mixtures of CO_2 and N_2 at 298 K.

4.4 Conclusions

The method proposed allows both the limiting CO_2 uptake and kinetics of CO_2 uptake/release to be determined in a single experiment. Very high uptake of CO_2 has been achieved such that Henry's law was found to be inapplicable. Nevertheless the method has been shown to be very reliable through experiments using mixtures of CO_2 and N_2 gas.

References

(1) Li, P.; Henstridge, M. C.; Xiong, L.; Compton, R. G. *Electroanalysis* **2013**, *25*, 2268.

(2) Rees, N. V.; Compton, R. G. *Energy & Environmental Science* **2011**, *4*.

(3) Zhang, J.; Zhang, S.; Dong, K.; Zhang, Y.; Shen, Y.; Lv, X. *Chemistry – A European Journal* **2006**, *12*, 4021.

(4) Aresta, M.; Dibenedetto, A. *Dalton Transactions* **2007**, *0*, 2975.

(5) Balat, H.; Öz, C. *Energy, Exploration & Exploitation* **2007**, *25*, 357.

(6) Sun, P.; Armstrong, D. W. *Analytica Chimica Acta* **2010**, *661*, 1.

(7) Welton, T. *Chemical Reviews* **1999**, *99*, 2071.

(8) Hallett, J. P.; Welton, T. *Chemical Reviews* **2011**, *111*, 3508.

(9) Cole, A. C.; Jensen, J. L.; Ntai, I.; Tran, K. L. T.; Weaver, K. J.; Forbes, D. C.; Davis, J. H. *Journal of the American Chemical Society* **2002**, *124*, 5962.

(10) Silvester, D. S.; Compton, R. G. *Zeitschrift für Physikalische Chemie* **2006**, *220*, 1247.

(11) Meng, Y.; Aldous, L.; Pilgrim, B. S.; Donohoe, T. J.; Compton, R. G. *New Journal of Chemistry* **2011**, *35*, 1369.

(12) Kubisa, P. *Progress in Polymer Science* **2009**, *34*, 1333.

(13) Fung, Y. S.; Zhou, R. Q. *Journal of Power Sources* **1999**, *81–82*, 891.

(14) Peng, J.; Deng, Y. *New Journal of Chemistry* **2001**, *25*, 639.

(15) Yang, H.; Gu, Y.; Deng, Y.; Shi, F. *Chemical communications* **2002**, *0*, 274.

(16) Feroci, M.; Orsini, M.; Rossi, L.; Sotgiu, G.; Inesi, A. *The Journal of Organic Chemistry* **2006**, *72*, 200.

(17) Chu, D.; Qin, G.; Yuan, X.; Xu, M.; Zheng, P.; Lu, J. *ChemSusChem* **2008**, *1*, 205.

(18) Yuan, D.; Yan, C.; Lu, B.; Wang, H.; Zhong, C.; Cai, Q. *Electrochimica Acta* **2009**, *54*, 2912.

(19) Shiflett, M. B.; Niehaus, A. M. S.; Elliott, B. A.; Yokozeki, A. *Int. J. Thermophys.* **2012**, *33*, 412.

(20) Shiflett, M. B.; Elliott, B. A.; Niehaus, A. M. S.; Yokozeki, A. *Separation Science and Technology* **2011**, *47*, 411.

(21) Shiflett, M. B.; Drew, D. W.; Cantini, R. A.; Yokozeki, A. *Energy & Fuels* **2010**, *24*, 5781.

(22) Gu, Y.; Zhang, Q.; Duan, Z.; Zhang, J.; Zhang, S.; Deng, Y. *J. Org. Chem.* **2005**, *70*, 7376.

(23) Heldebrant, D. J.; Koech, P. K.; Ang, M. T. C.; Liang, C.; Rainbolt, J. E.; Yonker, C. R.; Jessop, P. G. *Green Chem.* **2010**, *12*, 713.

(24) Paz, J.; Perez-Balado, C.; Iglesias, B.; Munoz, L. *J. Org. Chem.* **2010**, *75*, 3037.

(25) Almantariotis, D.; Stevanovic, S.; Fandino, O.; Pensado, A. S.; Padua, A. A. H.; Coxam, J. Y.; Costa, G. M. F. *J. Phys. Chem. B* **2012**, *116*, 7728.

(26) Shiflett, M. B.; Yokozeki, A. *Ind. Eng. Chem. Res.* **2005**, *44*, 4453.

(27) Palgunadi, J.; Kang, J. E.; Nguyen, D. Q.; Kim, J. H.; Min, B. K.; Lee, S. D.; Kim, H.; Kim, H. S. *Thermochim. Acta* **2009**, *494*, 94.

(28) Jacquemin, J.; Costa, G. M. F.; Husson, P.; Majer, V. *J. Chem. Thermodyn.* **2006**, *38*, 490.

(29) Jacquemin, J.; Husson, P.; Majer, V.; Padua, A. A. H.; Costa, G. M. F. *Green Chem.* **2008**, *10*, 944.

(30) Almantariotis, D.; Gefflaut, T.; Padua, A. A. H.; Coxam, J. Y.; Costa, G. M. F. *J. Phys. Chem. B* **2010**, *114*, 3608.

(31) Moganty, S. S.; Baltus, R. E. *Ind. Eng. Chem. Res.* **2010**, *49*, 5846.

(32) Shiflett, M. B.; Elliott, B. A.; Lustig, S. R.; Sabesan, S.; Kelkar, M. S.; Yokozeki, A. *ChemPhysChem* **2012**, *13*, 1806.

(33) Supasitmongkol, S.; Styring, P. *Energy Environ. Sci.* **2010**, *3*, 1961.

(34) Rogers, E. I. S., D. S.; Poole, D. L.; Aldous, L.;; Hardacre, C. C., R. G. *J. Phys. Chem. C* **2008**, *112*, 2729.

(35) Rosen, B. A.; Salehi-Khojin, A.; Thorson, M. R.; Zhu, W.; Whipple, D. T.; Kenis, P. J. A.; Masel, R. I. *Science* **2011**, *334*, 643.

(36) Shoup, D.; Szabo, A. *J. Electroanal. Chem. Interfacial Electrochem.* **1982**, *140*, 237.

(37) Xiong, L.; Aldous, L.; Henstridge, M. C.; Compton, R. G. *Anal. Methods* **2012**, *4*, 371.

(38) Paddon, C. A.; Silvester, D. S.; Bhatti, F. L.; Donohoe, T. J.; Compton, R. G. *Electroanalysis* **2007**, *19*, 11.

(39) Xiong, L., University of Oxford, 2014.

(40) Husson-Borg, P.; Majer, V.; Costa Gomes, M. F. *J. Chem. Eng. Data* **2003**, *48*, 480.

(41) Buzzeo, M. C.; Klymenko, O. V.; Wadhawan, J. D.; Hardacre, C.; Seddon, K. R.; Compton, R. G. *J. Phys. Chem. B* **2004**, *108*, 3947.

(42) Britz, D. *Digital Simulation in Electrochemistry*; Springer-Verlag: Heidelberg, 2005.

(43) Barrosse-Antle, L. E.; Compton, R. G. *Chemical communications* **2009**, 3744.

(44) Arrhenius, S. A. *Z. Physik. Chem.* **1889**, *4*, 96.

(45) Jindaratsamee, P.; Shimoyama, Y.; Morizaki, H.; Ito, A. *J. Chem. Thermodyn.* **2011**, *43*, 311.

(46) Atkins, P.; Paula, J. D. *Physical Chemistry*; W.H. Freeman & Company, 2009.

(47) Yokozeki, A.; Shiflett, M. B.; Junk, C. P.; Grieco, L. M.; Foo, T. *J. Phys. Chem. B* **2008**, *112*, 16654.

(48) Carvalho, P. J.; Alvarez, V. H.; Schroder, B.; Gil, A. M.; Marrucho, I. M.; Aznar, M.; Santos, L. M. N. B. F.; Coutinho, J. A. P. *J. Phys. Chem. B* **2009**, *113*, 6803.

(49) Negi, A. S.; Anand, S. C. *A Text Book of Physical Chemistry*; 2nd ed.; New Age International (P) Ltd.: New Delhi, 2004.

(50) Rajaram, J.; Kuriacose, J. C. *Chemical Thermodynamics Classical, Statistical and Irreversible*; Corling Kindersley Pvt. Ltd: India, 2013.

(51) Smith, F. L.; Harvey, A. H. *Chem. Eng. Prog.* **2007**, *103*, 33.

Chapter 5

The Microelectrode Voltammetry of Dioxygen Reduction in a Phosphonium Cation Based Room Temperature Ionic Liquid

This chapter investigates the electrochemical reduction of dioxygen, O_2, in the room temperature ionic liquid trihexyl(tetradecyl)phosphonium trifluorotris(pentafluoroethyl)phosphate $[P_{6,6,6,14}][FAP]$ (see **Figure 5.1** for the structure of the cation and anion). The nature of the unusual voltammetric waves is quantitatively modelled via digital simulation with the aim of clarifying apparent inconsistencies in the literature. The reduction is shown to proceed via a two-electron reaction and involve the likely capture of a proton from the solvent system. The oxidative voltammetric signals seen at fast scan rates are interpreted as resulting from the reoxidation of $HO_2^{\cdot -}$. In the presence of large amounts of dissolved carbon dioxide the reductive currents decrease by a factor of ca. two, consistent with the trapping of the superoxide radical, $O_2^{\cdot -}$, intermediate in the two-electron reduction process. The steady state current was shown to be linearly dependent on the oxygen partial pressure in high oxygen content (>77%) systems. Thus the simultaneous detecting of oxygen and carbon dioxide is realised in the oxygen/carbon dioxide mixture, providing proof-of-concept of high concentration oxygen and carbon dioxide dual sensing. This work was conducted partly in collaboration Dr. Edward O. Barnes who contributed the theory part in **5.4**. The work presented in this chapter has been published in *The Journal of Physical Chemistry C*[1] and *Electroanalysis*.[2]

5.1 Introduction

The electrochemistry of dioxygen in room temperature ionic liquid media has been widely studied, not least for its relevance in energy storage systems. Typical behaviour mirrors that seen in conventional organic solvents in which under dry conditions a fast electron transfer leads to the formation of the superoxide anion:[3-7]

$$O_2 + e \rightleftharpoons O_2^{\bullet -} \tag{5.1}$$

The superoxide ion behaves as a strong base so that in the presence of a proton source such as water, an irreversible disproportionation is thought to be possible: [8-10]

$$2O_2^{\bullet -} + H_2O \longrightarrow O_2 + HOO^- + OH^- \tag{5.2}$$

Voltammetrically this is visible through the loss of the back voltammetric peak corresponding to the reoxidation of $O_2^{\bullet -}$. Under dry conditions the superoxide species is stable and has been widely studied electrochemically. Examples of ionic liquid media where the O_2/ $O_2^{\bullet -}$ couple has been observed with relative stability of the superoxide inferred are given in **Table 5.1**. In contrast, the superoxide ion is reported to be reactive in some phosphonium-based ionic liquids.[3,11,12] Typical examples of the latter are given in **Figure 5.1** along with their structures where $P^+_{a,b,c,d}$ reflects the number (a, b, c and d) of carbon atoms in the four alkyl chains. The ions and abbreviations of all the ionic liquids mentioned in this Chapter are given in **Table 5.2**.

Table 5.1: Ionic liquids with reported stability of superoxide as judged electrochemically.

Ionic liquids	**Abbreviations**
1-Butyl-1-methylpyrrolidinium bis(trifluoromethanesulfonyl)imide	[BMP][NTf$_2$][13]
1-Butyl-3-methylimidazolium hexafluorophosphate	[C$_4$mim][HFP][14]
1-Butyl-3-methylimidazolium bis(trifluoromethanesulfonyl)imide	[C$_4$mim][NTf$_2$][7]
1-hexyl-1-methyl-pyrrolidinium bis(trifluoromethanesulfonyl)imide	[HMPyrr][NTf$_2$][15]
1-(2-methoxyethyl)-1-methylpiperidinium tris(pentafluoroethyl)trifluorophosphate	[MOEMPip][FAP][16]
1-(3-methoxypropyl)-1-methylpiperidinium bis(trifluoromethanesulfonyl)imide	[MOPMPip][NTf$_2$][15]
Trimethyl-n-hexylammonium bis(trifluoromethanesulfonyl)imide	[TMHA][NTf$_2$][13]

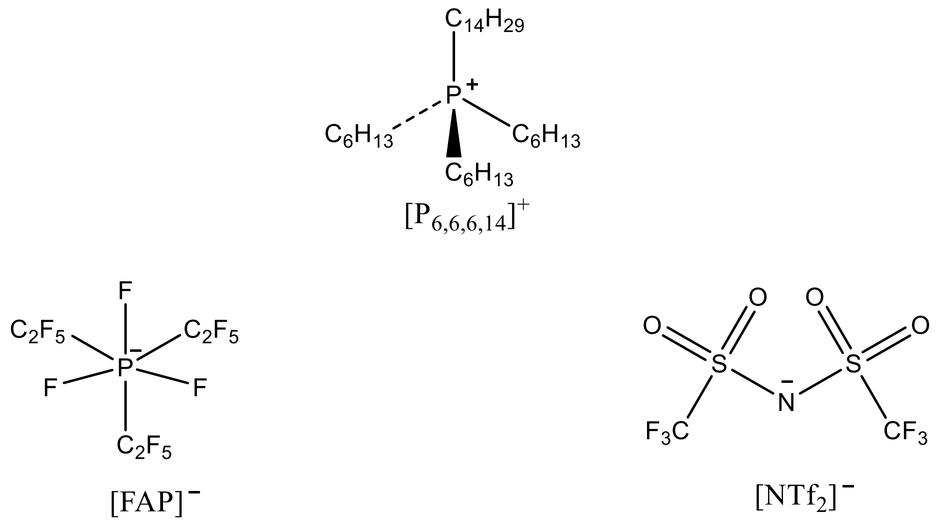

$[P_{6,6,6,14}]^+$

$[FAP]^-$

$[NTf_2]^-$

Figure 5.1: Structures of the phosphonium-based ionic liquid cation and two anions.

Table 5.2: Ions and Abbreviations of all the ionic liquids presented this Chapter

Ionic liquids	**Abbreviations**
1-Butyl-1-methylpyrrolidinium bis(trifluoromethanesulfonyl)imide	[BMP][NTf_2]
1-Ethyl-3-methylimidazolium bis(trifluoromethanesulfonyl)imide	[C_2mim][NTf_2]
1-Butyl-2,3-methylimidazolium bis(trifluoromethanesulfonyl)imide	[C_4dmim][NTf_2]
1-Butyl-3-methylimidazolium tetrafluoroborate	[C_4mim][BF_4]
1-Butyl-3-methylimidazolium heptafluorobutyrate	[C_4mim][$CF_3CF_2CF_2COO$]
1-Butyl-3-methylimidazolium hexafluorophosphate	[C_4mim][HFP]
1-Butyl-3-methylimidazolium bis(trifluoromethanesulfonyl)imide	[C_4mim][NTf_2]
1-Butyl-3-methylimidazolium hexafluorophosphate	[C_4mim][PF_6]
N-Butyl-N-methylpyrrolidinium bis(trifluoromethanesulfonyl)imide	[C_4mpyrr][NTf_2]
Diethylmethylammonium trifluoromethanesulfonate	[dema][TfO]
1-Hexyl-1-methyl-pyrrolidinium bis(trifluoromethanesulfonyl)imide	[HMPyrr][NTf_2]
N-Butyl-N-methyl pyrrolidinium bis(trifluoromethylsulfonyl)imide	[MeBuPyrr][NTf_2]
1-(2-Methoxyethyl)-1-methylpiperidinium tris(pentafluoroethyl)trifluorophosphate	[MOEMPip][FAP]
Bis(2-methoxyethyl)ammonium benzoate	[$(MeOEt)_2NH$][C_6H_5COOH]
1-(3-Methoxypropyl)-1-methylpiperidinium bis(trifluoromethanesulfonyl)imide	[MOPMPip][NTf_2]
n-Hexyltriethylammonium bis(trifluoromethanesulfonyl)imide	[$N_{6,2,2,2}$][NTf_2]

Trihexyl(tetradecyl)phosphonium trifluorotris(pentafluoroethyl)phosphate	$[P_{6,6,6,14}][FAP]$
Trihexyl(tetradecyl)phosphonium bis(trifluoromethanesulfonyl)imide	$[P_{6,6,6,14}][NTf_2]$
N-methyl-N-butylpyrrolidinium bis(trifluoromethylsulfonyl)imide	$[Py_{14}][NTf_2]$
Trimethyl-n-hexylammonium bis(trifluoromethanesulfonyl)imide	$[TMHA][NTf_2]$

A recent report by MacFarlane and colleagues has addressed the issue of superoxide stability in phosphonium cation trihexyl(tetradecyl)phosphonium-based ionic liquids.[9] Conflicting literature reports exist with some groups finding superoxide not to be stable but with others claiming the opposite. The differences *may* reflect contrasting levels of impurities or possibly changed behaviour reflecting the anionic component of the liquid. **Table 5.3** summarises the various claims.

Typically the voltammetric characteristics of superoxide stability depend on the observation of an oxidative back peak in cyclic voltammetry, as mentioned above. Often this approach is qualitative or semiqualitative, usually of necessity, reflecting the ohmic distortion of the voltammetric signals typically encountered in ionic liquids as a result of their often high resistance coupled with the use of macrosized electrodes. This commonly prevents the rigorous simulation of the voltammetry as would normally be undertaken in the study of molecular processes in more conductive solvents, both aqueous and nonaqueous. Specifically the effect of high resistance solvent media is to increase the peak to peak separation. Under these conditions, it is often hard to unambiguously assign the reverse voltammetric peak to the simple reverse of the process seen on the forward scan.[3,11] In particular the distinction between the process

$$A \pm e \rightleftharpoons B \tag{5.3}$$

on the one hand and the ECE type mechanism[3]

$$A \pm e \longrightarrow B \tag{5.4}$$

$$B \xrightarrow{\text{fast}} C \tag{5.5}$$

$$C \pm e \longrightarrow X \tag{5.6}$$

is challenging if the kinetics of the B to C reaction are fast. Of course the transformation of the second type can most likely occur via a DISP[17] type reaction rather than the ECE scheme depicted.[18] In particular, identifying a back peak due to the oxidation of B to A in the simpler process versus that of X to C in the ECE/DISP mechanism is challenging in the absence of quantitative simulation.

We have previously advocated a microelectrode approach for the determination of electrode reaction mechanisms in ionic liquids.[11,19-22] Partly this is because such an approach more readily facilitates the use of small volumes of solution greatly aiding the removal of dissolved gases or traces of water by the use of a vacuum-based T-cell.[11,19,23] At the same time the much reduced currents seen at microelectrodes lower the chances of ohmic distortion, and quantitatively modelling of the electrode process of interest is usually possible.

Table 5.3: $O_2^{\bullet -}$ stability in phosphonium cation trihexyl(tetradecyl)phosphonium based ionic liquids

Cation	Anion	Mechanism	Claims
$[P_{6,6,6,14}]^+$	$[FAP]^-$	$O_2 + e \rightleftharpoons O_2^{\bullet -}$	Electrochemical stability[24]
		$O_2 + e \rightleftharpoons O_2^{\bullet -}$ $O_2^{\bullet -} + IL \longrightarrow HO_2^{\bullet} + X$	No electrochemical stability[16]
		$O_2 + e \rightleftharpoons O_2^{\bullet -}$ $O_2^{\bullet -} + IL \longrightarrow HO_2^{\bullet} + X$	No electrochemical stability[3]
$[P_{6,6,6,14}]^+$	$[Cl]^-$	$O_2 + e \rightleftharpoons O_2^{\bullet -}$	Long term stability[9]
		$O_2 + 2H^+ + 2e \longrightarrow H_2O_2$	No electrochemical stability[12]
		$O_2 + e \rightleftharpoons O_2^{\bullet -}$ $O_2^{\bullet -} + H_2O \rightleftharpoons HO_2^{\bullet} + OH^-$ $HO_2^{\bullet} + O_2^{\bullet -} \rightleftharpoons HO_2^- + O_2$ $HO_2^- + H_2O \longrightarrow H_2O_2 + OH^-$	Electrochemical stability[8]
$[P_{6,6,6,14}]^+$	$[NTf_2]^-$	$O_2 + e \rightleftharpoons O_2^{\bullet -}$	Electrochemical stability[9]
		$O_2 + e \rightleftharpoons O_2^{\bullet -}$ $O_2^{\bullet -} + IL \longrightarrow X$ $X - e \longrightarrow Product$	No electrochemical stability[11]
		$O_2 + 2e + HA \longrightarrow H_2O_2 + 2A^-$	No electrochemical stability[25]
		$O_2 + e \rightleftharpoons O_2^{\bullet -}$	Electrochemical stability[26]
		$O_2 + e \rightleftharpoons O_2^{\bullet -}$	Electrochemical stability[10]

The aim of this chapter is to apply quantitative microelectrode methodology to the reduction of dioxygen in the phosphonium-based ionic liquid $[P_{6,6,6,14}][FAP]$ with the aim of realising mechanistic resolution and discover the potential of this RTIL to be developed into an O_2/CO_2 dual sensor which can be applied for various applications possibly including medical treatment[27-41] and spacecraft O_2 sensing[42] where the gas mixtures have high O_2 content.

5.2 Experimental

The experiments with mixed N_2 and O_2 were realised as follows: the inlet lines of both N_2 and O_2 were each connected to a flow meter (Platon, UK) which controlled the flow rate of each gas (see **Figure 5.2**). The combined O_2 flow rate v_{O2} and N_2 flow rate v_{N2} into the T-cell is 1100 mL/min, making up the total flow rate at fixed pressure, 1 bar. When the O_2 flow rate was adjusted from 0 to 1100 mL/min, the rest consisted of N_2. These two lines were merged after passing through the flow meters into a single inlet line which then passed through a Dreschel bottle containing $CaCl_2$/4 Å molecular sieves to dry the gas. The outlet line from the Dreschel bottle was then connected to the T-cell, purging dried gas into the cell. All experiments were conducted inside a Faraday cage with a thermostatted controller, with a ± 0.2 K temperature error (the highest temperature achieved by the thermosttated controller is 318 K).

5.2.1 Methodology

The system is exposed to a steady flow of pure oxygen gas and voltammograms are recorded periodically, ensuring the RTIL is saturated with the gas. Experimental data will be shown in the Results and discussion section **5.5**. A N_2-saturated experiment was performed by purging pure N_2 into a fresh and dry RTIL sample. All the cyclic voltammetry and potential step transients were performed at the temperatures of 298, 303, 308, 313 and 318 K, and scan rates of 0.1, 0.4 and 1 $V \cdot s^{-1}$.

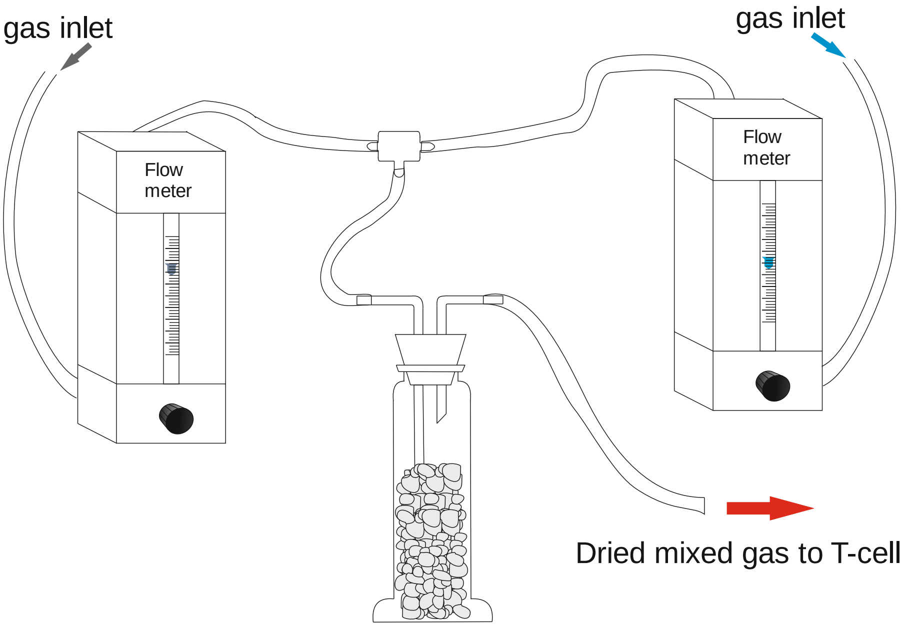

Figure 5.2: Schematic gas mixing equipment

The concentration and diffusion coefficient of O_2 in RTIL $[P_{6,6,6,14}][FAP]$ were determined by chronoamperometric experiments after the solvent is saturated with gas. In chronoamperometry, potential steps are measured from zero current flow (0 V vs. Ag) to a potential where the O_2 reduction reaction is diffusion controlled (typically -1.95 V vs. Ag), but insufficient for solvent reduction.

As explained comprehensively in Chapter 4, section **4.2.2**, equations (4.3) and (4.4), the Shoup and Szabo equation[43] were used to analyse the resultant potential step transients. After fixing the measured value of the electrode radius, 5.7 µm (measured as illustrated in Chapter 3), a range of different *nC* and *D* values were iterated with the Shoup and Szabo expression and compared with experimental transient to retain the 'best fit' value. The 'best fit' value was chosen as it minimised the mean scaled absolute deviation (*MSAD*) which also explained fully in Chapter 4, section **4.2.2** and equation (4.5). Detailed data will be presented in section **5.5**.

5.3 Theory

The modelling in this work was simulated by Dr. Edward O. Barnes. In the following sections experimental voltammetry is considered in light of various possible mechanisms. Ultimately the following mechanism is developed where the reduction via cyclic voltammetry of molecular oxygen is considered to be two successive one-electron processes separated by a fast homogeneous reaction, and the oxidation wave to be a further two-electron process:

$$\mathrm{O_2 + e^- \rightarrow O_2^{\cdot -}} \tag{5.7}$$

$$\mathrm{O_2^{\cdot -} \xrightarrow{fast} X} \tag{5.8}$$

$$\mathrm{X + e^- \rightarrow Y} \tag{5.9}$$

$$\mathrm{Y \rightarrow P + 2e^-} \tag{5.10}$$

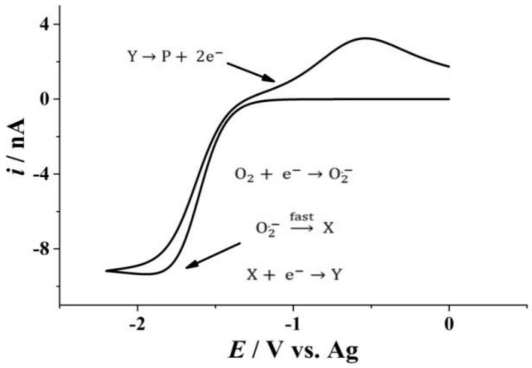

Figure 5.3: Typical reduction and oxidation wave with proposed mechanism at 1 $V \cdot s^{-1}$ scan rate (see text).

Figure 5.3 shows a schematic illustration for the cyclic voltammetry of pure O_2 in $[P_{6,6,6,14}][FAP]$ at 1 $V \cdot s^{-1}$ scan rate with the above mechanism. The reduction waves can be explained by reactions (5.7) – (5.9), and the oxidation wave by the separate two-electron process (5.10). We simplify this complex mechanism by considering simply a two electron processes with differing Butler-Volmer parameters (standard rate constant k^0, formal potential, E_f^o, and transfer coefficients α and β) for the reaction in each direction:

$$\mathrm{A} + 2\mathrm{e}^- \rightarrow \mathrm{Y} \qquad k_1^0, E_{f,1}^o, \alpha_1 \tag{5.11}$$

$$\mathrm{Y} \rightarrow \mathrm{P} + 2\mathrm{e}^- \qquad k_2^0, E_{f,2}^o, \beta_2 \tag{5.12}$$

where A = O_2, and P are products of the reaction. It is possible that P is also O_2. This simplification is a good approximation assuming the homogeneous step is much faster than all other processes, and both transfers are fully electrochemically irreversible. This simplification of the mechanism allows for much more efficient simulation than would be possible by considering the entire mechanism. Since the process takes place in an ionic liquid, migratory mass transport can be neglected due to the suppression of electric fields and only diffusion is considered.[44,45] Fick's second law in cylindrical space is used to model diffusion at a microdisc electrode:

$$\frac{\partial C_i}{\partial \tau} = D_i \left(\frac{\partial^2 c_i}{\partial r^2} + \frac{1}{r} \frac{\partial c_i}{\partial r} + \frac{\partial^2 c_i}{\partial z^2} \right) \tag{5.13}$$

where c_i is the concentration of species i ($mol \cdot m^{-3}$), D_i is the diffusion coefficient of species i ($m^2 \cdot s^{-1}$), r is the radial spatial coordinate (m) and z is the vertical spatial coordinate (m). This equation is normalised by the introduction of dimensionless parameters:

$$\frac{\partial C_i}{\partial \tau} = D_i' \left(\frac{\partial^2 C_i}{\partial R^2} + \frac{1}{R}\frac{\partial C_i}{\partial R} + \frac{\partial^2 C_i}{\partial Z^2} \right) \tag{5.14}$$

where R and Z are dimensionless distances in the r and z directions relative to the electrode radius, r_e (m):

$$R = \frac{r}{r_\mathrm{e}} \tag{5.15}$$

$$Z = \frac{z}{r_\mathrm{e}} \tag{5.16}$$

C_i and D_i' are dimensionless concentrations and diffusion coefficients, which are defined relative to the bulk solution concentration of species A, c_A^* (mol·m^{-3}), and diffusion coefficient of species A:

$$C_\mathrm{i} = \frac{c_\mathrm{i}}{c_\mathrm{A}^*} \tag{5.17}$$

$$D_\mathrm{i}' = \frac{D_\mathrm{i}}{D_\mathrm{A}} \tag{5.18}$$

τ is dimensionless time, defined as:

$$\tau = \frac{D_A}{r_e^2} t \tag{5.19}$$

The conformal mapping technique of Amatore *et al.*[46] is used to map the infinite [0, ∞) x [0, ∞) r,z space onto a finite [0,1] x [0,1] η,Γ space. The coordinate transforms are given by:

$$R = \frac{\sqrt{1-\eta^2}}{cos\left(\frac{\pi}{2}\Gamma\right)} \tag{5.20}$$

$$Z = \eta tan\left(\frac{\pi}{2}\Gamma\right) \tag{5.21}$$

After application of this transformation, the mass transport equation becomes:

$$\frac{\partial C_i}{\partial \tau} = \frac{1}{\eta^2 + tan^2\left(\frac{\pi}{2}\Gamma\right)}\left\{\frac{4}{\pi^2}cos^2\left(\frac{\pi}{2}\Gamma\right)\frac{\partial^2 C_i}{\partial \Gamma^2} + \frac{\partial}{\partial \eta}\left[(1-\eta^2)\frac{\partial C_i}{\partial \eta}\right]\right\} \tag{5.22}$$

This transformation allows the highly curved lines of constant flux present in steady state voltammetry to become straight, allowing for much more efficient solution of the mass transport equation.

The η = 0 axis in transformed space corresponds to the insulating surface surrounding the electrode in real space (R > 1, Z = 0), while η = 0 corresponds to the symmetry axis at the centre of the electrode (R = 0, all Z). The Γ = 1 boundary corresponds to bulk solution. At all three of these boundaries, a zero flux condition is imposed on all species.

The Γ = 0 boundary corresponds to the electrode surface, and Butler-Volmer kinetics are applied.[47,48] In transformed space, and assuming each independent electron transfer is fully irreversible:

$$\left(\frac{\partial C_A}{\partial \Gamma}\right)_{\Gamma=0} = \left[K_1^0 C_A^0 e^{-\alpha_1(\theta-\theta_{f,1})} - K_2^0 C_B^0 e^{\beta_2(\theta-\theta_{f,2})}\right] \tag{5.23}$$

where a subscript 1 corresponds to the reductive electron transfer, and a subscript 2 to the oxidative electron transfer. K^0 is the dimensionless standard electrochemical rate constant, given by:

$$K^0 = \frac{r_e}{D_A} k^0 \tag{5.24}$$

and k^0 is the standard electrochemical rate constant (m·s^{-1}). C_A^0 and C_B^0 are dimensionless concentrations as defined above adjacent to the surface, and α_1 and β_2 are transfer constants[49,50] for the reduction and oxidation process, respectively. θ and θ_f are the dimensionless applied potential and formal potential. Dimensionless potentials are defined as:

$$\theta = \frac{F}{RT} E \tag{5.25}$$

In cyclic voltammetry, the applied potential θ is swept linearly from some start potential to a vertex potential, and then back again. The mathematical form of the potential profile for a reduction is given by:

$$\theta = |\theta_s - \theta_v - \sigma\tau| + \theta_v \tag{5.26}$$

where σ is the dimensionless scan rate, given by:

$$\sigma = \frac{F r_e^2}{R T D_A} \nu \tag{5.27}$$

The dimensional current is then calculated as:

$$I = 2\pi n F D_A C_A^* r_e \int_0^1 \eta \left(\frac{\partial C_A}{\partial \Gamma}\right)_{\Gamma=0} d\eta \tag{5.28}$$

5.3.1 Numerical Methods

The modelling programme used in this work was kindly developed by Dr. Edward O. Barnes.

To obtain a solution to the cyclic voltammetry problem, the mass transport equations and boundary conditions are discretised using the finite difference method,[51] and solved numerically over discrete temporal and spatial grids. Both grids are regular, with a constant interval between successive points. The temporal grid is defined using N_θ, the number of grid points per unit θ swept put. The spatial grid has N points in each direction η and Γ. Convergence studies found $N_\theta = 50$ and $N = 100$ sufficient to provide results within 0.5 % of a fully converged result.

The discretised mass transport equation and boundary conditions were solved in matrix form using the Thomas algorithm[52] and the alternating direction implicit (ADI) method,[53] allowing parallel programming to be employed to decrease simulation times. The program was coded in C++. All simulations were carried out on a 3.40 GHz Intel (R) Core (TM) i5-3570 CPU with 4.00 GB RAM. Typical running times were ca. three minutes per simulation.

5.4 Results and Discussion

In the following section, we present chronoamperometry and cyclic voltammetry experimental data for the reduction of pure O_2, and then simulate the cyclic voltammetry with the two-electron process model described in the Theory section. We then further validate the proposed mechanism by performing cyclic voltammetry on O_2 in the presence of CO_2, which results in an approximate halving of the reductive current due to the chemical trapping of superoxide before the second electron transfer.[5,23,54-64]

5.4.1 Chronoamperometric Experiments

Chronoamperometric measurements were performed at each temperature and partial pressure studied. The current time transient from the chronoamperometry is used then to determine the concentration and diffusion coefficient of O_2. As outlined in the Methodology section **5.3.1**, the potential was stepped from 0 to -1.95 V vs. Ag on a Pt microelectrode to deduce the value nc of concentration c, multiplied by the number of electrons transferred, n, and the diffusion coefficient D of oxygen in the RTIL using the Shoup and Szabo equation. **Figure 5.4** shows three chronoamperometric measurements carried out after exposure to O_2 for 30, 60, 120 and 135 minutes. It is seen that steady state current still increased after 30 minutes and all three transient after 60 minutes overlay very well and gave the similar nc and D values of 5.25 ± 0.13 mM and $7.05 \pm 0.1 \times 10^{-10}$ $m^2 \cdot s^{-1}$, respectively. These demonstrate that O_2 saturation is reached after 60 minutes and a period of 15 minutes between potential step experiments is long enough to allow full relaxation of the concentration local to the microelectrode to relax to the bulk value after perturbation, and that longer times than this had no effect on the chronoamperometry. A typical MSAD contour plot was made as illustrated in Chapter 4, section **4.3.3** and is shown in **Figure 5.5**. The minimum MSAD appeared where $nc = 5.25$ $mmol \cdot L^{-1}$, and $D = 7.05 \times 10^{-10}$ $m^2 \cdot s^{-1}$, respectively. Shoup and Szabo fitting of the transient can be seen in **Figure 5.6a**.

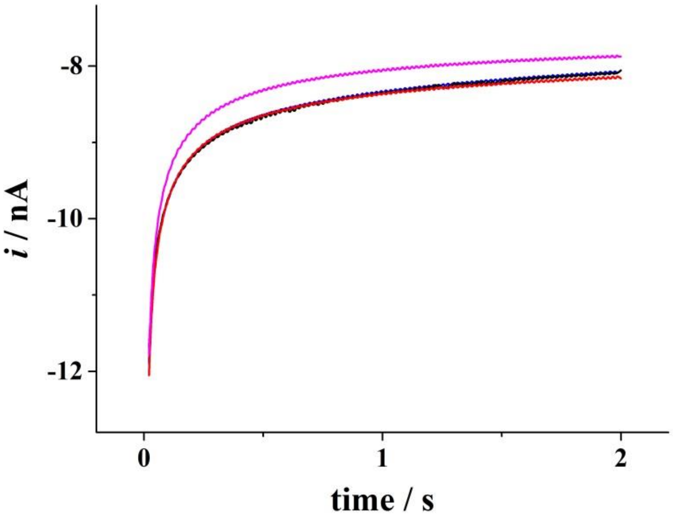

Figure 5.4: Three chronoamperometric measurements recorded after exposure to O_2 for 30 (▬), 60 (▬), 120 (▬) and 135 (▬) minutes.

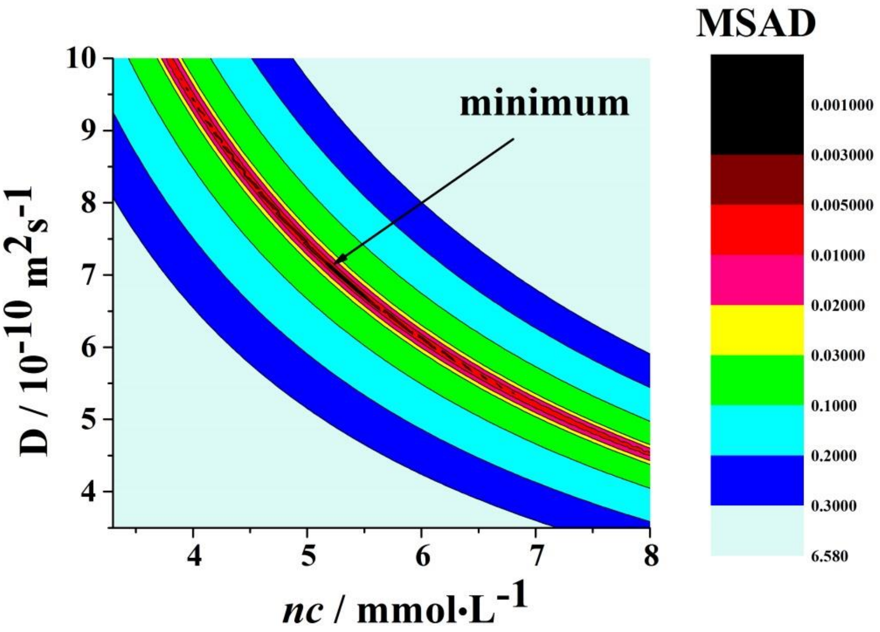

Figure 5.5: 2D contour plot of MSAD where the colour corresponding to the MSAD is listed to the right. The result was obtained from the reduction of O_2 in $[P_{6,6,6,14}][FAP]$ after exposure to O_2 for 120 minutes.

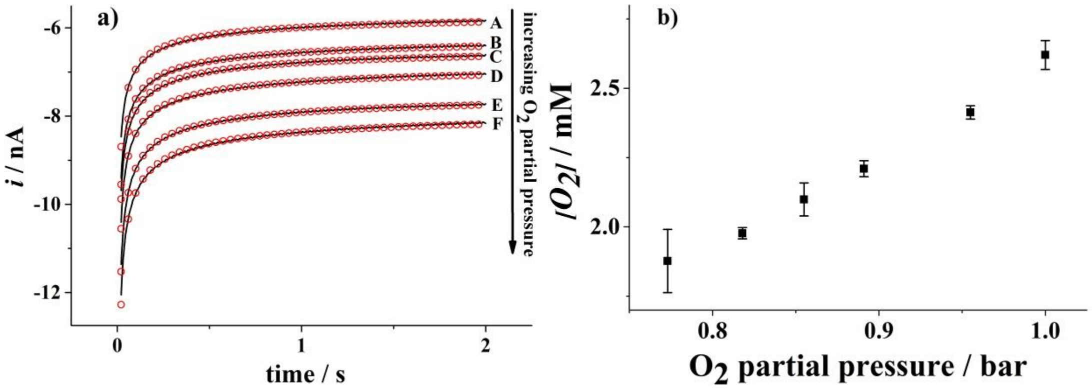

Figure 5.6: a) Experimental (▬) and simulated (○) transients for the reduction of (A) 0.77, (B) 0.82, (C) 0.86, (D) 0.89, (E) 0.96, and (F) 1 bar pressure of O_2. The remainder was N_2, maintaining the total pressure to be 1 bar. $T = 298$ K. The potential was stepped from 0 to -1.98 ± 0.4 V vs. Ag in all measurements. b): O_2 concentration (assume $n = 2$) variation with the partial pressure of O_2 in the gas mixture.

Transients were recorded for 100% pure O_2 and each of five different partial pressures of O_2, namely 0.77, 0.82, 0.86, 0.89 and 0.96 bar. **Figure 5.6** compares the experimental and fitted transients in the O_2/RTIL and O_2/N_2/RTIL systems. Excellent agreement between experimental and Shoup and Szabo transient can be seen. Here we assume that $n = 2$ for the reasons discussed later in the chapter. The inset shows that the equilibrium between O_2 gas phase and solution phase has been achieved and the concentration of O_2 is directly proportional to the partial pressure of O_2 in the T-cell, in accordance with the Henry's Law:[65]

$$p = K_H c \tag{5.29}$$

where p is the partial pressure of O_2 above the solution, c is the concentration of O_2 (determined from nc value where $n = 2$, for the reasons to be discussed below) and

K_H is Henry's Law constant which equals 396 L·bar·mol^{-1}. We obtained a value of *nc* from 3.75 ± 0.22 mM at the lowest pressure to 5.25 ± 0.13 mM at the highest pressure from the fitting, whereas the diffusion coefficient remained 7.0 ± 0.2× 10^{-10} m^2·s^{-1}, suggesting the validity of the fitting as the diffusion coefficient is not expected to be a function of O_2 partial pressure in dilute solution. The O_2 concentration *nc* and diffusion coefficient *D* deduced from the Shoup and Szabo equation are compared with literature values in **Table 5.4** which shows that both the *c* and the *D* are similar to literature values measured in other ionic liquids.

Table 5.4: Comparison with literature of the product *nc* and the diffusion coefficient for O_2 in [$P_{6,6,6,14}$][FAP] and other oxygen solubility data. Note that as described in the text, *n* = 2 for [$P_{6,6,6,14}$][FAP].

Ionic liquids	***nc*(O_2) / mM**	***D*(O_2) / 10^{-10} m^2·s^{-1}**	**Likely *n***
[$P_{6,6,6,14}$][FAP][a]	5.25 ± 0.13	7.05 ± 0.1	2
[C_2mim][NTf_2][66]	3.9	7.3 ± 1.0	1
[C_4dmim][NTf_2][7]	3.6	5.1	1
[C_4mim][BF_4][7]	4.1	1.8	1
[C_4mim][NTf_2][7]	3.1	8.8	1
[C_4mim][PF_6][14]	3.6	2.2	1
[C_4mim][PF_6][7]	3.0	2.5	1
[C_4mpyrr][NTf_2][7]	3.6	5.5	1
[$N_{6,2,2,2}$][NTf_2][3]	8.9 ± 0.8	3.2 ± 0.3	1
[$N_{6,2,2,2}$][NTf_2][7]	3.9	4.6	1
[$N_{6,2,2,2}$][NTf_2][66]	11.6	1.5 ± 0.2	1
[Py_{14}][NTf_2][3]	6.1 ± 0.8	5.2 ± 0.4	1
[$P_{6,6,6,14}$][FAP][3]	7.8 ± 1.5	6.1 ± 1.1	1
[$P_{6,6,6,14}$][NTf_2][3]	6.0 ± 0.5	7.5 ± 0.6	1
[$P_{6,6,6,14}$][NTf_2][11]	4.0 ± 0.1	7.5 ± 0.1	1

[a]Values deduced in this Chapter

Chronoamperometric experiments were carried out at different temperatures to find out the dependence on temperature of the concentration and diffusion coefficient of O_2. **Figure 5.7** shows excellent agreement between experimental transient and Shoup and Szabo fittings at 298, 303, 308, 313, and 318 K. **Figure 5.8a** illustrates a linear dependence for the natural logarithm of the O_2 concentration c (assuming n = 2) on the reciprocal of absolute temperature, in line with the Van't Hoff equation:[67]

$$\ln c = \frac{-\Delta H}{RT} + constant \tag{5.30}$$

where c is O_2 concentration; ΔH is the enthalpy of dissolution; R is the ideal gas constant; and T is temperature. The ΔH of O_2 solubility was calculated to be + 5.7 kJ·mol^{-1} from **Figure 5.8a.** The likely positive enthalpy of oxygen dissolution in [$P_{6,6,6,14}$][FAP] corresponds to an endothermic dissolution in this particular system. **Table 5.5** compares ΔH from our work with literature values for O_2 dissolution in various ionic liquids. The reported enthalpies of O_2 dissolution vary significantly in different ionic liquids, from - 29.2 to + 20.6 kJ·mol^{-1}.

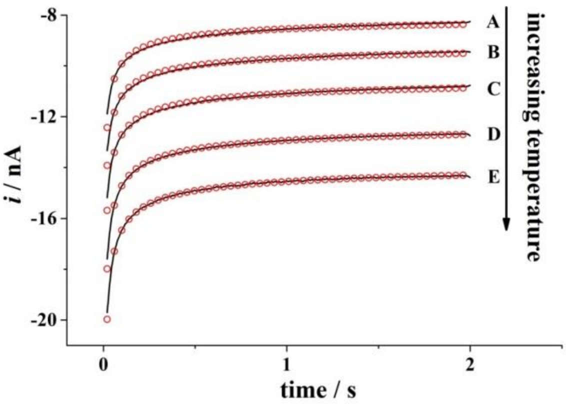

Figure 5.7: Experimental (▬) and simulated (○) chronoamperometric transients for the reduction of O_2 at (A) 298 K, (B) 303 K, (C) 308 K, (D) 313 K, and (E) 318 K, with the 100% O_2 gas at 1 bar pressure.

Note that in gas solubility measurement of the type reported in this chapter, the *ΔH* values for O_2 solubility are differential enthalpies of solubility pertaining to gas saturation, which is the rate of the change of enthalpy ΔH with the increase of n_{O2}, as described in Chapter 4, equation (4.10). These, in principle, can be quite different (even to the extent of differing in sign) from the corresponding molar integral values, as described in Chapter 4, equation (4.11).

Table 5.5: Comparison of *ΔH* and E_a value of our work with literature values

Ionic liquid	**ΔH/kJ·mol^{-1}**	**E_a/kJ·mol^{-1}**
[C_4mim][NTf_2]	20.6 ± 8.2[68]	21.5[7]
[C_4mpyrr][NTf_2]	-	22.5[7]
[C_4dmim][NTf_2]	-	23.5[7]
[C_4mim][BF_4]	-	27.9[7]
[C_4mim][PF_6]	-	33.2[7]
[C_4mim][$CF_3CF_2CF_2COO$]	-2.67[69]	-
[dema][TfO]	-	23.0[70]
[MeBuPyrr][NTf_2]	13.1 ± 12.5[68]	
[$(MeOEt)_2NH$][C_6H_5COOH]	-29.2[70]	45.0[70]
[$N_{6,2,2,2}$][NTf_2]	-	20.2[7]
[$P_{6,6,6,14}$][FAP][a]	5.73	16.1

[a]value from our work

The Arrhenius behaviour of diffusion of O_2 in [$P_{6,6,6,14}$][FAP] is shown in **Figure 5.8b**. A linear dependence of the natural logarithm of the O_2 diffusion coefficient *D* with the reciprocal of the absolute temperature can be seen.[67] The activation energy E_a of O_2 diffusion was calculated to be + 16.1 kJ·mol^{-1} from **Figure 5.8b** using the Arrhenius equation:

$$\ln(D) = \frac{-E_a}{R}\frac{1}{T} + \ln(A) \tag{5.31}$$

where $A = 2.66 \times 10^{-7}$ $m^2 \cdot s^{-1}$, is determined from the y axis intercept. **Table 5.5** compares E_a from this work and the literature values in other RTILs. The value of E_a here determined is found to be lower than that reported in other RTILs, consistent with the relatively large value of D_{O2} determined for [$P_{6,6,6,14}$][FAP]. (**Table 5.4**)

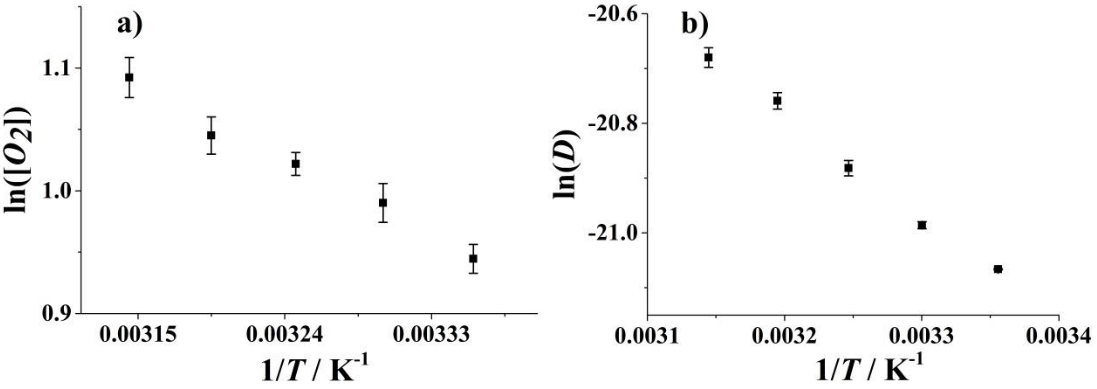

Figure 5.8: Temperature dependence of O_2 concentration (a) and diffusion coefficient (b), assuming $n = 2$. Experiments were carried out with the 100% pure O_2 gas at 1 bar pressure.

5.4.2 Cyclic Voltammetry Measurements

In this section, we report the cyclic voltammetry of pure O_2 in the RTIL [$P_{6,6,6,14}$][FAP]. We simulate this voltammetry using the mechanism described in the Theory section of two separate two-electron transfers. The suggestion of the two-electron nature of the reduction is then supported by carrying out cyclic voltammetry of O_2 in the presence of CO_2, which traps the superoxide after a single electron transfer,[5,23,54-64] resulting in an approximate halving of the reductive current.

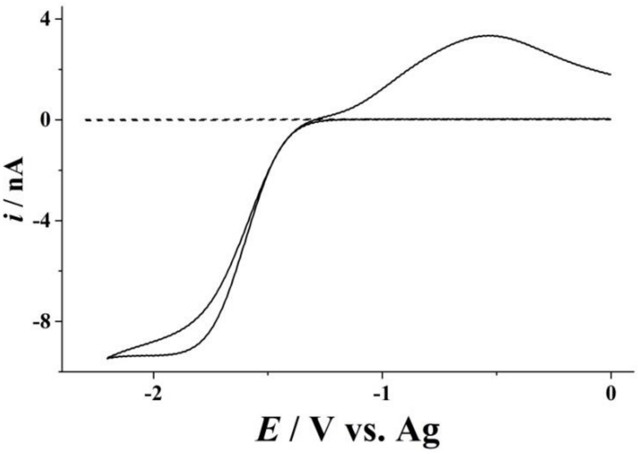

Figure 5.9: Comparison of cyclic voltammogram for N_2-saturated (--) and O_2-saturated (▬) [$P_{6,6,6,14}$][FAP] at a 5.7 µm Pt microelectrode, 1 V·s^{-1} scan rate, 298 K.

First, cyclic voltammetry of [$P_{6,6,6,14}$][FAP] was conducted in the absence of O_2 to ensure the purity and dry condition of RTIL. Only N_2 was purged during the voltammetry measurement. The RTIL saturated with the N_2 system only shows small background currents flowing in the potential range 0 to -2.2 V vs. Ag (see the dashed line in **Figure 5.9**). After the N_2 gas flow was stopped, O_2 was subsequently purged into the cell to investigate the reduction process. The same potential range of 0 to -2.2 V vs. Ag was used to study the O_2 reduction. **Figure 5.9** also shows the cyclic voltammogram of oxygen saturated [$P_{6,6,6,14}$][FAP]. Clear voltammetric waves were seen in the IL after purging with O_2 for 30 minutes. The reduction of O_2 in the RTIL is associated with the peak at ca. – 1.90 V vs. Ag; an oxidative peak at ca. -0.6 V vs. Ag is also observed. Similar experiments were conducted at the different scan rates of 800 mV·s^{-1}, 400 mV·s^{-1} and 100 mV·s^{-1} and are shown as solid lines in **Figure 5.10** along with fitted data. The latter is described below.

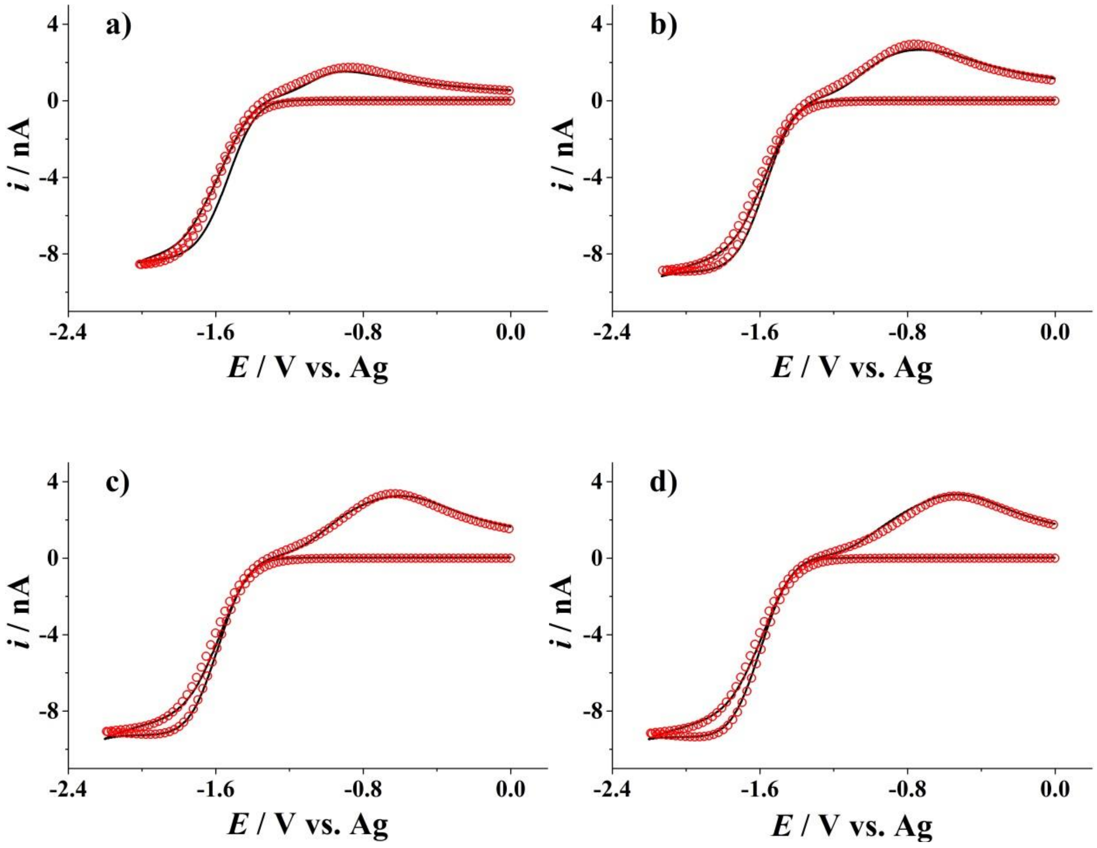

Figure 5.10. Experimental (▬) and simulated (○) cyclic voltammetry of pure & dry O_2 in $[P_{6,6,6,14}][FAP]$ at a 5.7 µm radius Pt disc electrode at a scan rate of (a) 100 $mV \cdot s^{-1}$, (b) 400 $mV \cdot s^{-1}$, (c) 800 $mV \cdot s^{-1}$, and (d) 1 $V \cdot s^{-1}$ at 298 K.

5.4.3 Simulation of Experimental Voltammograms

Computer modelling was used to examine the possible applicability of the mechanism proposed in the Theory section **5.4**. First, a one-electron mechanism was used to fit the voltammetry, but it was not possible to fit the voltammogram with $\alpha_1 + \beta_2 = 1$. The Tafel equation was used in order to find values of transfer coefficient α_1 and β_2. For an irreversible reduction, the Tafel equation is given by:[71]

$$\ln(I) = \frac{-\alpha}{RT} E + constant \tag{5.32}$$

and for an oxidation is given by:

$$\ln(I) = \frac{\beta}{RT}E \ + constant' \tag{5.33}$$

Therefore, a plot of ln(I) against E for data at the base of a voltammetric wave will yield a straight line of gradient $\frac{-\alpha}{RT}$ for a reduction and $\frac{\beta}{RT}$ for an oxidation. Using this method, α_1 and β_2 were found to be 0.28 and 0.16 ± 0.01, respectively. The failure of these values to sum to 1 is a confirmation of the reductive and oxidative waves relating to separate redox processes.[49,50]

Further evidence that a one-electron mechanism is inappropriate is that the forward peak current approximately halved when carbon dioxide was introduced into the system, indicating that two electrons were transferred in the forward process (see below). A different mechanism with a two-electron transfer forward process and a one-electron transferred backward process was examined next, but the simulated back peak only reached half of the experimental data. Therefore, both forward and backward processes were simulated as two-electron transfers (as discussed in section **5.4** above), which fitted very well with the experimental voltammetry. **Figure 5.10** shows the cyclic voltammetric response for pure O_2 in [$P_{6,6,6,14}$][FAP] over different scan rates at 298 K. The forward peak and back peak were simulated using the following mechanism:

$$\mathrm{A} + 2\mathrm{e}^- \rightarrow \mathrm{Y} \qquad k_1^0, E_{f,1}^o, \alpha_1 \tag{5.14}$$

$$\mathrm{Y} \rightarrow \mathrm{P} + 2\mathrm{e}^- \qquad k_2^0, E_{f,2}^o, \beta_2 \tag{5.15}$$

which show an excellent fit between the experimental and simulated data. Parameters used in the modelling programme are listed in **Table 5.6**, where c is the concentration of O_2 in the RTIL, as determined from chronoamperometric study with $n = 2$, D_{O2} is the O_2 diffusion coefficient (A in equation (5.11)), D_Y is the diffusion coefficient of Y, k_1^0 and k_2^0 are the heterogeneous rate constant for the forward and backward reaction, $E_{f,1}^o$ and $E_{f,2}^o$ are formal potentials for the forward and backward reaction, α_1 and β_2 are transfer constants for the reduction and oxidation process, respectively.

Table 5.6. Parameters used to simulate the voltammograms of pure and dry O_2 in $[P_{6,6,6,14}][FAP]$ at the Pt microdisc electrode at 298 K.

c (mM)	2.65
D_{O2} (10^{-10} $m^2 \cdot s^{-1}$)	7.10
D_Y (10^{-12} $m^2 \cdot s^{-1}$)	1.50
$k_1^0 \exp(\frac{\alpha_1 E_{f,1}^o}{RT})$ (10^{-8} $m^2 \cdot s^{-1}$)	1.00
$k_2^0 exp(-\frac{\beta_2 E_{f,2}^o}{RT})$ (10^{-9} $m^2 \cdot s^{-1}$)	1.80
α	0.28
β	0.16 ± 0.01

Note the α_1 and β_2 values calculated from the Tafel analysis of experimental data discussed above were employed in the simulation. As the waves are fully irreversible, only the compound parameters $k_1^0 \exp(\frac{\alpha_1 E_{f,1}^o}{RT})$ and $k_2^0 \exp(-\frac{\beta_2 E_{f,2}^o}{RT})$ can be reported, rather than the k_0 and E_f^o values separately. The c and D_{O2} values were obtained from the Shoup and Szabo equation. As nc was found to be 5.30 mM, and we assume $n = 2$, a value of $c = 2.65$ mM was used.

5.4.4 Voltammograms of Oxygen in the presence of Carbon Dioxide

In order to validate the two-electron transfer mechanism, we next mixed carbon dioxide (CO_2) into the system to trap the superoxide ion $O_2^{\cdot -}$ as a likely intermediate in the two-electron reduction. The chemical reaction between CO_2 and superoxide has been investigated by several groups indicating the chemical trapping of superoxide by CO_2 in a wide variety of solvents.[23,54-57,59,72-74] O_2 and CO_2 were mixed by flow meters as described in the Experimental Section and purged into the T-cell. Cyclic voltammograms were recorded at 0, 0.014, 0.045, 0.082 and 0.22 bar CO_2 partial pressures to test the interaction between CO_2 and the electroactive species. **Figure 5.11** shows the cyclic voltammetry of O_2 in the presence of various CO_2 contents. It can be seen that the peak current decreased with increasing CO_2 content. The reductive current falls approximately by a factor of 2 as the CO_2 concentration increases to above 0.08 bar, suggesting that the O_2 reduction process is overall a two-electron step and consistent with the notion that CO_2 traps the superoxide anion, $O_2^{\cdot -}$. The trapping also leads to the disappearance of the back peak due to reoxidation. The voltammetry of the mixed gases is therefore consistent with and supportive of the proposed two-electron reduction process. The inset of **Figure 5.11** shows the dependence of reduction peak current divided by O_2 partial pressure against CO_2 partial pressure. The halving of peak current can be seen clearly, but a slight increase of peak current above 0.08 bar CO_2 partial pressure is discovered. This may be due to the reduction of RTIL's viscosity and subsequently changed the O_2 diffusion coefficient after the introduction of CO_2, as reported previously.[75]

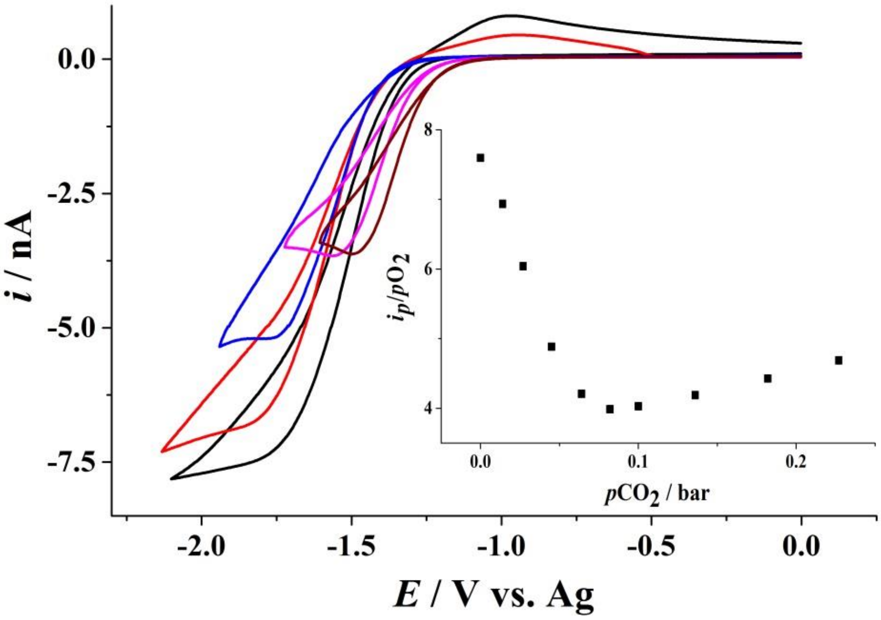

Figure 5.11: Cyclic voltammetric response of mixed O_2 and CO_2 gas with 0 bar(▬), 0.014 bar (▬), 0.045 bar (▬), 0.082 bar (▬) and 0.22 bar (▬) CO_2 in the mixture at 298 K. The reminder was made up of O_2 to keep the overall pressure to be 1 bar. Scan rate: 25 mV·s^{-1}.

A possible overall mechanism is proposed below:

$$O_2 + e^- \rightarrow O_2^{\cdot -} \tag{5.34}$$

$$O_2^{\cdot -} + CO_2 \rightarrow Z \tag{5.35}$$

$$O_2^{\cdot -} \rightarrow X \tag{5.36}$$

$$X + e^- \rightarrow Y \tag{5.37}$$

$$Y \rightarrow P + 2e^- \tag{5.38}$$

It is likely but not essential that P = O_2. Previous literature suggesting the abstraction of a proton by $O_2^{\cdot -}$ from the $[P_{6,6,6,14}]^+$ cation make it likely that species X is $HO_2^{\cdot}$ [3,16] which is then reduced to $HO_2^{\cdot -}$ (species Y). Due to the chemical trapping of $O_2^{\cdot -}$, the second electron transfer and reoxidation process will gradually disappear with the increasing amount of dissolved CO_2 contents.

Meanwhile, as shown in **Figure 5.9**, the linear behaviour shows that low concentration of CO_2 can be accurately detected in the mixture when the majority of the mixture is O_2. The potential application for medical sensing is evident.

5.5 Conclusions

The reduction of O_2 in RTIL [$P_{6,6,6,14}$][FAP] was performed over different partial pressures and temperatures. The solubility and diffusion coefficient of O_2 were determined using the Shoup and Szabo equation fitted to experimental chronoamperometry. In this system, O_2 is reduced into the reactive intermediate $O_2^{\cdot -}$ which can be further reduced to the product. The product can then undergo a separate two-electron oxidation process. With the introduction of CO_2, the reactive intermediate $O_2^{\cdot -}$ can be trapped by reaction with CO_2 as observed in other solvents,[23,54-62] and a full mechanistic scheme is given in equations (5.34) – (5.38). Linear relationship between reductive current and O_2/CO_2 partial pressure was discovered at high O_2 concentration, indicating the potential of this RTIL to be developed into an O_2/CO_2 dual sensor which can be applied for various applications including medical treatment and spacecraft O_2 sensing where the gas mixtures have high O_2 content.

References

(1) Li, P.; Barnes, E. O.; Hardacre, C.; Compton, R. G. *J. Phys. Chem. C* **2015**, *119*, 2716.

(2) Li, P.; Compton, R. G. *Electroanalysis* **2015**, Ahead of Print.

(3) Evans, R. G.; Klymenko, O. V.; Saddoughi, S. A.; Hardacre, C.; Compton, R. G. *J. Phys. Chem. B* **2004**, *108*, 7878.

(4) Sawyer, D. T.; Chiericato, G., Jr.; Angelis, C. T.; Nanni, E. J., Jr.; Tsuchiya, T. *Anal. Chem.* **1982**, *54*, 1720.

(5) Wadhawan, J. D.; Welford, P. J.; McPeak, H. B.; Hahn, C. E. W.; Compton, R. G. *Sens. Actuators, B* **2003**, *88*, 40.

(6) Vasudevan, D.; Wendt, H. *J. Electroanal. Chem.* **1995**, *392*, 69.

(7) Huang, X.-J.; Rogers, E. I.; Hardacre, C.; Compton, R. G. *J. Phys. Chem. B* **2009**, *113*, 8953.

(8) Pozo-Gonzalo, C.; Torriero, A. A. J.; Forsyth, M.; MacFarlane, D. R.; Howlett, P. C. *J. Phys. Chem. Lett.* **2013**, *4,* 1834.

(9) Pozo-Gonzalo, C.; Howlett, P. C.; Hodgson, J. L.; Madsen, L. A.; MacFarlane, D. R.; Forsyth, M. *Phys. Chem. Chem. Phys. : PCCP* **2014**.

(10) Hayyan, M.; Mjalli, F. S.; Hashim, M. A.; AlNashef, I. M.; Al-Zahrani, S. M.; Chooi, K. L. *J. of Electroanal. Chem.* **2012**, *664*, 26.

(11) Xiong, L.; Barnes, E. O.; Compton, R. G. *Sens. Actuators, B: Chemical* **2014**, *200*, 157.

(12) Pozo-Gonzalo, C.; Virgilio, C.; Yan, Y.; Howlett, P. C.; Byrne, N.; MacFarlane, D. R.; Forsyth, M. *Electrochem. Commun.* **2014**, *38*, 24.

(13) Katayama, Y.; Onodera, H.; Yamagata, M.; Miura, T. *J. Electrochem. Soc.* **2004**, *151*, A59.

(14) AlNashef, I. M.; Leonard, M. L.; Kittle, M. C.; Matthews, M. A.; Weidner, J. W. *Electrochem. Solid-State Lett.* **2001**, *4*, D16.

(15) Hayyan, M.; Mjalli, F. S.; Hashim, M. A.; AlNashef, I. M.; Tan, X. M. *J. Electroanal. Chem.* **2011**, *657*, 150.

(16) Hayyan, M.; Mjalli, F. S.; AlNashef, I. M.; Hashim, M. A. *J. Fluorine Chem.* **2012**, *142*, 83.

(17) Andrieux, C. P.; Hapiot, P.; Savéant, J. M. *J. Am. Chem. Soc.* **1987**, *109*, 3768.

(18) Amatore, C.; Saveant, J. M. *J. Electroanal. Chem. Interfacial Electrochem.* **1978**, *86*, 227.

(19) Li, P.; Henstridge, M. C.; Xiong, L.; Compton, R. G. *Electroanalysis* **2013**, *25*, 2268.

(20) Silvester, D. S.; Rogers, E. I.; Barrosse-Antle, L. E.; Broder, T. L.; Compton, R. G. *J. Braz. Chem. Soc.* **2008**, *19*, 611.

(21) Silvester, D. S.; Compton, R. G. *Z. Phys. Chem.* **2006**, *220*, 1247.

(22) Barrosse-Antle, L. E.; Bond, A. M.; Compton, R. G.; O'Mahony, A. M.; Rogers, E. I.; Silvester, D. S. *Chem. - Asian J.* **2010**, *5*, 202.

(23) Buzzeo, M. C.; Klymenko, O. V.; Wadhawan, J. D.; Hardacre, C.; Seddon, K. R.; Compton, R. G. *J. Phys. Chem. B* **2004**, *108*, 3947.

(24) Lee, J.; Murugappan, K.; Arrigan, D. W. M.; Silvester, D. S. *Electrochimica Acta* **2013**, *101*, 158.

(25) Baltes, N.; Beyle, F.; Freiner, S.; Geier, F.; Joos, M.; Pinkwart, K.; Rabenecker, P. *Talanta* **2013**, *116*, 474.

(26) Hayyan, M.; Mjalli, F. S.; Hashim, M. A.; AlNashef, I. M.; Tan, X. M.; Chooi, K. L. *J. Applied. Sci.* **2010**, *10*.

(27) Amao, Y. *Microchim. Acta* **2003**, *143*, 1.

(28) Grist, S. M.; Chrostowski, L.; Cheung, K. C. *Sensors* **2010**, *10*, 9286.

(29) Kuang, X.; Payne, J. L.; Johnson, M. R.; Radosavljevic Evans, I. *Angew. Chem., Int. Ed.* **2012**, *51*, 690.

(30) McDonagh, C.; Burke, C. S.; MacCraith, B. D. *Chem. Rev.* **2008**, *108*, 400.

(31) Mills, A. *Platinum Met. Rev.* **1997**, *41*, 115.

(32) Rahman, M. A.; Kumar, P.; Park, D.-S.; Shim, Y.-B. *Sensors* **2008**, *8*, 118.

(33) Wang, X.-D.; Chen, H.-X.; Zhao, Y.; Chen, X.; Wang, X.-R.; Chen, X. *TrAC, Trends Anal. Chem.* **2010**, *29*, 319.

(34) Ayers, M. R.; Hunt, A. J.; The Regents of the University of California, USA . 1999, p 14 pp.

(35) Chu, C.-S.; Lin, C.-A. *Sens. Actuators, B* **2014**, *195*, 259.

(36) Liu, H.; Yang, H.; Hao, X.; Xu, H.; Lv, Y.; Xiao, D.; Wang, H.; Tian, Z. *Small* **2013**, *9*, 2639.

(37) O'Driscoll, B. R.; Howard, L. S.; Davison, A. G. *Thorax* **2008**, *63*, vi1.

(38) Shehata, N.; Meehan, K.; Leber, D. *Proc. SPIE* **2012**, *8463*, 84630P/1.

(39) Sung, T.-W.; Lo, Y.-L. *Sens. Actuators, B* **2012**, *173*, 406.

(40) Lee, Y. E. K.; Kopelman, R. *Methods in Enzymology*; Academic Press: San Diego, 2012; Vol. 504.

(41) Devor, A.; Sakadzic, S.; Srinivasan, V. J.; Yaseen, M. A.; Nizar, K.; Saisan, P. A.; Tian, P.; Dale, A. M.; Vinogradov, S. A.; Franceschini, M. A.; Boas, D. A. *J Cereb Blood Flow Metab* **2012**, *32*, 1259.

(42) Cortright, E. M. *Apollo Expeditions to the Moon*; U.S. Government Printing Office: Washington, DC, 1975.

(43) Shoup, D.; Szabo, A. *J. Electroanal. Chem. Interfacial Electrochem.* **1982**, *140*, 237.

(44) Dickinson, E. J. F.; Compton, R. G. *J. of Electroanal. Chem.* **2011**, *661*, 198.

(45) Dickinson, E. J. F.; Limon-Petersen, J. G.; Rees, N. V.; Compton, R. G. *J. Phys. Chem. C* **2009**, *113*, 11157.

(46) Amatore, C. A.; Fosset, B. *J. Electroanal. Chem.* **1992**, *328*, 21.

(47) Butler, J. A. V. *Trans. Faraday Soc.* **1924**, *19*, 729.

(48) Erdey-Gruz, T.; Volmer, M. *Z. physik. Chem.* **1930**, *150*, 203.

(49) Guidelli, R.; Compton, R. G.; Feliu, J. M.; Gileadi, E.; Lipkowski, J.; Schmickler, W.; Trasatti, S. *Pure Appl. Chem.* **2014**, *86*, 245.

(50) Guidelli, R.; Compton, R. G.; Feliu, J. M.; Gileadi, E.; Lipkowski, J.; Schmickler, W.; Trasatti, S. *Pure Appl. Chem.* **2014**, *86*, 259.

(51) Compton, R. G.; Laborda, E.; Ward, K. R. *Understanding Voltammetry: Simulation of Electrode Processes*; Imperial College Press: London, 2014.

(52) Press, W. H.; Teukolsky, S. A.; Vetterling, W. T.; Flannery, B. P. *Numerical Recipes: The Art of Scientific Computing*; 3rd Edition ed.; Cambridge University Press, 2007.

(53) Britz, D. *Digital Simulation in Electrochemistry*; Springer-Verlag: Heidelberg, 2005.

(54) Wadhawan, J. D.; Welford, P. J.; Maisonhaute, E.; Climent, V.; Lawrence, N. S.; Compton, R. G.; McPeak, H. B.; Hahn, C. E. W. *J. Phys. Chem. B* **2001**, *105*, 10659.

(55) Albery, W. J.; Clark, D.; Drummond, H. J. J.; Coombs, A. J. M.; Young, W. K.; Hahn, C. E. W. *J. Electroanal. Chem.* **1992**, *340*, 99.

(56) Hahn, C. E. W.; McPeak, H.; Bond, A. M. *J. Electroanal. Chem.* **1995**, *393*, 69.

(57) Hahn, C. E. W.; McPeak, H.; Bond, A. M.; Clark, D. *J. Electroanal. Chem.* **1995**, *393*, 61.

(58) McPeak, H.; Bond, A. M.; Hahn, C. E. W. *J. Electroanal. Chem.* **2000**, *487*, 25.

(59) Roberts, J. L., Jr.; Calderwood, T. S.; Sawyer, D. T. *J. Am. Chem. Soc.* **1984**, *106*, 4667.

(60) Qian, F.; Lu, J.; Zhou, Z.; Cha, C. *Sens. Actuators, B* **1993**, *17*, 77.

(61) Zhou, Z.-B.; Liu, W.-J.; Liu, C.-C. *Sens. Actuators, B* **1998**, *52*, 219.

(62) Zhou, Z. B.; Liu, W. J.; Liu, C. C. *Sens. Actuators, B* **2000**, *65*, 35.

(63) Casadei, M. A. *Eur. J. Org. Chem.* **2001**, 1689.

(64) Casadei, M. A.; Cesa, S.; Moracci, F. M.; Inesi, A.; Feroci, M. *J. Org. Chem.* **1996**, *61*, 380.

(65) Battino, R.; Cleve, H. L. *Chem. Rev.* **1966**, *66*, 395.

(66) Buzzeo, M. C.; Klymenko, O. V.; Wadhawan, J. D.; Hardacre, C.; Seddon, K. R.; Compton, R. G. *J. Phys. Chem. A* **2003**, *107*, 8872.

(67) Atkins, P.; Paula, J. D. *Physical Chemistry*; W.H. Freeman & Company, 2009.

(68) Anthony, J. L.; Anderson, J. L.; Maginn, E. J.; Brennecke, J. F. *J. Phys. Chem. B* **2005**, *109*, 6366.

(69) Zhou, L.; Fan, J.; Shang, X.; Wang, J. *J. Chem. Thermodyn.* **2013**, *59*, 28.

(70) Khan, A.; Lu, X.; Aldous, L.; Zhao, C. *J. Phys. Chem. C* **2013**, *117*, 18334.

(71) Compton, R. G.; Banks, C. E. *Understanding Voltammetry*; 2nd Edition ed.; Imperial College Press, 2010.

(72) Xiao, C.; Zeng, X. *J. Electrochem. Soc.* **2013**, *160*, H749.

(73) Feroci, M.; Chiarotto, I.; Orsini, M.; Sotgiu, G.; Inesi, A. *Electrochim. Acta* **2011**, *56*, 5823.

(74) Gupta, N.; Linschitz, H.

(75) Barrosse-Antle, L. E.; Hardacre, C.; Compton, R. G. *J. Phys. Chem. B* **2009**, *113*, 2805.

Chapter 6

Voltammetric Measurement of Oxygen Concentration in a series of Bis(trifluoromethylsulfonyl)-imide Anion-Based Room Temperature Ionic Liquids

This chapter measures oxygen uptake in a series of bis(trifluoromethylsulfonyl)imide anion-based room temperature ionic liquids (RTILs). Cyclic voltammetry is first used to observe the reduction of oxygen in RTILs and chronoamperometric measurement is next applied to simultaneously determine both the concentration and the diffusion coefficient of oxygen in the different RTILs. The viscosity of the RTILs is also reported. It is found that the diffusion coefficient of oxygen generally increases with decreasing viscosity of the RTILs. The work in this chapter involved collaboration with Dr. Peter Goodrich and Mr. Alex Neale from the Queen's University Ionic Liquid Laboratories, Belfast (QUILL). Dr. Peter Goodrich synthesised the RTILs and Mr. Alex Neale conducted the viscosity measurements for the RTILs. We conducted oxygen uptake experiments jointly. The work reported here will be submitted for publication.

6.1 Introduction

In parallel with the development of new and, more importantly, sustainable technologies for energy production, significant research interest is also being placed upon the advancement of electrical energy storage systems. In addition to improving electrical energy storage systems in portable electronics, where the lithium-ion (Li-ion) secondary battery dominates at present, this aspiration also arises from the goal of developing the next generation of high energy capacity systems for electric vehicles (EVs) and hybrid-electric vehicles (HEVs).

Among all prospective secondary battery technologies, the lithium-oxygen (Li-O_2) [or lithium-air (Li-air)] battery has received a significant portion of interest in recent years. This attention, in both the academic and industrial fields, can be attributed to the remarkable theoretical specific energy of this particular chemistry: which is close to 3458 $\mathrm{Wh \cdot kg^{-1}}$ based on the mass of the discharge product, lithium peroxide, Li_2O_2 (calculation based on the nominal voltage of 2.96 V).[1] However, many investigations have revealed important practical challenges associated with this chemistry, including high overpotentials during charging and discharging, and undesirable decomposition reactions of the electrolyte or electrode materials.[2,3] These factors dramatically reduce the efficiency and cyclability of such systems. As such, the primary focus of research into this field concerns investigations in search of stable electrolytes and cathode materials.

During the ideal discharge of a Li-O_2 battery, the oxygen reduction reaction (ORR) at the cathode generates the superoxide radical ($O_2^{\bullet -}$)

$$O_2 + e^- \rightleftharpoons O_2^{\cdot -} \tag{6.1}$$

which, in turn, rapidly reacts with Li^+ ions to form the lithium-oxide discharge products; lithium superoxide (LiO_2) and, by disproportionation of LiO_2, lithium peroxide (Li_2O_2).[2,4] Under ideal charging conditions, Li_2O_2 decomposition would occur exclusively to regenerate the reactants, Li^+ and O_2. Although a seemingly simple reversible process, the particularly reactive nature of the superoxide species results in competing side reactions and significant electrolyte decomposition in many organic solvents. For example, in an organic carbonate based electrolyte, the $O_2^{\bullet-}$ radical reacts almost entirely with the solvent to form lithium alkylcarbonates and Li_2CO_3 which passivate the electrode surface.[5] Comparatively, both ether and DMSO based electrolytes, frequently used in Li-air battery studies, allow the reversible formation of Li_2O_2 during cycling. However, while more stable than carbonate solvents, reactive decomposition of ether electrolytes becomes significant even after the first cycle.[6,7] On the other hand, competing side reactions in DMSO electrolytes are less favoured but these slower decomposition reactions between DMSO, Li_2O_2 and $O_2^{\bullet-}$ have been observed and eventually lead to capacity fade.[8,9]

Room temperature ionic liquids (RTILs) have received growing attention for their potential use as electrolytes for electrochemical energy storage devices for numerous factors including non-flammability, negligible vapour pressure, hydrophobicity and good thermal and electrochemical stability. Perhaps most interestingly, a selection of ionic liquid structures, most notably utilising non-aromatic alkylammonium cations, are considered to exhibit good stability towards the superoxide radical.[10,11] Indeed, the electrochemical generation of $O_2^{\bullet-}$ (ORR) has been studied in ionic liquids for over 2 decades; first observed irreversibly in a 1-ethyl-3-methylimidazolium chloride-aluminium chloride RTIL.[12] The first reported instance of the reversible electroreduction of O_2 (*i.e.* without significant and rapid side-reactions between $O_2^{\bullet-}$ and the RTIL) was observed at a glassy carbon macroelectrode in 1-butyl-1-methylimidazolium hexafluorphosphate ($[C_4mim][PF_6]$)[13] and has since been reported in numerous other studies concerning imidazolium, alkylammonium and phosphonium based RTILs. [10,11,14-21]

Among several contributing factors affecting the rate capability and power output of a Li-air battery, the supply of reactants to the cathode surface is very significant. The other factors include, but are not limited to, the cathode porosity,[22] electrolyte and gas penetration into the porous cathode,[23,24] and cathode surface passivation with insoluble discharge products.[25] The question of transporting and supplying the reactants brings to light the major drawback of using RTIL-based electrolytes; RTILs are typically quite viscous and, although this class of liquids are completely ionic in form, they generally exhibit relatively low conductivity compared to aqueous solution. Crucially, since the diffusivity of components within the electrolyte (Li^+ and O_2) is approximately inversely proportional to the viscosity of the system, it is not surprising that the sluggish transport of these reactants in viscous RTILs impedes the rate capability of the RTIL-based Li-air batteries; this observation has been reported.[26,27]

The properties of each ionic liquid are determined by the structure of both the cation and anion, of which there is a virtually unlimited number of structures and combinations. With this factor in mind, RTILs may be considered tuneable solvents and the structures can be modified with the goal of optimising certain properties; like the solubility and diffusion of oxygen for instance. In this work, we use electrochemical methods to determine the solubility and diffusivity of oxygen in a selection of pure RTILs based on the bis(trifluoromethylsulfonyl)imide anion paired with a selection of cyclic alkylammonium based cations. These observations are compared with the measured viscosity of the RTIL. Exploring the relationship between the RTIL structure and the measured transport capabilities is necessary in the future design of novel ionic liquid structures with improved characteristics.

6.2 Experimental

The experiments were conducted with five room temperature ionic liquids: *N*-butyl-*N*-methylpyrrolidinium bis(trifluoromethanesulfonyl)imide [Pyrr$_{14}$][NTf$_2$], *N*-butyl-*N*-methylpiperidinium bis(trifluoromethanesulfonyl)imide [Pip$_{14}$][NTf$_2$], *N*-butyl-*N*-methylazepinium bis(trifluoromethanesulfonyl)imide [Aze$_{14}$][NTf$_2$], *N*-methyl-*N*-(2-methoxyethyl)pyrrolidinium bis(trifluoromethanesulfonyl)imide [Pyrr$_{1(2o1)}$][NTf$_2$], and *N*-methyl-*N*-(2-methoxyethyl)piperidinium bis(trifluoromethanesulfonyl)imide [Pip$_{1(2o1)}$][NTf$_2$]. The chemical structures of the five cations and bis(trifluoromethanesulfonyl)imide anion, their names and abbreviations are shown in **Figure 6.1**. The syntheses of all five RTILs were carried out by Dr. Peter Goodrich, at QUILL, as described in Chapter 3.

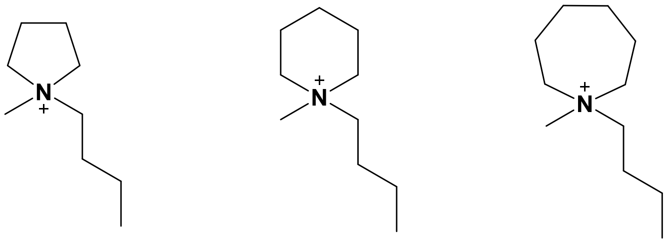

N-butyl-N-methyl-pyrrolidinium [Pyrr$_{14}$]$^+$ **N-butyl-N-methyl-piperidinium [Pip$_{14}$]$^+$** **N-butyl-N-methyl-azepinium [Aze$_{14}$]$^+$**

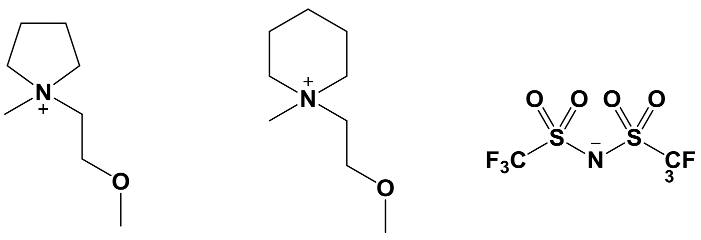

N-methyl-N-(2-methoxy-ethyl)pyrrolidinium [Pyrr$_{1(2o1)}$]$^+$ **N-methyl-N-(2-methoxy-ethyl)piperidinium [Pip$_{1(2o1)}$]$^+$** **bis(trifluoromethane-sulfonyl)imide [NTf$_2$]$^-$**

Figure 6.1: Chemical structures of the cyclic alkylammonium RTIL cations and anion used in this chapter, along with their names and abbreviations.

Prior to any electrochemical or physical measurements, the RTILs were dried by completing several freeze/thaw cycles under high vacuum (10^{-3} mbar). Following the freeze/thaw process, the RTILs were kept under high vacuum at elevated temperature (90 °C) with stirring overnight. The resulting moisture content of the RTILs did not exceed 40 ppm water, as measured by Karl Fischer titration using an 899 Coulometer (Metrohm). RTILs were immediately stored and sealed under an Argon (Ar) atmosphere inside an Ar-filled glovebox before further use. The viscosity of the RTILs was measured using a Gemini Rotonetic Drive 2 cone and plate rheometer (Bohlin).

The electrochemical measurements were conducted based on the T-cell set up described in Chapter 3. The microelectrode is immersed in *ca.* 10 μL of the RTIL solution of interest. Once constructed, the cell was placed inside a Faraday cage inside the glove box and then connected to a gas line. Externally to the glove box, the gas line (Ar or O_2) was fitted to a Dreschel bottle containing $CaCl_2$ to remove the residual water from the gas stream. The outlet of the gas line terminated inside a fume hood, via a connection through the glove box wall, to prevent the leakage of gas into the glove box atmosphere. The cell was initially purged with Ar for at least 30 minutes. Under an argon atmosphere, cyclic voltammetry is performed to observe any processes occurring in the absence of dissolved O_2. These scans were performed at 100 $mV \cdot s^{-1}$ and over the approximate potential range where oxygen is expected to occur; *ca.* 0 to -2.5 V *vs*. Ag. The cell was then exposed to a flow of pure O_2 gas at a pressure of 1 atm to allow diffusion of O_2 into the liquid sample. After 45 minutes, voltammograms for the reduction of O_2 are recorded. This is performed periodically until the resulting voltammograms are consistent, ensuring that O_2 saturation in the

RTIL had occurred. Once saturation had occurred, typically within a period of 1.5 to 2.5 hours, the concentration and diffusion coefficient of dissolved O_2 were determined by three times of chronoamperometric experiments. The Shoup and Szabo equation[28] were used to analyse the resultant potential step transients, as explained comprehensively in Chapter 4, section **4.2.2**, equations (4.3) and (4.4). Detailed data will be presented in the next section.

6.3 Results and Discussion

Several room temperature ionic liquids were selected as electrolytes in which to study the electrochemical reduction of dissolved oxygen and a microdisk electrode. It has been shown previously that the specific nature of both the anion and the cation will play a role in the solubility and transport of oxygen in the RTILs.[16] For this particular study, the anion species, $[NTf_2]^-$, is kept constant and the effect of changed cation structure is considered to investigate the interplay between the fine-tuning of cation structure, modification of physical properties and the oxygen electrochemistry. The exploration of these properties will, hopefully, be useful for the future design of improved RTIL-based electrolytes for Li-air batteries.

6.3.1 Cyclic Voltammetry of Oxygen in RTILs

Cyclic voltammetry of the platinum microdisk electrode was initially used to probe the electro-reduction of O_2 dissolved in the RTIL electrolyte. For all voltammograms presented, the potential was swept initially in the negative direction from a starting voltage of 0 V *vs*. Ag at a scan rate of 100 $mV \cdot s^{-1}$. The background voltammograms, collected under Ar-atmosphere (labelled: Blank), and the voltammograms obtained once O_2 saturation in the IL had occurred are presented in **Figure 6.2**. The temperature for all cyclic voltammetry and chronoamperometry experiments was 298 ± 0.5 K, as dictated by the internal atmosphere of the glove box.

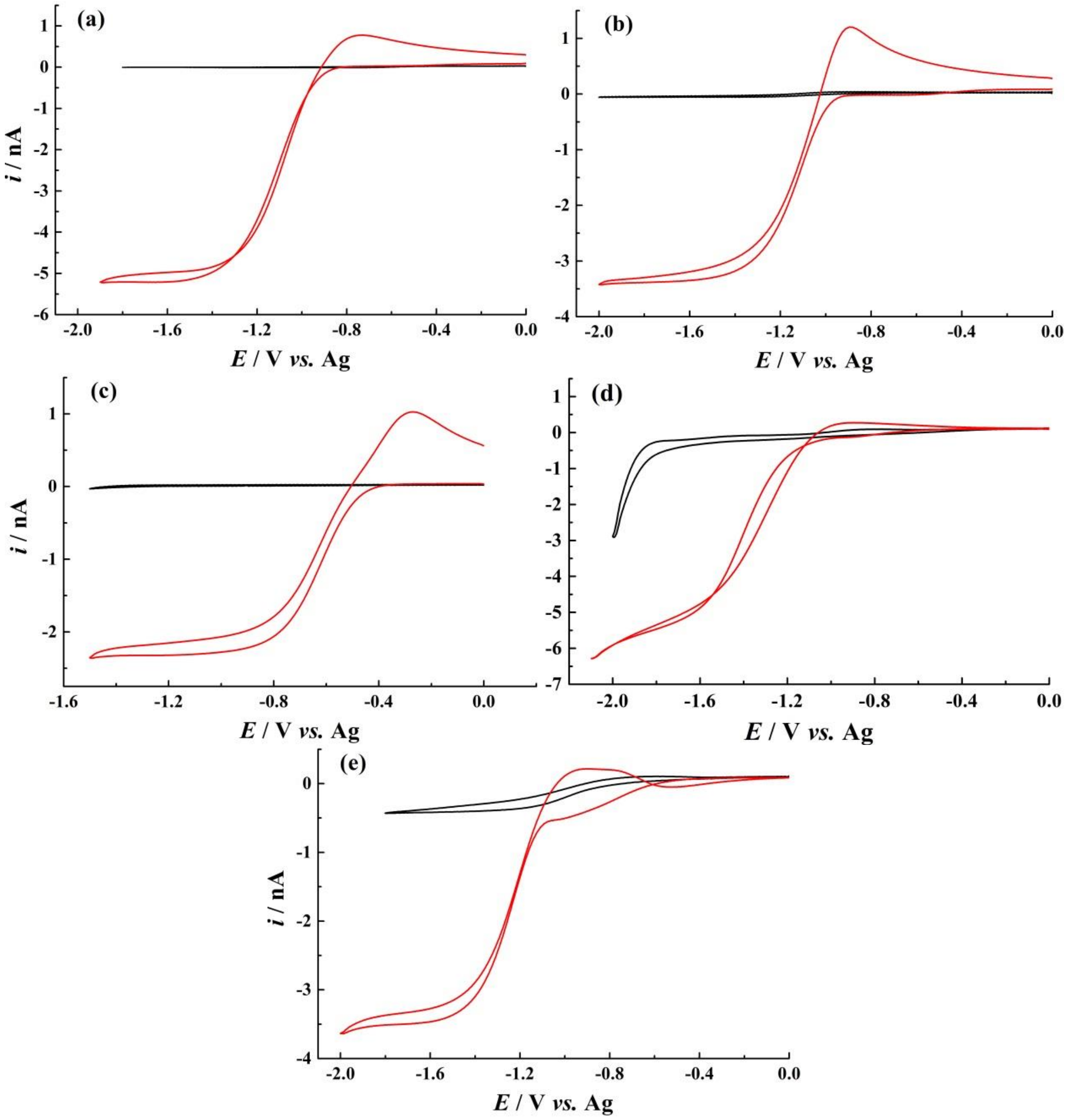

Figure 6.2: Cyclic voltammograms (▬) for the reduction of O_2 at a 10 μm diameter Pt-microdisk electrode *vs.* Ag in (a) $[Pyrr_{14}][NTf_2]$, (b) $[Pip_{14}][NTf_2]$, (c) $[Aze_{14}][NTf_2]$, (d) $[Pyrr_{1(2o1)}][NTf_2]$ and (e) $[Pip_{1(2o1)}][NTf_2]$. The blank traces (▬) were obtained under an Ar-atmosphere prior to exposure to O_2 gas. A scan rate of 100 mV·s^{-1} was used in all cases.

Under a pure Argon-atmosphere, the current response was found to be very low and completely negligible within the potential region of interest for the RTILs, with the exception of [$Pyrr_{1(2o1)}$][NTf_2] and [$Pip_{1(2o1)}$][NTf_2]. The blank CV obtained for [$Pyrr_{1(2o1)}$][NTf_2], **Figure 6.2d**, shows the onset of reduction of an unknown species at *ca.* -1.8 V *vs.* Ag. Fortunately, as the CV shows, this process occurs at more negative potentials than the reduction of dissolved O_2 measured in subsequent experiments. The blank CV obtained for [$Pip_{1(2o1)}$][NTf_2] shows a small current response, approximately - 0.4 *n*A, possibly corresponding to the reduction of the contaminant gases. Under different conditions, dissolved volatiles could be more efficiently removed by bubbling with Ar directly into the liquid, an option not possible for the 10 μL used in T-cells, or by exposing the RTIL to vacuum.

For the three RTILs functionalised with the butyl group, [$Pyrr_{14}$][NTf_2], [Pip_{14}][NTf_2] and [Aze_{14}][NTf_2] (**Figures 6.2a-c**), no measurable reduction peak was observed prior to the onset potential of O_2 reduction. On the other hand the ether functionalised ILs, [$Pyrr_{1(2o1)}$][NTf_2] and [$Pip_{1(2o1)}$][NTf_2] (**Figures 6.2d-e**), both exhibited small pre-peak features in the O_2 saturated CVs. The current magnitude of these features appears of much greater significance in the piperidinium-based RTIL, corresponding to approximately 2 % and 15 % of the O_2 reduction peak in [$Pyrr_{1(2o1)}$][NTf_2] and [$Pip_{1(2o1)}$][NTf_2], respectively. These pre-peak processes indicate the possibility of the O_2 reduction reaction being coupled with an immediate chemical reaction of the superoxide product with either solvent molecules or impurities within the solvent, known as an EC mechanism, as described in Chapter 1.[29] The direct chemical reaction of the superoxide radical leads to a depletion of the concentration of the reduced species local to the electrode surface. This, in turn, causes a shift of the reduction wave towards more positive potentials provided the wave is electrochemically reversible. The magnitude of this pre-peak indicates the likelihood that the chemical reaction of the $O_2^{\cdot -}$ is occurring with an impurity, X, in the electrolyte, where the concentration of X does not exceed the concentration of O_2. This can be inferred due to the presence of two reduction peaks (*i.e.* the pre-peak and the main O_2 reduction peak). Once species X is completely consumed *via* the chemical reaction with $O_2^{\bullet -}$, the remaining O_2 undergoes reduction at the electrode by a mechanism more representative of the heterogeneous process; an electrochemical reduction in the absence of a coupled chemical reaction. This observation has been made previously in a study into Li_2O_2 formation by reduction of O_2 in the presence of known concentrations of Li^+ ions in the solvent.[4]

Considering the reduction peak for this set of RTILs, the peak shape appears to resemble steady-state characteristics. This behaviour is typical of oxygen reduction at microdisk electrodes where the convergent diffusion of the reactants is expected at slow-to-mid scan rates.[17] For the alkyl functionalised RTILs, **Figures 6.2a-c**, the shape of the overall voltammogram is asymmetrical and a clear transient peak, associated with more planar diffusion, is observed for the reverse oxidation process. This observation is quite typical for the oxygen systems due to the asymmetry exhibited by the diffusion coefficients of the neutral and reduced species; the diffusion coefficient of the superoxide radical has been found to over one order of magnitude less than the neutral oxygen in many media.[11,14,30] Significant interactions between the charged superoxide species and the charged species of the RTILs are likely to contribute to the very low mobility of the anion. Additionally, the magnitude of the oxidation peak relative to the reduction peak increases in the order

[Pyrr$_{14}$][NTf$_2$] < [Pip$_{14}$][NTf$_2$] < [Aze$_{14}$][NTf$_2$] which expectedly correlates with an increase in the viscosity in the same order (see later for viscosity data).

For the RTILs containing the ether-functional group, **Figures 6.2d-e**, the magnitude of the current response on the reverse oxidation sweep is considerably smaller and more representative of a system under convergent hemispherical type diffusion. It would seem rather ambitious to contribute the lack of a transient peak on the reverse scan to a much greater mobility of the superoxide radical in these two RTILs. Nevertheless, the presence of the oxygen in the ether-functional group of the cation could certainly be expected to alter the cation charge distribution and, in turn, alter the strength or manner of the interaction between the RTIL cation and the radical anion. Experimental measurement of the superoxide diffusivity in these RTILs could be a worthwhile consideration. The type of transient oxidation peaks observed in **Figures 6.2a-c** are typically observed at microelectrodes in more viscous media.[17] However, comparing [Pyrr$_{14}$][NTf$_2$] with the two ether functionalised RTILs reveals that the order of viscosity of the RTIL ([Pyrr$_{1(2o1)}$][NTf$_2$] < [Pyrr$_{14}$][NTf$_2$] < [Pip$_{1(2o1)}$][NTf$_2$]) does not correlate well with the order of the magnitude of the reverse oxidation peak ([Pyrr$_{1(2o1)}$][NTf$_2$] < [Pip$_{1(2o1)}$][NTf$_2$] < [Pyrr$_{14}$][NTf$_2$]). This absence of a reverse oxidation could be the result of direct chemical reaction and consumption of the superoxide with the RTIL, but this is worth further investigation.

An interesting feature appears on the reverse scan of [Pip$_{1(2o1)}$][NTf$_2$] under oxygen, **Figure 6.2e**, at approximately 0.5 V *vs.* Ag where a net reducing current is observed. This unusual observation was not found in the other RTILs. Consider this RTIL also exhibit largest reduction pre-peak among all RTIL samples in the study, it is very likely that superoxide anion reacted with the solvent or impurities in the RTIL.

6.3.2 Chronoamperometric measurements

Chronoamperoemtry was performed on each of the O_2-saturated RTIL electrolytes to determine the solubility and diffusivity of the dissolved oxygen. In chronoamperometric measurements, the potential was stepped from 0 V *vs.* Ag (where the faradic current is negligible) to a potential where the reduction of the dissolved oxygen is diffusional controlled. As shown in the voltammograms presented in **Figure 6.2**, this potential varied between each sample as a result of the use of a silver pseudo-reference electrode. As such, the step potential for a given RTIL is determined from the associated voltammogram of that particular RTIL. The potential stepped for each RTIL can be found in the brackets in the legend of **Figure 6.3**. The potential was held at the reducing potential over a period of a few seconds and the resulting transients were analysed using the Shoup and Szabo equation[28] (as described in Chapter 4) to extract the diffusion coefficient of oxygen, *D*, and the concentration of oxygen dissolved in the bulk electrolyte, *c*. The resulting experimental chronoamperometric transients and the associated simulated transients are presented in **Figure 6.3**. Excellent agreements between the experimental and the Shoup and Szabo computed transients are observed. The solubility, *c*, and diffusion coefficient, *D*, of oxygen derived from the Shoup and Szabo analysis are presented in **Table 6.1** along with the viscosity of each RTIL. Multiple chronoamperometric experiments were performed for each RTIL, as described in the experimental methodology section, and, as such, the solubility and diffusion coefficient values in

Table 6.1 represent the average values of these experiments and the calculated standard error is shown for each sample.

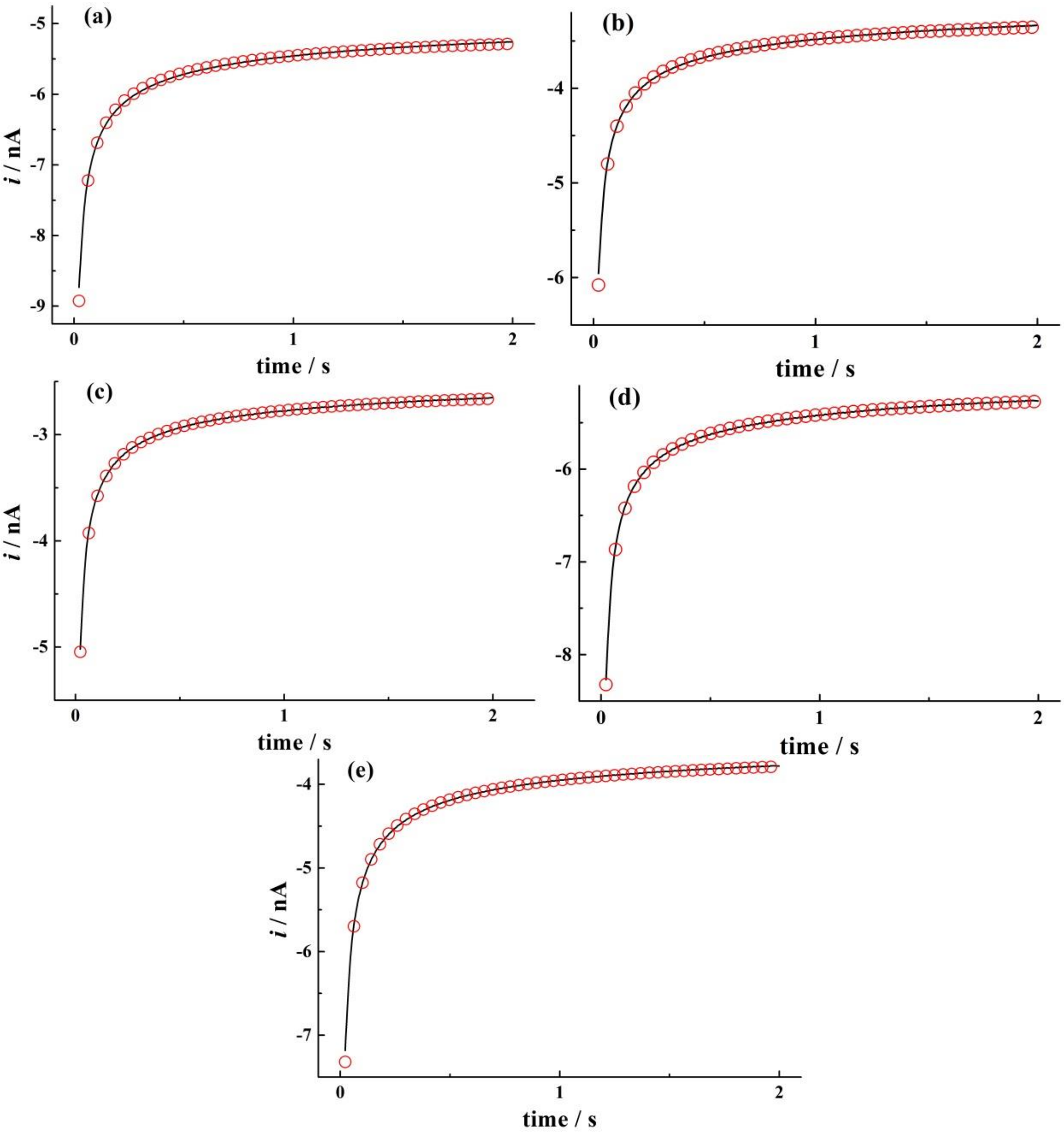

Figure 6.3: Experimental (▬) and simulated (○) chronoamperometric transients for the reduction of O_2 at 297 K under 1 atm O_2 pressure in (a) [Pyrr$_{14}$][NTf$_2$] (-1.7 V), (b) [Pip$_{14}$][NTf$_2$] (-1.75 V), (c) [Aze$_{14}$][NTf$_2$] (-1.4 V), (d) [Pyrr$_{1(2o1)}$][NTf$_2$] (-1.88 V) and (e) [Pip$_{1(2o1)}$][NTf$_2$] (-1.86 V).

The mobility of the dissolved oxygen in this selection of RTILs appears to approximately follow an inverse trend with respect to the viscosity, which will be discussed at a later point in this chapter, while the trend in the solubility of oxygen is less obviously elucidated. The effect of the ethereal oxygen atom on the RTIL cation could be expected to change the manner in which oxygen interacts with the RTIL and, therefore, adjust the solubility of the gas relative to the alkyl-functionalised analogues. However, for the pyrrolidinium-based RTILs, $[\mathrm{Pyrr}_{14}][\mathrm{NTf}_2]$ and $[\mathrm{Pyrr}_{1(2o1)}][\mathrm{NTf}_2]$, the substitution of the butyl-group with the 2-methoxyethyl group impedes the solubility of O_2 while the opposite can be said for the piperidinium-based RTILs, $[\mathrm{Pip}_{14}][\mathrm{NTf}_2]$ and $[\mathrm{Pip}_{1(2o1)}][\mathrm{NTf}_2]$. More RTILs with different cation structures should be tested to probe this observation further.

Also presented in **Table 6.1** is the equivalent data for dimethyl sulfoxide (DMSO), a commonly used solvent for Li-air battery electrolyte studies. As is expected for relatively viscous systems like RTILs, the observed range for the diffusion coefficient of the dissolved oxygen in these RTILs (from 1.39 to 3.76×10^{-10} $\mathrm{m^2 \cdot s^{-1}}$) is significantly lower than for the non-viscous molecular solvent. Interestingly, the literature value provided was taken from a recent study concerning the properties of a DMSO/$[\mathrm{Pyrr}_{14}][\mathrm{NTf}_2]$ blended electrolyte for Li-air battery applications.[31] Expectedly, the results of this particular study demonstrated that the addition of DMSO to the RTIL improved the mobility of the dissolved oxygen associated with a reduction of the viscosity relative to the pure RTIL system.[31]

Table 6.1: Solubility, *c*, and diffusion coefficient, *D*, data for oxygen in the series of RTILs at 298 K derived from the Shoup and Szabo analysis of chronoamperometric transients and the viscosity, *η*, of the RTILs at the same temperature. The equivalent data for a DMSO electrolyte taken from literature is provided for comparison.

Ionic liquids	c / mmol·dm^{-3}	D / × 10^{-10} m^{2}·s^{-1}	η / mPa·s
[Pyrr$_{14}$][NTf$_2$]	9.15 ± 0.15	2.67 ± 0.05	80.02
[Pip$_{14}$][NTf$_2$]	8.48 ± 0.09	1.82 ± 0.02	177.93
[Aze$_{14}$][NTf$_2$]	7.98 ± 0.20	1.50 ± 0.04	323.27
[Pyrr$_{1(2o1)}$][NTf$_2$]	6.67 ± 0.13	3.76 ± 0.14	55.49
[Pip$_{1(2o1)}$][NTf$_2$]	12.21 ± 0.04	1.39 ± 0.01	108.56
DMSO	1.8[a]	18[a]	1.99[b]

[a] solubility and diffusion coefficient data for O_2 in DMSO was measured electrochemically at 25 °C with 0.1 mol·dm^{-3} tetrabutlyammonium hexafluorophosphate as the supporting electrolyte.[31]
[b] viscosity of pure DMSO given at 298 K.[32]

6.3.3 The Relationship between Diffusivity and Viscosity

As previously stated the diffusion coefficient of dissolved species is generally found to be inversely proportional to the viscosity of the solvent medium. For the RTILs presented here, the change in viscosity associated with different cation structures is well known. For example, the largest observed differences is associated with the observed increase in viscosity as size of the alkyl ring of the cation is increased, from the five membered ring of the [Pyrr$_{14}$][NTf$_2$] to the six and seven membered rings of [Pip$_{14}$][NTf$_2$] and [Aze$_{14}$][NTf$_2$], respectively. Additionally, the measured reduction in viscosity as a result of substituting the butyl functional group of the cation with the 2-methoxyethyl group has been documented previously.[33] This reduction in viscosity for the ether-functionalised cation analogue (*i.e.* comparing [Pyrr$_{14}$][NTf$_2$] to [Pyrr$_{1(2o1)}$][NTf$_2$] and [Pip$_{14}$][NTf$_2$] to [Pip$_{1(2o1)}$][NTf$_2$]) is attributed to an increased free volume as a result of the additional conformational flexibility of the ethereal chain.[33] The relationship between the measured viscosity of the RTIL and the diffusion coefficient of a species can be quite well described, for certain systems, by the Stokes-Einstein equation:

$$D = \frac{k_B T}{6\pi\eta\alpha} \tag{6.2}$$

where D is the diffusion coefficient of the dissolve species, k_B is the Boltzmann constant (1.38×10^{-23} $m^2 \cdot kg \cdot s^{-1} \cdot K^{-1}$), T is the temperature, η is the viscosity of the solvent and α is the hydrodynamic radius of the species.[16] Alternative versions of this expression have been considered to better describe this relationship in significantly viscous solvents like RTILs.[34] However, the inverse relationship between mobility and viscosity remains and, as such, can be utilised to probe these properties in the RTILs. A plot of the diffusion coefficient versus the inverse viscosity of oxygen is presented in **Figure 6.4**.

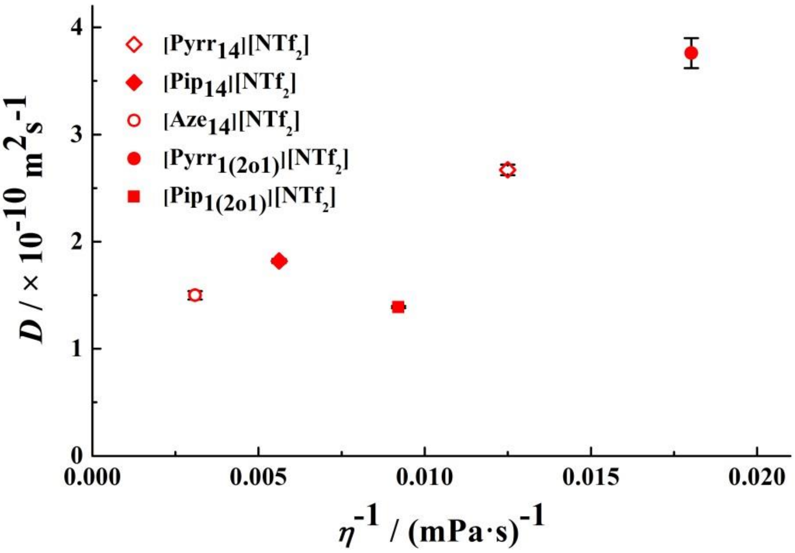

Figure 6.4: Stokes-Einstein plots for the dependence of the diffusion coefficient of O_2, D, on the inverse viscosity, η^{-1}, at 298K for [$Pyrr_{14}$][NTf_2], [Pip_{14}][NTf_2], [Aze_{14}][NTf_2], [$Pyrr_{1(2o1)}$][NTf_2] and [$Pip_{1(2o1)}$][NTf_2].

With the exception of [Pip$_{1(2o1)}$][NTf$_2$], the measured diffusion coefficients of oxygen in these RTILs appears to correlate reasonably well with a decrease in viscosity. However, there is not a direct dependence of D on η^{-1} since the plot has a large intercept. The deviation away from ideal behaviour across all the samples is not surprising; previous studies concerning the applicability of the standard Stokes-Einstein equation have previously found that for small molecules, such as H_2, H_2S and O_2, the expected relationship does not apply and suggest analyte-RTIL interactions may play a more significant role in the movement, or lack thereof, of the analyte.[16] However, if the diffusion coefficient of the dissolved oxygen in [Pip$_{1(2o1)}$][NTf$_2$] is lower than expected because of stronger interactions the RTIL cation, which may incidentally explain the higher solubility of the gas in this RTIL, this reasoning then generates the question of why the same observation is not made for the two RTILs of the most similar structures with it, [Pyrr$_{1(2o1)}$][NTf$_2$] or [Pip$_{14}$][NTf$_2$]. A further deviation away from this relationship is obvious if the diffusion coefficient of O_2 in DMSO and the viscosity of this solvent are considered. Extrapolation of an approximated linear fit of the data presented in **Figure 6.4** would suggest that the mobility of the oxygen in the non-viscous solvent, DMSO, should approach 70-80 × 10^{-10} $m^2 \cdot s^{-1}$, indicating a different diffusivity – viscosity relationship in RTIL systems.

6.4 Conclusions

The reduction of oxygen was performed in five room temperature ionic liquids samples which made up of bis(trifluoromethyl-sulfonyl)imide anion and a selection of cyclic alkylammonium based cations. Clear oxygen reduction peaks were recorded in all five dry RTIL samples. The concentration and diffusion coefficient of oxygen in different RTILs were analysed from chronoamperometric measurements. The diffusion coefficients of oxygen in five RTILs were compared with their measured viscosity. It is seen that the diffusivity generally decreases as the viscosity increases, but the interaction between solvated O_2 with RTIL composition is likely to change the obstruct the diffusion of O_2 in RTILs and hence results in a smaller diffusion coefficient.

Reference

(1) Girishkumar, G.; McCloskey, B.; Luntz, C.; Swanson, S.; Wilcke, W. *J. Phys. Chem. Lett.* **2010**, *1*, 2193.

(2) Bruce, P. G.; Freunberger, S. A.; Hardwick, L. J.; Tarascon, J.-M. *Nat. Mater.* **2012**, *11*, 19.

(3) Balaish, M.; Kraytsberg, A.; Ein-Eli, Y. *Phys. Chem. Chem. Phys.* **2013**, *16*, 2801.

(4) Peng, Z.; Freunberger, S. A.; Hardwick, L. J.; Chen, Y.; Giordani, V.; Bardé, F.; Novák, P.; Graham, D.; Tarascon, J.-M.; Bruce, P. G. *Angew. Chem., Int. Ed.* **2011**, *50*, 6351.

(5) Xu, W.; Xu, K.; Viswanathan, V. V.; Towne, S. A.; Hardy, J. S.; Xiao, J.; Nie, Z.; Hu, D.; Wang, D.; Zhang, J.-G. *J. Power Sources* **2011**, *196*, 9631.

(6) Freunberger, S. A.; Chen, Y.; Drewett, N. E.; Hardwick, L. J.; Barde, F.; Bruce, P. G. *Angew. Chem., Int. Ed.* **2011**, *50*, 8609.

(7) Han, S.-M.; Kim, J.-H.; Kim, D.-W. *J. Electrochem. Soc.* **2014**, *161*, A856.

(8) Trahan, M. J.; Mukerjee, S.; Plichta, E. J.; Hendrickson, M. A.; Abraham, K. M. *J. Electrochem. Soc.* **2013**, *160*, A259.

(9) Kwabi, D. G.; Batcho, T. P.; Amanchukwu, C. V.; Ortiz-Vitoriano, N.; Hammond, P.; Thompson, C. V.; Shao-Horn, Y. *J. Phys. Chem. Lett.* **2014**, *5*, 2850.

(10) Hayyan, M.; Mjalli, F. S.; Hashim, M. A.; AlNashef, I. M.; Al-Zahrani, S. M.; Chooi, K. L. *J. Electroanal. Chem.* **2012**, *664*, 26.

(11) Herranz, J.; Garsuch, A.; Gasteiger, H. A. *J. Phys. Chem. C* **2012**, *116*, 19084.

(12) Carter, M. T.; Hussey, C. L.; Strubinger, S. K. D.; Osteryoung, R. A. *Inorg. Chem.* **1991**, *30*, 1149.

(13) AlNashef, I. M.; Leonard, M. L.; Kittle, M. C.; Matthews, M. A.; Weidner, J. W. *Electrochem. Solid-State Lett.* **2001**, *4*, D16.

(14) Buzzeo, M. C.; Klymenko, O. V.; Wadhawan, J. D.; Hardacre, C.; Seddon, K. R.; Compton, R. G. *J. Phys. Chem. A* **2003**, *107*, 8872.

(15) Barnes, A. S.; Rogers, E. I.; Streeter, I.; Aldous, L.; Hardacre, C.; Wildgoose, G. G.; Compton, R. G. *J. Phys. Chem. C* **2008**, *112,* 13709.

(16) Huang, X.-J.; Rogers, E. I.; Hardacre, C.; Compton, R. G. *J. Phys. Chem. B* **2009**, *113*, 8953.

(17) Rogers, E. I.; Huang, X.-J.; Dickinson, E. J. F.; Hardacre, C.; Compton, R. G. *J. Phys. Chem. C* **2009**, *113*, 17811.

(18) Allen, C. J.; Mkurjee, S.; Plichta, E. J.; Hendrickson, M. A.; Abraham, K. M. *J. Phys. Chem. Lett.* **2011**, *2*, 2420.

(19) Allen, C. J.; Hwang, J.; Kautz, R.; Mukerjee, S.; Plichta, E. J.; Hendrickson, M. A.; Abraham, K. M. *J. Phys. Chem. C* **2012**, *116*, 20755.

(20) Hayyan, M.; Mjalli, F. S.; AlNashef, I. M.; Hashim, M. A. *J.Fluorine Chem.* **2012**, *142*, 83.

(21) Li, P.; Barnes, E. O.; Hardacre, C.; Compton, R. G. *J. Phys. Chem. C* **2015**, *119*, 2716.

(22) Ma, S. B.; Lee, D. J.; Roev, V.; Im, D.; Doo, S.-G. *J. Power Sources* **2013**, *244*, 494.

(23) Tran, C.; Yang, X.-Q.; Qu, D. *J. Power Sources* **2010**, *195*, 2057.

(24) Balaish, M.; Kraytsberg, A.; Ein-Eli, Y. *ChemElectroChem* **2014**, *1*, 90.

(25) McCloskey, B. D.; Speidel, A.; Scheffler, R.; Miller, D. C.; Viswanathan, V.; Hummelshøj, J. S.; Nørskov, J. K.; Luntz, A. C. *J. Phys. Chem. Lett.* **2012**, *3*, 997.

(26) Higashi, S.; Kato, Y.; Takechi, K.; Nakamoto, H.; Mizuno, F.; Nishikoori, H.; Iba, H.; Asaoka, T. *J. Power Sources* **2013**, *240,* 14.

(27) Soavi, F.; Monaco, S.; Mastragostino, M. *J. Power Sources* **2013**, *224*, 115.

(28) Shoup, D.; Szabo, A. *J. Electroanal. Chem. Interfacial Electrochem.* **1982**, *140*, 237.

(29) Bard, A. J.; Faulkner, L. R.; 2nd ed.; *Electrochemical Methods: Fundamentals and Applications*, Wiley: New York, 2001.

(30) Evans, R. G.; Klymenko, O. V.; Saddoughi, S. A.; Hardacre, C.; Compton, R. G. *J. Phys. Chem. B* **2004**, *108*, 7878.

(31) Khan, A.; Zhao, C. *Electrochem. Commun.* **2014**, *49,* 1.

(32) Gaylord Chemical: 2013.

(33) Chen, Z. J.; Xue, T.; Lee, J.-M. *RSC Advances* **2012**, *2,* 10564.

(34) Vorotyntsev, M. A.; Zinovyeva, V. A.; Picquet, M. *Electrochim. Acta* **2010**, *55*, 5063.

Chapter 7

Voltammetry at Porous Electrodes: An Experimental and Theoretical Study

This chapter describes voltammetry at two contrasting types of porous electrodes, namely graphite felt and vitreous carbon foam electrodes. Both of these electrodes have a pre-formed porous structure, but the former has a much more compact internal porous structure. Voltammetry in hexaammineruthenium(III) chloride ($Ru(NH_3)_6Cl_3$) in 0.1 M potassium chloride (KCl) aqueous solution is used to characterise the electrodes in the light of newly developed theory. Vitreous carbon foam electrodes were also employed for the Oxygen (O_2) reduction reaction. Specifically, a hollow sphere model that approximates the diffusion within the interior pores together with semi-infinite diffusion to the exterior electrode surface was used to simulate the voltammetry of both systems. Excellent agreement for reduction peak currents was achieved between experiment and simulation, demonstrating the validity of the theoretical model in determining the average pore size and exterior electrode surface area. The work presented here has involved collaboration with Dr. Edward O. Barnes in respect of Theory and the latter has been published in the *Journal of Electroanalytical Chemistry*.[1]

7.1 Introduction

As described in Chapter 2, porous electrodes are receiving growing interest in electroanalytical measurements because of the scope for altered voltammetric responses which may offer a lower overpotential and a more sensitive response for some processes than conventional macroelectrodes systems where mass transport occurs exclusively via semi-infinite diffusion. Hitherto many porous electrodes have been fabricated by electroplating metals (mostly gold) on template layers of spheres before they are finally removed. These electrodes, as exemplified in **Table 7.1** for illustrative systems, have been used for electrochemical sensing to detect species such as NADH (a coenzyme often involved in metabolism),[2-4] glucose,[5-7] nitrobenzene,[8] hydrogen peroxide,[9] and as the basis for a number of immunosensors.[10-12]

Table 7.1: Composition and uses of porous electrodes. *A human protein which is an indicator for inflammation.[13] **A human protein which is an indicator for coronary artery disease.[14]

Porous material	Hollow void radius (nm)	Target species
Gold	320	NADH[2]
Gold	550	NADH[3]
Ruthenium oxide	150	NADH[4]
Gold	125	Glucose[5]
Polyaniline/Prussian blue	250	Glucose[6]
Ionic liquid doped poly (*N*[3-(trimethyoxysilyl)propyl]aniline	250	Glucose[7]
Platinum nanoparticle modified carbon	55	Nitrobenzene[8]
Gold nanoparticle doped titanium dioxide with immobilised haemoglobin	250	Hydrogen peroxide[9]
Gold	250	C-reactive protein*[10]
Ionic liquid doped polyaniline	125	Hepatitis B surface antigen[11]
Gold	125	Human apolipoprotein B-100**[12]

This Chapter examines different types of porous electrode in which the porous structure is pre-formed, namely graphite felt and vitreous carbon foam electrodes. These materials have large interior surface areas arising from their high void volumes (≥ 95%) and are very popular for industrial applications such as energy storage[15-17] and redox flow batteries.[18-21]. However, these two materials have major differences in their structure: graphite felt material is made of randomly distributed carbon fibres so it has a high Young's modulus and tensile strength;[22] whereas vitreous carbon foam material has a reticulated carbonaceous skeleton which has a much lower strength.[15,22]

A theoretical model for the porous electrodes is developed seeking to identify the contributions to the voltammetric signals resulting from material diffusing to the electrode surface from bulk solution and from material within the holes of the porous structure. It is anticipated qualitatively that the latter will give rise, under suitable timescales, to a 'thin layer' type response. This chapter thus highlights the comparison between the experimental reduction peak currents and the simulated currents. The excellent agreement shows that the theoretical model provides good approximation for electrochemical processes occurring in and at porous electrodes.

7.2 Theory

The theoretical model and programming were developed by Dr. Edward O. Barnes. Electrochemistry at a porous electrode is simulated here. Consider a simple one electron transfer process:[1]

$$A \pm e^{-} \rightleftharpoons B \tag{7.1}$$

It is assumed that the electron transfer takes place in the solution with a large excess amount of inert supporting electrolyte to ensure that mass transport is exclusively diffusion.

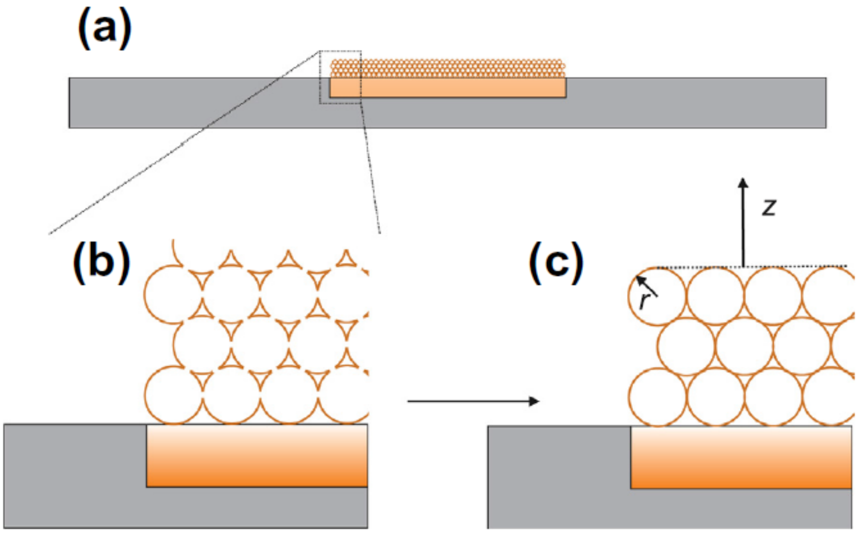

Figure 7.1: a) Schematic illustration of the cross section from a porous electrode consisting of a series of hollow spheres supported on a disc electrode (note the size of spheres relative to the disc electrode is greatly exaggerated); b) a zoomed in illustration to highlight the interconnected nature of the spheres; c) a description of the model employed to simulate electrochemistry at porous electrode.[1]

The porous electrode is considered to be a series of interconnected spherical voids within a conductive material. These electrodes might for example be fabricated by supporting a range of nano-sized polystyrene spheres on the surface of a macroelectrode, and surrounding them with a layer of, for instance, electro-deposited gold. The spheres would then be dissolved away, leading to a network of interconnected holes, through where solution containing the solute of interest may permeate. Note alternative porous structures are used in the experimental approach described below. It is assumed that the porous layer comprises hollow spheres formed from where the template was dissolved and tiny pores of negligible size linking adjacent spheres for the simplicity of the theory and to generate an idealised structure amenable to theoretical modelling. This assumption enables the entire porous layer to be flooded by the electrolyte when immersed in a solution. This is shown schematically in **Figure 7.1**, which shows a view of the spheres supported on a disc electrode (a), and a zoomed in illustration of the porous, interconnected hollow sphere structures (b). In this study, the electrode is modelled as a series of identical, hollow, independent conductive spheres, as shown in **Figure 7.1c**. It is assumed that, in the experiment, negligible diffusion occurs either from sphere to sphere or between spheres and the bulk solution. If the spheres are small enough compared to the radius of the disc electrode where they are supported, the top of the layer (s) of spheres can be considered as a disc electrode. The reasons for this simplification are discussed next.

The electrochemical behaviour of flat micro- (and nano-) electrode arrays can be divided into four distinct categories,[23-29] as shown in **Figure 7.2**. In case 1, the experimental timescale is short enough so that the diffusion layers are independent and do not overlap. This results in linear diffusion and a Cottrellian response from the array as a whole. The timescale is longer, in case 2, and while the electrodes still have independent diffusion layers, these layers are now large compared to the electrodes and convergent diffusion occurs in this case. The response can be considered to be that of some independent microelectrodes. In case 3, the diffusion layers begin to overlap as they become comparable in size to the electrode separation. In case 4, the diffusion layers are very large relative to the electrodes and the separation distance between them, thus the diffusion layers merge into a single diffusion layer, and the array effectively behaves as a single, much larger electrode, and Cottrellian (planar diffusion) behaviour is again observed. By considering the top layer of spheres to behave as a case 4 array, it can be modelled as a macroelectrode response. This will be valid provided at least several layers of spheres are used in the electrode construction and that $\sqrt{Dt} > r_s$, where t is the experimental timescale, D is the diffusion coefficient of the species of interest and r_s is the radius of the sphere. These conditions are thought to hold for the electrodes studied later in this chapter.

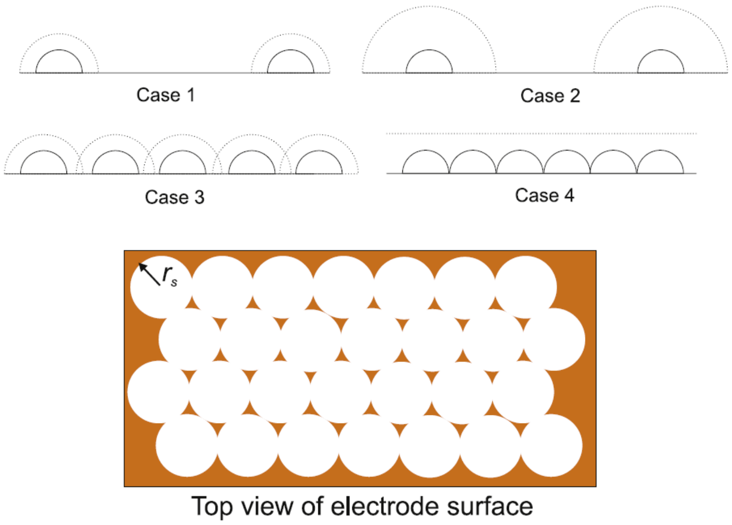

Figure 7.2: Schematic diagram of the four cases for electrochemical responses at a micro- (or nano-) electrode array, and a top view of a porous electrode surface, showing the close packing of hemispherical hollows.[1]

Further to this assumption of modelling the top layer of spheres as a case 4 electrode array, we also assume that diffusion inside the hollow spheres is completely decoupled from the diffusion down to the top layer of spheres. We also assume that no diffusion occurs between individual spheres. This allows us to simulate the response inside a single sphere and the response at a disc electrode. The single sphere result can be multiplied by the number of spheres present, and added to the disc response from the exposed top layer of spheres to give an overall response. This model is used to simulate two electrochemical experiments: potential step chronoamperometry and cyclic voltammetry, which are next discussed in turn.

Table 7.2: Parameter definitions

Parameter	Description	Units
α/β	Electron transfer coefficient	Unitless
c_i	Concentration of species i	$mol\cdot m^{-3}$
c_i^*	Bulk solution concentration of species i	$mol\cdot m^{-3}$
c_i^0	Electrode surface concentration of species i	$mol\cdot m^{-3}$
D_i	Diffusion coefficient of species i	$m^2\cdot s^{-1}$
E	Applied potential	V
E_f^o	Formal potential	V
I	Current	A
k^0	Heterogeneous rate constant	$m\cdot s^{-1}$
r	Radial coordinate	m
$r_{s/d}$	Radius of sphere/disc	m
N	Number of spheres	Unitless
t	Time	s
z	z Coordinate	m

7.2.1 Simulation of Chronoamperometry within a Single Sphere

In a potential step chronoamperometric experiment, the potential applied to the electrode is firstly held at a value where no electron transfer takes place, then stepped to a value where the electrochemical reaction is fully driven in a diffusion controlled way. The spherically symmetric environment inside a sphere can be reduced to a one dimensional system. The dependence of concentration of any species on time is given by Fick's second law in spherically symmetric space:

$$\frac{\partial c_i}{\partial t} = D_i(\frac{\partial^2 C_i}{\partial r^2} + \frac{2}{r}\frac{\partial c_i}{\partial r}) \tag{7.2}$$

where c_i is the concentration and D_i the diffusion coefficient of species i, and r is the radial coordinate, equal to zero at the centre of the sphere, and equal to r_s at the inside edge of the sphere. Symbols are defined in **Table 7.2**. Initial conditions are:

$$t = 0,\ \text{all } r;\ c_A = c_A^* \tag{7.3}$$

Note that for single step chronoamperometry, as considered here, species B in equation (7.1) need not be considered.

At time $t = 0$, the start of the experiment, the electrode potential is stepped, and the boundary condition at the electrode surface becomes:

$$t \geq 0,\ r = r_s;\ c_A = 0 \tag{7.4}$$

At the centre of the sphere, a zero flux boundary condition is imposed on both species as a result of symmetry:

$$t \geq 0,\ r = 0;\ \frac{\partial c_A}{\partial r} = 0 \tag{7.5}$$

Dimensionless parameters are introduced in order to simplify the model. These parameters are listed in **Table 7.3**. Upon introduction of these parameters, the mass transport equation becomes:

$$\frac{\partial C_i}{\partial \tau} = D_i'(\frac{\partial^2 C_i}{\partial R^2} + \frac{2}{R}\frac{\partial C_i}{\partial R}) \tag{7.6}$$

Table 7.4 lists the dimensionless boundary conditions. To determine the current, a dimensionless flux at the sphere surface is given by:

$$j_s = (\frac{\partial C_A}{\partial R})_{R=1} \tag{7.7}$$

This is then converted into a real, dimensional current, *I*/A, through:

$$I_s = 4\pi F r_s c_A^* D_A j_s \tag{7.8}$$

7.2.2 Simulation of Cyclic Voltammetry within a Single Sphere

The only modification needs be conducted to the above model in order to simulate cyclic voltammetry inside a sphere is the electrode surface boundary condition, where Butler–Volmer kinetics are instead employed. Using Butler–Volmer kinetics,[30] which can be shown to be a limiting form of assymetric Marcus–Hush theory,[31] the flux at the electrode surface for the reduction of A to B is given by:

$$D_A(\frac{\partial c_A}{\partial r})_{r=r_s} = k^0\left[c_A^0 \exp\left(-\alpha\frac{F\left(E-E_f^o\right)}{RT}\right) - c_B^0 \exp(\beta\frac{F\left(E-E_f^o\right)}{RT})\right] \tag{7.9}$$

where α and β are transfer coefficients, and it is assumed that $\alpha + \beta = 1$. Symbols and dimensionless parameters definitions and can also be found in **Tables 7.2** and **7.3**.

Table 7.3: Normalised parameter definitions

Normalised parameter	Definition
C_i	$\frac{c_i}{c_A^*}$
D_i'	$\frac{D_i}{D_A}$
K^0	$\frac{r_s}{D_A}k^0$
$R*$	$\frac{R}{r_s}$
σ	$\frac{Fr_s^2}{RTD_A}v$
θ	$\frac{F\left(E-E_f^o\right)}{RT}$
τ	$\frac{D_A}{r_s^2}t$
Z	$\frac{z}{r_d}$

$R*$ is the dimensionless radial coordinate, which is 0 in the centre of the sphere and 1 at the edge of the sphere.

Conservation of mass results in equal fluxes of species A and B:

$$D_B\frac{\partial c_B}{\partial r} = -D_A\frac{\partial c_A}{\partial r} \tag{7.10}$$

Dimensionless boundary conditions are again summarised in **Table 7.4**. The dimensionless flux density and the real current are calculated the same as for chronoamperometry.

Table 7.4: Normalised boundary conditions for electrochemistry inside a hollow sphere

boundary	Cyclic voltammetry condition
All R, $\tau < 0$	$C_A = 1$ $C_B = 0$
$R = 1$, $\tau \geq 0$	$\frac{\partial C_A}{\partial R} = K^0\left[C_A^0 e^{-\alpha\theta} - C_B^0 e^{\beta\theta}\right]$ $D_B' \frac{\partial C_B}{\partial R} = -\frac{\partial C_A}{\partial R}$
$R = 0$, $\tau \geq 0$	$\frac{\partial C_i}{\partial R} = 0$

7.2.3 Simulation of Chronoamperometry and Cyclic Voltammetry at a Disc Electrode

Chronoamperometry at a disc electrode is well characterised and can be determined with the aid of the Shoup and Szabo equation.[32-34] In the hypothetical porous electrode model described here, we decouple the current response from the interior spheres from that of the overall 'disc'. Hence there are two electrode radii, one for the sphere and the other for the disc, which without due care will complicate the analysis of theoretical results in terms of dimensionless parameters. Therefore, the radius of the spheres is used as the basis for the dimensionless parameters in the model. A dimensionless disc radius, R_d, must then be defined as:

$$R_d = \frac{r_d}{r_s} \tag{7.11}$$

The Shoup and Szabo equation can be described then, by:

$$j_d = R_d \frac{2}{\pi}(0.7854 + 0.4432(\frac{\tau}{R_d^2})^{-0.5} + 0.2145\exp[-0.3912(\frac{\tau}{R_d^2})^{-0.5}] \quad (7.12)$$

and

$$I_d = 2\pi F D_A c_A^* r_s j_d \quad (7.13)$$

The simulation methods for cyclic voltammetry at a macrodisc electrode are well developed. The relevant mass transport equation is:

$$\frac{\partial C_i}{\partial \tau} = D_i'(\frac{\partial^2 C_i}{\partial Z^2}) \quad (7.14)$$

The definition of symbols and dimensionless parameters used can also be referred in **Tables 7.2** and **7.3**. Butler–Volmer kinetics are again used as the electrode surface boundary condition, now applied at $Z = 0$ rather than $R = 1$. A zero flux bulk solution boundary condition is applied at $Z_{MAX} = 6\sqrt{D'_{MAX}\tau_{MAX}}$, where D'_{MAX} is the largest (dimensionless) diffusion coefficient in the system and τ_{MAX} is the total dimensionless time taken to run the experiment. This position has been shown to be well outside the diffusion layer.[35-37] Dimensionless boundary conditions, and the boundaries at which they apply, for a macrodisc are shown in **Table 7.5**.

The dimensionless flux at the disc, j_d, is defined as:

$$j = \frac{I}{4\pi F D_A c_A^* r_s} \quad (7.15)$$

is given by:

$$j_d = \frac{R_d}{2}(\frac{\partial C_A}{\partial Z})_{Z=0} \quad (7.16)$$

Table 7.5: Normalised boundary conditions for cyclic voltammetry at a macrodisc electrode.

Boundary	*Cyclic voltammetry condition*
All Z, $\tau < 0$	$C_A = 1$ $C_B = 0$
$R = 0$, $\tau \geq 0$	$\frac{\partial C_A}{\partial R} = K^0\left[C_A^0 e^{-\alpha\theta} - C_B^0 e^{\beta\theta}\right]$ $D'_B \frac{\partial C_B}{\partial R} = -\frac{\partial C_A}{\partial R}$
$R = 6\sqrt{D'_{MAX}\tau_{MAX}}, \tau \geq 0$	$\frac{\partial C_i}{\partial R} = 0$

7.2.4 Total Current at a Porous Electrode

It is assumed that the electrochemical response at a porous electrode is the sum of the responses inside the hollow spheres (by modelling the pores) and the disc like response from diffusion to the top layer of spheres. If there is negligible diffusion between individual spheres and the bulk during electrolysis, then the overall current will be the sum of the two responses:

$$I = I_s + I_d \tag{7.17}$$

where I_s and I_d refer to the currents from the interior spheres and the esxterior disc, respectively. If defining the overall number of interior spheres as N, then in dimensionless terms:

$$j = Nj_s + j_d \tag{7.18}$$

and

$$I = 4\pi F D_A c_A r_s j \tag{7.19}$$

7.2.5 Numerical Methods

Dr. Edward O. Barnes developed the numerical simulation of chronoamperometry and cyclic voltammetry, which necessitates the discretisation of the mass transport equations and boundary conditions in space and time, for which the Crank–Nicolson method is used.[38] The equations are then solved simultaneously and implicitly over all space using the Thomas algorithm[39] to solve the large banded matrices produced.

Appropriate spatial and temporal grids must be defined to discretise and solve the equations over. For chronoamperometry, the temporal grid consists of a dense, regular mesh of points from $\tau = 0$ up to some switching value, τ_s. After this value, the temporal grid expands and becomes less dense. Mathematically:

$$\tau_0 = 0 \tag{7.20}$$

$$\tau \leq \tau_s : \tau_k = \tau_{k-1} + \Delta_\tau \tag{7.21}$$

$$\tau > \tau_s : \tau_k = \tau_{k-1} + \gamma_\tau(\tau_{k-1} - \tau_{k-2}) \tag{7.22}$$

For cyclic voltammetry, the temporal grid is defined in terms of the dimensionless potential. Each unit of θ is divided into N_θ evenly spaced points. The temporal grid is then defined to be:

$$\tau_k = \tau_{k-1} + \frac{1}{N_\theta \sigma} \tag{7.23}$$

For the spatial grid inside a sphere (for both chronoamperometry and cyclic voltammetry), the grid expands away from the electrode surface at R = 1 after an initial step of Δ_R. Mathematically:

$$R_0 = 1 \tag{7.24}$$

$$R_1 = 1 - \Delta_R \tag{7.25}$$

$$R_j = R_{j-1} - \gamma_R(R_{j-2} - R_{j-1}) \tag{7.26}$$

The final R point is defined as zero, the centre of the sphere.

For a macrodisc, a similar grid is used, with an initial step size of Δ_Z from zero, and then expanding out to bulk solution:

$$Z_0 = 1 \tag{7.27}$$

$$Z_1 = \Delta_Z \tag{7.28}$$

$$Z_j = Z_{j-1} + \gamma_R(Z_{j-1} - Z_{j-2}) \tag{7.29}$$

Convergence studies found the following grid parameters sufficient to ensure simulated results were within 0.2% of fully converged outcomes: $\Delta_\tau = 1 \times 10^{-9}$, $\tau_s = 1 \times 10^{-5}$, $\gamma_\tau = 1.0001$, $N_\theta = 100$, $\Delta_R = \Delta_Z = 1 \times 10^{-5}$, $\gamma_R = \gamma_Z = 1.01$. Typical run times were of the order 5 to 10 s per simulation. The models were programmed in C++ and all simulations carried out on an Intel (R) Xenon (R) 2.26 GHz PC with 2.25 GB RAM.

7.3 Experimental

The fabrication of the porous electrodes was described in Chapter 3. Both the felt and foam electrodes were first studied in $Ru(NH_3)_6Cl_3$ aqueous solution with 0.1 M KCl as supporting electrolyte.

Before the study, nitrogen (N_2) was bubbled for 30 minutes to eliminate oxygen (O_2) which could influence the voltammetry. A 10.0 μM $Ru(NH_3)_6Cl_3$ aqueous solution with 0.1 M KCl supporting electrolyte was used with either graphite felt or vitreous carbon foam electrode to study the redox reaction (7.30).

$$[Ru(NH_3)_6]^{3+}(aq) + e^- \rightleftharpoons [Ru(NH_3)_6]^{2+}(aq) \tag{7.30}$$

Note that it is difficult to remove the trapped air from the interior pores of graphite felt electrode by aqueous solutions due to the hydrophobicity of the carbon fibres and the small average interior pore size. The trapped air in the pores would block the electrode surface in contact with electrolyte, thus it is necessary to remove the trapped air. The data generated without air removal will be shown in next section. An electrode wetting procedure was developed according to the literature.[17] The graphite felt electrode was rinsed with deionised water after washing in ethanol, and then agitated in a sacrificial sample of the test solution before being transferred to the electrochemical cell. The effect of the pre-washing time was tested: the electrode was either rinsed by pure ethanol rapidly or immersed in pure ethanol for 10 minutes before rinsed by deionised water carefully, cyclic voltammetry was then measured with the electrode rinsed for different time. The results of different pre-washing time will be shown in the next section.

Pre-washing procedure is not required for vitreous carbon foam electrode as the foam material has a much larger pore size (r_s = 0.208 mm) and more open porous structure, thus the electrolyte is easily completely flooded into the pores. The vitreous carbon foam electrode was next studied in oxygen saturated aqueous solution.

In both $Ru(NH_3)_6Cl_3$ and oxygen systems studied with different electrodes, three cyclic voltammograms were performed at 10, 20, 50, 100, 200, 400 and 800 $mV{\cdot}s^{-1}$ scan rate to ensure the equilibrium was reached and the solution was stirred between each measurement. Care was taken not to create air bubbles when stirring if the graphite felt electrode was employed for the reason explained above.

All the experiments were conducted in a thermostatted Faraday cage at 298 K. Variation of the peak current with scan rate were investigated to examine the active area for both electrodes. Simulation of the voltammetric response was employed to examine the theoretical model given above.[1]

7.4 Results and Discussion

The electrochemistry of the graphite felt and vitreous carbon foam electrodes in 10.0 μM $Ru(NH_3)_6Cl_3$ aqueous solution with 0.1 M KCl as supporting electrolyte is studied. Then computer modelling is performed to simulate the current generated from interior and exterior pores, respectively. The electrochemistry of oxygen reduction reaction is also studied using a vitreous carbon foam electrode. Computer modelling is also employed in the oxygen reduction reaction system.

7.4.1 Electrochemistry of the Graphite Felt Electrodes

The wetting process using non-aqueous solvent, discussed briefly in section **7.3** was important and different washing times were tested to find an optimal time. **Figure 7.3** shows the voltammetry of the $Ru(NH_3)_6Cl_3$ redox reaction measured using graphite felt electrodes without pre-washing and pre-washed by ethanol and dionised water either rapidly or for 10 minutes, recorded at 20 $mV \cdot s^{-1}$, respectively. All graphite felt electrodes used in this thesis have the same dimensions of 5.1 mm diameter and 1.1 mm thickness, as described in Chapter 3. It can be seen that the electrode without pre-washing produces negligible current compared to the electrodes with pre-treatment process. The other two electrodes, which are pre-washed either instantly or for 10 minutes, produced identical voltammograms, and the small difference of peak potentials (~ 10 mV) can be explained by the use of Ag pseudo-reference electrode. Therefore, **Figure 7.3** demonstrates that the pre-washing is a crucial step so as to activate the full electrode surface of the graphite felt electrode. Furthermore, the electrode is completely wetted by rapidly washing with ethanol and dionised water as the peak currents has no difference from that with 10 minutes pre-washing time, thus long time pre-treatment is unnecessary for improved voltammetric results.

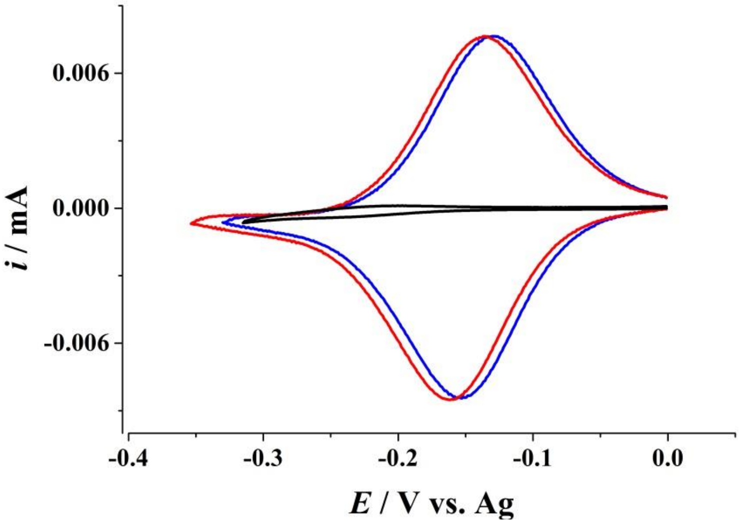

Figure 7.3: Voltammograms of the 10.0 μM $Ru(NH_3)_6Cl_3$ redox reaction measured using graphite felt electrodes without pre-washing (▬) and pre-washed by ethanol instantly (▬) or for 10 (▬) minutes, at 298 K, 20 mV·s^{-1}. Dimensions for all three disc electrodes: 5.1 mm diameter, 1.1 mm thickness.

Next, the effect of variable scan rate on the peak current was investigated. **Figure 7.4** shows the resulting voltammetry in 10.0 μM $Ru(NH_3)_6Cl_3$ aqueous solution at 10, 20, 50, 100, 200, 400 and 800 mV·s^{-1} scan rate. A clear reduction peak can be seen at around -0.2 V, and an oxidation back peak at around -0.15 V, associated with the one electron redox reaction of $Ru(NH_3)_6Cl_3$.[40] At low scan rates the voltammograms show 'thin layer' character (see **Figure 7.3**) whilst at fast scan rate the effect of diffusion are more evident.

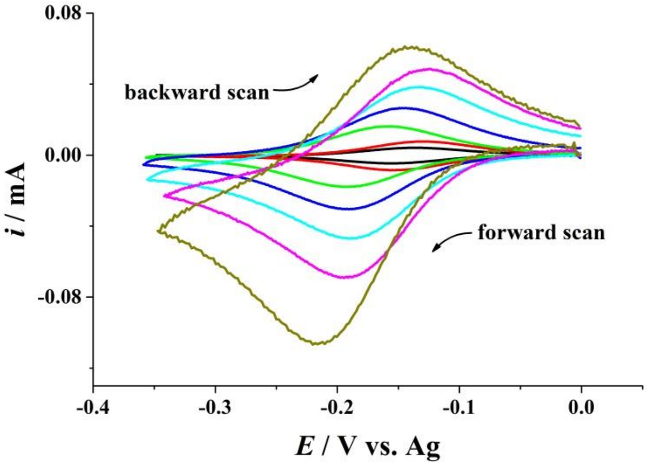

Figure 7.4: $Ru(NH_3)_6Cl_3$ redox voltammetry with graphite felt electrode at 10 (▬), 20 (▬), 50 (▬), 100 (▬), 200 (▬), 400 (▬) and 800 (▬) $mV \cdot s^{-1}$ scan rate.

We next consider the analysis of the data in **Figure 7.4** and assume the exterior surface S_s of the graphite felt electrode as a disc electrode, which has dimensions of 0.51 cm diameter and 0.11 cm thickness. The exterior surface area of the 'disc electrode' is therefore 0.58 cm^2.

Further, consider the graphite felt electrode as a cylinder, and then the volume of the electrode V can be calculated as:

$$V = \pi \times r_e^{2} \times l \tag{7.31}$$

where r_e = 0.255 cm, is the radius of the approximate disc electrode and l (=0.11 cm) is the thickness of the electrode. According to the material specification given in Chapter 3, 95% of electrode volume is occupied by pores, thus the number of pores n_p and the overall electrode active area S can be calculated as:

$$n_p = \frac{95\% \times V}{\frac{4}{3} \times \pi \times r^3} \tag{7.32}$$

$$S = n_p \times 4 \times \pi \times r^2 + S_s \tag{7.33}$$

where r is the radius of interior pores, n_p is the number of interior pores, Thus S can be calculated for any particular value of r.

Next the reversible Randles Sevcik equation is introduced,[41]

$$i_p = (2.69 \times 10^5) n^{\frac{3}{2}} A D^{\frac{1}{2}} C v^{\frac{1}{2}} \tag{7.34}$$

where i_p is the reduction peak current, n (= 1) is the number of electrons transferred, A is the electrode area, D and C are the diffusion coefficient of $Ru(NH_3)_6Cl_3$ (8.5×10^{-6} $cm^2 \cdot s^{-1}$)[40] and concentration (10.0 μM) of $Ru(NH_3)_6Cl_3$, respectively, and v is the scan rate. Thus A can be roughly estimated from the experimental data. Equations (7.33) and (7.34) will be used later to estimate the overall electrode active area assuming that the internal pore contribution is entirely diffusional and not 'thin layer'. This will be shown later to only applicable for faster voltage scan rates.

The reduction peak current (i_p) was plotted against the square root (sqrt) of scan rate (v) for $Ru(NH_3)_6Cl_3$ reduction process, according to equation (7.34), to initially approximately explore the active electrode area in the experiment. **Figure 7.5** shows an approximately linear dependence between experimental reduction peak current and square root of scan rate in the redox system, together with simulated peak current against square root of scan rate. Note that the currents measured at low scan rates do not conform to equation (7.34). The simulation was conducted using the theory proposed by Dr. Edward O. Barnes as discussed above. The simulation data in **Figure 7.5** was performed in two parts including the current generated from interior pores and from the exterior 'disc electrode'. The heterogeneous rate constant k^0 is nominally assumed to be 100 m·s^{-1} for a fully reversible reaction. The exterior area of the graphite felt electrode S_s was fixed at 0.58 cm^2 whilst the average pore radius r and the number of pores n_p were varied to find the best fit result. The parameters used in the simulation are listed in **Table 7.6**.

Table 7.6: Parameters used in the simulation for $Ru(NH_3)_6Cl_3$ reduction using graphite felt electrode. D is the diffusion coefficient of $Ru(NH_3)_6Cl_3$, α is the transfer coefficient, k^0 is the heterogeneous rate constant, r is the radius of interior pores, n_p is the number of interior pores, S_s is the exterior area of the graphite felt electrode, C is the concentration of $Ru(NH_3)_6Cl_3$ in aqueous solution.

Parameters	**values**
D^{40} / m^2·s^{-1}	8.5 × 10^{-10}
α	0.5
$k^0 / m \cdot s^{-1}$	*100
r / m	9 × 10^{-5}
n_p	15500
S_s / m^2	5.8 × 10^{-5}
C / mM	1 × 10^{-2}

*nominal value

The best fit average pore radius r for the simulated data presented in **Figure 7.5** was 9 ± 0.5 × 10^{-5} m. The values of n_p and S were calculated using equations (7.32) and (7.33). They were found to be 15500 ± 850 and 16 ± 0.9 cm^2, respectively.

It is seen that the current generated from interior pores is similar in value to experimental data, as shown by the green squares and black squares in **Figure 7.5**, respectively, which means that the majority amount of current is contributed from the interior pores.

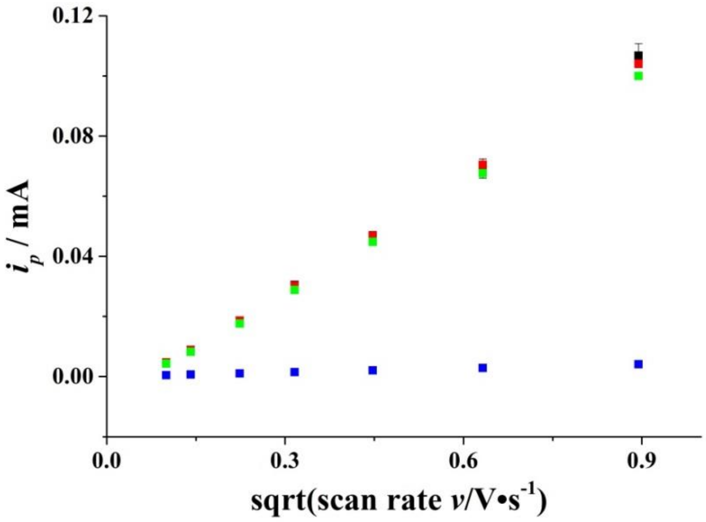

Figure 7.5: Ru(NH$_3$)$_6$Cl$_3$ reduction i_p vs. sqrt(v) with graphite felt electrode. Experimental current (■), simulated overall current (🟥), simulated current from interior pores (🟩) and from exterior disc electrode (🟦). Error bars in the experimental data generated from 3 sets of experiments. The parameters used in the simulation are explained in the text below.

The overall active area, S =16 cm^2, found from simulation approximately matches with the overall area value A estimated from equation (7.34), which was 17 cm^2, suggesting that at the faster scan rate used, the flux within the pores is more diffusional than ‘thin layer’. Note that for low scan rates the current is not proportional to the square root of the scan rate, as shown in **Figure 7.5**.

Cyclic voltammetry studied inside the spheres will vary significantly in character according to the scan rate used. All of the electroactive species inside a sphere will be consumed at lower scan rates (or small spheres) which will lead to a ‘thin layer’ response. However, the depletion layer cannot extend very far into the interior of the sphere at high scan rates (or large spheres), which will lead to a ‘diffusional’ response. Qualitatively this can be seen in **Figure 7.6**, which shows the simulated cyclic voltammograms generated from interior pores using the parameters listed in **Table 7.6**. A clear transition of the voltammograms is seen from a thin layer response, through an intermediate case to a diffusional response.

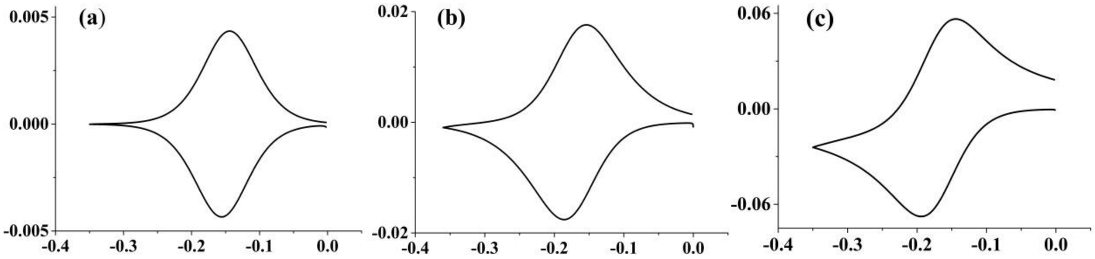

Figure 7.6: Simulated cyclic voltammograms at scan rate of (a) 10, (b) 50, (c) 400 mV·s^{-1}. For both three graph, X axis's unit is *E* / V vs. Ag, Y axis's unit is *i* / mA.

The transition between 'thin layer' to diffusional response from low to high scan rate can also be discerned from **Figures 7.3** and **7.4,** which show the experimental voltammograms, indicating that the interior signals contributed predominantly to the experimental voltammograms.

Figure 7.6 shows a transition behaviour which is confirmed with a plot of ln(i_p) against ln(scan rate). For a thin layer response, the peak height is proportional to the scan rate, whereas for a diffusional response, the peak height is proportional to the square root of the scan rate. This is seen in **Figure 7.7**, where the red squares in this figure show a plot of simulated reduction peak current generated from interior pores against scan rate, and the black square is ln-ln plot of experimental reduction peak current against scan rate. The gradient changes from 0.9 at low scan rate to 0.6 at high scan rate. **Figure 7.7** shows a very good agreement between experimental data with simulated interior current data, which further illustrates that the majority of current in the voltammograms is contributed from the interior pores of the graphite felt electrode.

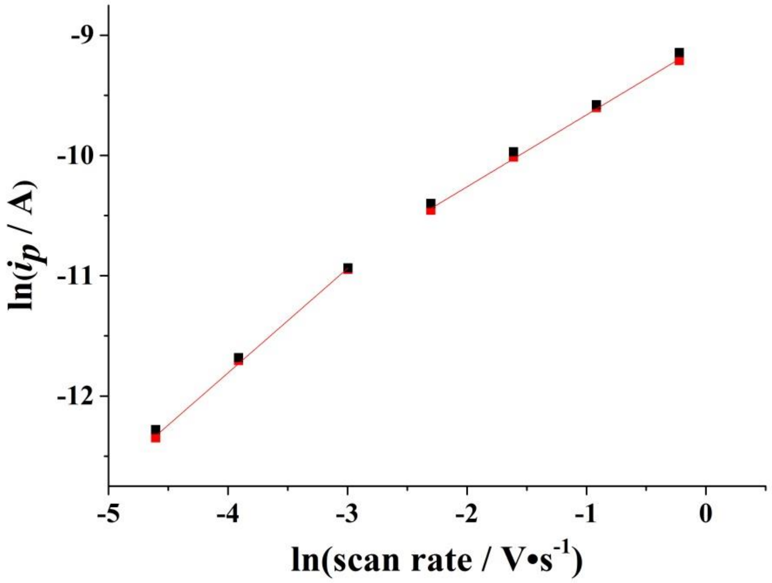

Figure 7.7: Experimental (■) and simulated interior (🟥) dimensionless reduction peak current as a function of dimensionless scan rate.

Herein, the graphite felt porous electrode was reported to give a stable and well-defined signal of $Ru(NH_3)_6Cl_3$ one electron redox reaction in a quiescent system. The detection limit can be as low as 10^{-6} M in concentration due to its large interior surface area. Our theoretical model adequately simulates the voltammetric process at graphite felt electrodes. The best fit average pore radius was found to be $9\pm0.5\times10^{-5}$ m and the overall active electrode surface area was as high as 17 cm^2 in a piece of 0.02 cm^3 volume graphite felt electrode.

7.4.2 Electrochemistry of the Vitreous Carbon Foam Electrodes

A vitreous carbon foam electrode (dimension: $0.5\times0.5\times0.32$ cm^3) was used in 10.0 μM $Ru(NH_3)_6Cl_3$ aqueous solution with 0.1 M KCl as supporting electrolyte, and O_2

saturated 0.1 M KCl aqueous solution to examine the porous electrode model derived previously in the context of this different electrode material.

Figure 7.8 shows the resulting voltammetry of $Ru(NH_3)_6Cl_3$ redox reaction. A clear reduction peak can be seen at around 0 V, and an oxidation back peak around 0.15 V, associated with the one-electron reaction of $Ru(NH_3)_6Cl_3$.[40]

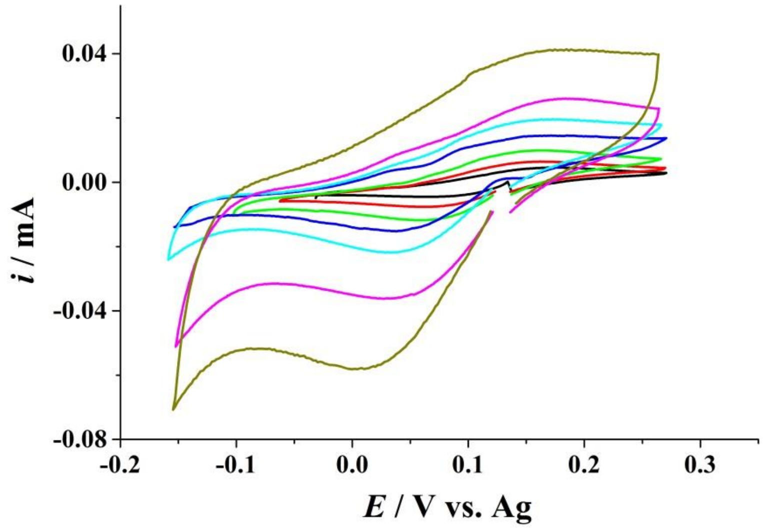

Figure 7.8: $Ru(NH_3)_6Cl_3$ redox voltammogramms with vitreous carbon foam electrode at 10 (—), 20 (—), 50 (—), 100 (—), 200 (—), 400 (—) and 800 (—) $mV\cdot s^{-1}$. Foam electrode dimensions: 0.5 × 0.5 × 0.32 cm^3.

The analysis of the reduction peak current at different scan rate is shown below, together with the results from the O_2 reduction system.

A new piece of vitreous carbon foam electrode was prepared for the set of O_2 reduction study as material was lost because of the extreme mechanical fragility of the foam material. The dimensions of two vitreous carbon foam electrodes were maintained to be the same, although some error was inevitable. The O_2 reduction voltammograms in **Figure 7.9** show clear reduction peaks at around -0.6 V at 10 mV·s^{-1} scan rate and these shifted to more negative potentials with scan rate as it increases up to 800 mV·s^{-1}.

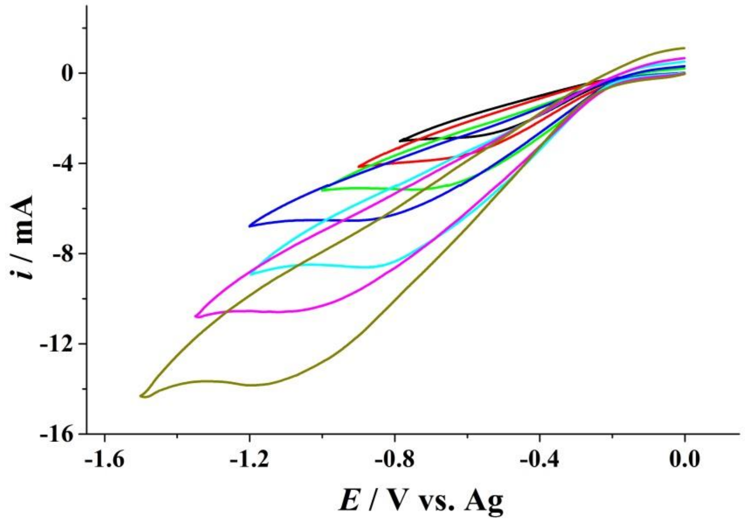

Figure 7.9: Voltammograms of saturated O_2 in 0.1 M KCl aqueous solution at 10 (▬), 20 (▬), 50 (▬), 100 (▬), 200 (▬), 400 (▬) and 800 (▬) mV·s^{-1} scan rate. Vitreous carbon foam electrode dimension: 0.5 × 0.5 × 0.32 cm^3.

Before considering the analysis of the data in **Figures 7.8** and **7.9**, we again first estimate the number of pores and the area of the vitreous carbon foam electrode. Consider the block foam electrode as a cuboid then the volume of the vitreous carbon foam electrode V and exterior surface area S_s can be calculated as:

$$V = l \times w \times h \tag{7.35}$$

$$S_s = 2 \times (l \times w + l \times h + w \times h) \tag{7.36}$$

where l (0.5 cm), w (0.5 cm) and h (0.32 cm) are the length, width and height of the vitreous carbon foam electrode, and these values were used in the simulation. According to the production specification given in Chapter 3, electrode fabrication section, 96.5% of the foam volume is occupied by pores and the pore radius r is

0.208 mm. Thus the foam electrode can be considered as a highly porous material for the area calculation. Thus the number of pores n_p and the overall electrode area S can be calculated as:

$$n_p = \frac{96.5\% \times V}{\frac{4}{3} \times \pi \times r^3} \tag{7.37}$$

$$S = n_p \times 4 \times \pi \times r^2 + S_s \tag{7.38}$$

Therefore, according to equation (7.37) and (7.38), the vitreous carbon foam electrode used in $Ru(NH_3)_6Cl_3$ and O_2 system has a volume V of around 0.080 cm^3 and an approximate electrode area S of around 12 cm^2.

Next, the peak current was plotted against the square root of scan rate in **Figure 7.10** for both $Ru(NH_3)_6Cl_3$ and O_2 reduction process to find the active electrode area of vitreous carbon foam electrode. The reversible one-electron transfer Randles Sevcik equation (7.34) was used for the experimental current in **Figure 7.10a** to estimate the active electrode area. The result was 8.6 cm^2 when the diffusion coefficient and concentration[40] of $Ru(NH_3)_6Cl_3$ are respectively 8.5×10^{-10} $m^2 \cdot s^{-1}$ and 10 μM. For the irreversible oxygen reduction process, the relevant form of the Randles Sevcik equation is:[42]

$$i_p = (2.99 \times 10^5) n (n' + \alpha_{n'+1})^{\frac{1}{2}} A D^{\frac{1}{2}} C v^{\frac{1}{2}} \tag{7.39}$$

where n is the number of electrons transferred, n' is the number of electron transferred before the rate determining step, $\alpha_{n'+1}$ is the dimensionless transfer coefficient of the rate determining step. $\alpha_{n'+1}$ was calculated to be 0.2 from a Tafel plot, which means the 1st electron transfer is the rate determining step and thus n' is 0.

The diffusion coefficient[43] D and concentration c was 1.96×10^{-9} $m^2 \cdot s^{-1}$ and 1.24 mM,[44] respectively. Therefore, the active electrode area calculated using the experimental data in **Figure 7.10b** was 9.4 cm^2.

Table 7.7: Parameters used in the simulation for $Ru(NH_3)_6Cl_3$ and O_2 reduction using vitreous carbon foam electrode. D is the diffusion coefficient, α is the transfer coefficient, k^0 is the heterogeneous rate constant, r is the radius of interior pores, n_p is the number of interior pores, S_s is the exterior area of the graphite felt electrode, C is the concentration of $Ru(NH_3)_6Cl_3$ or O_2 in aqueous solution.

Parameters	$Ru(NH_3)_6Cl_3$ system	O_2 system
D / $m^2 \cdot s^{-1}$	[40]8.5×10^{-10}	[43]1.96×10^{-9}
α	0.5	0.2
k^0 / $m \cdot s^{-1}$	*100	$k^0 exp\left(\frac{\alpha E_f^0}{RT}\right) = 1 \times 10^{-6}$
r / m	2.08×10^{-4}	2.08×10^{-4}
n_p	2050	2050
S_s / m^2	1.16×10^{-4}	1.16×10^{-4}
C / mM	1×10^{-2}	[44]1.24

*nominal value to ensure reversibility

The parameters used in the simulation for both systems are listed in **Table 7.7**. Note that in the $Ru(NH_3)_6Cl_3$ system, $k^0 = 100$ $m \cdot s^{-1}$ is only 'nominal' to ensure reversible behaviour whilst for a fully irreversible O_2 reduction process, only the compound parameter $k^0 exp\left(\frac{\alpha E_f^0}{RT}\right)$ can be reported rather than the k^0 separately. It is seen in **Figure 7.10** that a good agreement between experimental data and simulated peak current can be found. However, the difference between experimental and simulated data is slightly more apparent as compared to that seen for the graphite felt electrode. To some extent, this results from the fragile property of the foam material which led to imperfect electrode dimensions. In addition, air bubbles trapped in the carbon foam electrode could have opposite influence for two systems. In $Ru(NH_3)_6Cl_3$ experiment, air bubbles results in smaller active electrode area thus the simulated current is bigger than experimental value. In O_2 experiment, however, air bubbles, which contains around 20 vol% O_2, contribute more reductive current at the beginning of experiment whilst as the depletion of O_2, only inert N_2 left in the air bubbles. This further explains the crossover of simulated and experimental values in **Figure 7.10b**.

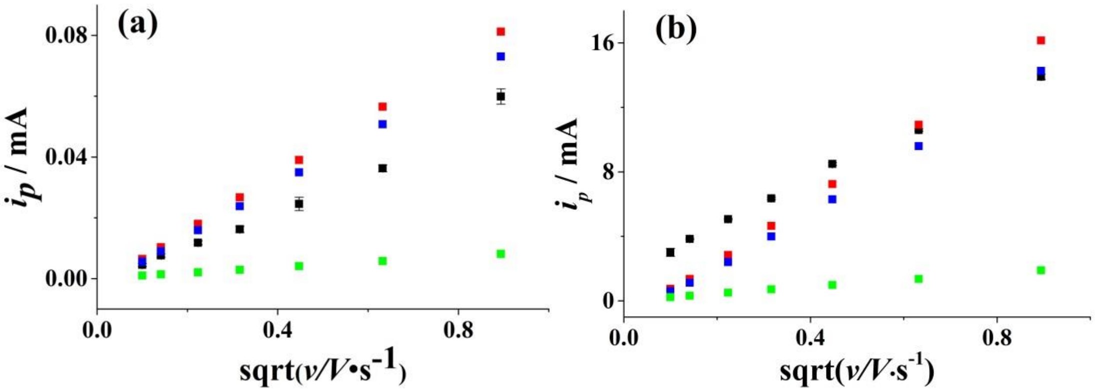

Figure 7.10: (a) $Ru(NH_3)_6Cl_3$ reduction i_p against the square root of scan rate plot using vitreous carbon foam electrode. Experimental current (■), simulated overall current (🟥), simulated current from interior pores (🟦) and exterior disc electrode (🟩); (b) O_2 reduction i_p against the square root of scan rate plot using vitreous carbon foam electrode.

The calculated active areas for both systems (8.6 and 9.4 cm^2) were relatively close to the area S (= 12cm^2) estimated using equations (7.37) and (7.38) with the supplier's data, confirming the porous property of the vitreous carbon foam electrode and the validity of the theoretical model.

7.5 Conclusions

A theory has developed which allows insight into the electrochemistry of porous electrode structures formed from spherical templates. In cyclic voltammetry, significant contributions from electrolysis of material both within the voids and from semi-infinite linear diffusion to the electrode surface is predicted to be observed. Experiments with two highly porous electrodes: graphite electrode (compact carbon fibre structure) and vitreous carbon foam electrode (reticular structure) were used to verify the theoretical model. The theoretical model successfully modelled both the interior and exterior contribution of the current and gave a reasonable value of the pore size for graphite felt electrode (9×10^{-5} m). The overall active area for both electrodes calculated using Randles Sevcik equation and the value from simulation are in very good agreements, showing that the programme is useful to predict the behaviour of porous electrodes using a hollow sphere model and that analytical theory can be used for sufficiently fast scan rate.

Reference

(1) Barnes, E. O.; Chen, X.; Li, P.; Compton, R. G. *J. Electroanal. Chem.* **2014**, *720-721*, 92.

(2) Szamocki, R.; Reculusa, S.; Ravaine, S.; Bartlett, P. N.; Kuhn, A.; Hempelmann, R. *Angew. Chem. Int. Ed.* **2006**, *45*, 1317.

(3) Szamocki, R.; Velichko, A.; Holzapfel, C.; Muecklich, F.; Ravaine, S.; Garrigue, P.; Sojic, N.; Hempelmann, R.; Kuhn, A. *Anal. Chem.* **2007**, *79*, 533.

(4) Lenz, J.; Trieu, V.; Hempelmann, R.; Kuhn, A. *Electroanalysis* **2011**, *23*, 1186.

(5) Chen, X.-J.; Xuan, J.; Jiang, L.-P.; Zhu, J.-J. *Sci. China, Ser. B: Chem.* **2009**, *52*, 1999.

(6) Chen, X.; Chen, Z.; Tian, R.; Yan, W.; Yao, C. *Anal. Chim. Acta* **2012**, *723*, 94.

(7) Chen, X.; Zhu, J.; Tian, R.; Yao, C. *Sens. Actuators, B* **2012**, *163*, 272.

(8) Zhang, Y.; Zeng, L.; Bo, X.; Wang, H.; Guo, L. *Anal Chim Acta* **2012**, *752*, 45.

(9) Wei, N.; Xin, X.; Du, J.; Li, J. *Biosens Bioelectron* **2011**, *26*, 3602.

(10) Chen, X.; Wang, Y.; Zhou, J.; Yan, W.; Li, X.; Zhu, J.-J. *Anal Chem* **2008**, *80*, 2133.

(11) Li, X.-H.; Dai, L.; Liu, Y.; Chen, X.-J.; Yan, W.; Jiang, L.-P.; Zhu, J.-J. *Adv. Funct. Mater.* **2009**, *19*, 3120.

(12) Chen, X.; Zhou, J.; Xuan, J.; Yan, W.; Jiang, L.-P.; Zhu, J.-J. *Analyst* **2010**, *135*, 2629.

(13) Whicher, J.; Biasucci, L.; Rifai, N. *Clin. Chem. Lab. Med.* **1999**, *37*, 495.

(14) Haidari, M.; Moghadam, M.; Chinicar, M.; Ahmadieh, A.; Doosti, M. *Clin. Biochem.* **2001**, *34*, 149.

(15) Gallego, N. C.; Klett, J. W. *Carbon* **2003**, *41*, 1461.

(16) Harikrishnan, G.; Patro, T. U.; Khakhar, D. V. *Carbon* **2007**, *45*, 531.

(17) Smith, R. E. G.; Davies, T. J.; Baynes, N. d. B.; Nichols, R. J. *Journal of Electroanalytical Chemistry* **2015**, *747*, 29.

(18) Weber, A. Z.; Mench, M. M.; Meyers, J. P.; Ross, P. N.; Gostick, J. T.; Liu, Q.-H. *J. Appl. Electrochem.* **2011**, *41*, 1165.

(19) Zhao, P.; Zhang, H.; Zhou, H.; Yi, B. *Electrochim. Acta* **2005**, *51*, 1091.

(20) Shah, A. A.; Watt-Smith, M. J.; Walsh, F. C. *Electrochim. Acta* **2008**, *53*, 8087.

(21) Wu, T.; Huang, K.; Liu, S.; Zhuang, S.; Fang, D.; Li, S.; Lu, D.; Su, A. *J. Solid State Electrochem.* **2012**, *16*, 579.

(22) Vohler, O.; Reiser, P. L.; Martina, R.; Overhoff, D. *Angew. Chem., Int. Ed. Engl.* **1970**, *9*, 414.

(23) Brookes, B. A.; Davies, T. J.; Fisher, A. C.; Evans, R. G.; Wilkins, S. J.; Yunus, K.; Wadhawan, J. D.; Compton, R. G. *J. Phys. Chem. B* **2003**, *107*, 1616.

(24) Davies, T. J.; Moore, R. R.; Banks, C. E.; Compton, R. G. *J. Electroanal. Chem.* **2004**, *574*, 123.

(25) Davies, T. J.; Banks, C. E.; Compton, R. G. *J. Solid State Electrochem.* **2005**, *9*, 797.

(26) Chevallier, F. G.; Davies, T. J.; Klymenko, O. V.; Jiang, L.; Jones, T. G. J.; Compton, R. G. *J. Electroanal. Chem.* **2005**, *577*, 211.

(27) Davies, T. J.; Brookes, B. A.; Fisher, A. C.; Yunus, K.; Wilkins, S. J.; Greene, P. R.; Wadhawan, J. D.; Compton, R. G. *J. Phys. Chem. B* **2003**, *107*, 6431.

(28) Davies, T. J.; Compton, R. G. *J. Electroanal. Chem.* **2005**, *585*, 63.

(29) Davies, T. J.; Ward-Jones, S.; Banks, C. E.; Del Campo, J.; Mas, R.; Munoz, F. X.; Compton, R. G. *J. Electroanal. Chem.* **2005**, *585*, 51.

(30) Butler, J. A. V. *Trans.Faraday Soc.* **1924**, *19*, 729.

(31) Laborda, E.; Henstridge, M. C.; Batchelor-McAuley, C.; Compton, R. G. *Chem. Soc. Rev.* **2013**, *42*, 4894.

(32) Shoup, D.; Szabo, A. *J. Electroanal. Chem. Interfacial Electrochem.* **1982**, *140*, 237.

(33) Paddon, C. A.; Silvester, D. S.; Bhatti, F. L.; Donohoe, T. J.; Compton, R. G. *Electroanalysis* **2007**, *19*, 11.

(34) Klymenko, O. V.; Evans, R. G.; Hardacre, C.; Svir, I. B.; Compton, R. G. *J. Electroanal. Chem.* **2004**, *571*, 211.

(35) Gavaghan, D. J. *J. Electroanal. Chem.* **1998**, *456*, 25.

(36) Gavaghan, D. J. *J. Electroanal. Chem.* **1998**, *456*, 13.

(37) Gavaghan, D. J. *J. Electroanal. Chem.* **1998**, *456*, 1.

(38) Crank, J.; Nicolson, E. *Proc. Camb. Phil. Soc.* **1947**, *43*, 50.

(39) Press, W. H.; Teukolsky, S. A.; Vetterling, W. T.; Flannery, B. P. *Numerical Recipes: The Art of Scientific Computing*; 3rd Edition ed.; Cambridge University Press, 2007.

(40) Belding, S. R.; Laborda, E.; Compton, R. G. *Phys Chem Chem Phys* **2012**, *14*, 14635.

(41) Bard, A. J.; Faulkner, L. R. *Electrochemical Methods: Fundamentals and Applications*; 2nd ed.; Wiley, 2000.

(42) Compton, R. G.; Banks, C. E. *Understanding Voltammetry*; 2nd ed.; Imperial College Press: London, 2011.

(43) Han, P.; Bartels, D. M. *J. Phys. Chem.* **1996**, *100*, 5597.

(44) Li, Q.; Batchelor-McAuley, C.; Lawrence, N. S.; Hartshorne, R. S.; Compton, R. G. *J. Electroanal. Chem.* **2013**, *688*, 328.

Chapter 8

Conclusions

The work presented in this thesis focuses on the potential of room temperature ionic liquids to improve the limitations of the present generation of amperometric gas sensors. These limitations include:

a) A short lifespan due to solvent evaporation in extreme environments;

b) The narrow application scope because of the solvent breakdown under extreme conditions, notably high temperatures;

c) The membrane used for gas selection and electrolyte leakage prevention slows down the movement of gas and increases the response time of the gas sensors;

d) Narrow electrochemical windows preclude the detection of certain gases which are oxidised/reduced outside of the voltage windows.

In order to overcome these problems arising from conventional electrolyte, RTILs were used instead in this thesis with their advantages discussed in Chapter 2. Microelectrodes were employed in this thesis as working electrodes to compensate some drawbacks of RTILs including high viscosity and low conductivity.

Chapter 4 examined the interaction between imidazolium cation based RTILs and carbon dioxide. A model of kinetics of CO_2 uptake/release was proposed which simulated well the whole process. Considerably high CO_2 uptake has been achieved, indicating the applicability of the RTIL to be employed not only as an electrolyte, but also as a CO_2 sequestration media.

Oxygen detection was performed in a phosphonium cation based RTIL, as described in Chapter 5. The solubility and diffusion coefficient of O_2 were determined by the experimental chronoamperometry. It was proposed that O_2 was reduced into superoxide which was further reduced to the product. A linear dependence between O_2 solubility and partial pressure was found. It was also discovered that with the introduction of CO_2, the superoxide anion was trapped which resulted in nearly doubled voltammetric signal. A linear relationship between the reductive current and the O_2/CO_2 partial pressure was discovered at high O_2 concentration, indicating the potential of this RTIL to be developed into both an O_2 and O_2/CO_2 dual sensor.

Chapter 6 carried out oxygen concentration measurements in a series of alkylammonium cation based RTILs to study the potential of these RTILs being employed in oxygen gas sensors and lithium-air battery. Similar O_2 reduction peaks were found in all RTIL samples, and generally the diffusivity of O_2 decreases as the viscosity increases.

Porous electrodes were also studied in this thesis, as reported in Chapter 7. A theory was developed which allows insight into the electrochemistry of porous electrode structures. Experiments with two types of porous electrodes were used to verify the theoretical model. The proposed transition between linear diffusion to ‘thin layer’ behaviour occurred from internal pores successfully simulated the current response for both electrodes at different scan rates, and a reasonable value of pore size was determined.

Overall, this thesis illustrates that RTILs have great potential to be used in amperometric gas sensors to compensate problems caused by conventional electrolytes.